ELECTRICALLY ACTUATED MICROPOST ARRAYS FOR DROPLET MANIPULATION

by

Jonas Elliott Gerson

A thesis submitted to the Department of Chemical Engineering

In conformity with the requirements for

the degree of Master of Applied Science

Queen's University

Kingston, Ontario, Canada

(March, 2013)

“The first principle is that you must not fool yourself - and you are the easiest person to fool.”

- Richard P. Feynman

“To invent, you need a good imagination and a pile of junk.”

- Thomas A. Edison

Abstract

Precise manipulation of heterogeneous droplets on an open droplet microfluidic platform could have numerous practical advantages in a broad range of applications, from proton exchange membrane (PEM) fuel cells and microreactors, to medical diagnostic platforms capable of assaying complex biological analytes. Toward the aim of developing electrically controllable micropost arrays for use in open droplet manipulation, custom-designed titanium dioxide (TiO_2)-loaded poly(dimethylsiloxane) (PDMS) micropost arrays were developed in this work and indirectly mechanically actuated by applying an electric field.

Initial experiments explored the bulk properties of TiO_2-loaded PDMS films, with scanning electron microscopy (SEM) confirming a uniform TiO_2 particle distribution in the PDMS, and tensile testing of bulk films showing an inverse relationship between TiO_2 % (w/w) and Young's Modulus with the Young's Moduli quantified as 4.22 ± 0.51 MPa for unloaded PDMS, 2.27 ± 0.18 MPa for 10 % (w/w) TiO_2, and 1.39 ± 0.20 MPa for 20 % (w/w) TiO_2. Following bulk material evaluation, soft lithography methods were developed to fabricate TiO_2-loaded PDMS micropost arrays. Mathematical predictions were applied to design microposts of varying shape, length, and gap spacing to yield super-hydrophobic surfaces actuatable by an electric field. Visual inspection and optical microscopy of the resulting arrays confirmed a non-collapsed micropost geometry. Overall, round microposts that were 100, 200, and 300 μm in length, 15 μm in diameter, and spaced 50 μm apart were produced largely free of defects, and used in contact angle measurements and micropost deflection experiments. Droplet contact angles measured on the arrays remained above 120° indicating the arrays successfully provided super-hydrophobic surfaces. Individual microposts deflected most notably above an electric field strength of 520 kV/m (12.5 kV nominal voltage).

The ability to mechanically deflect customized microposts using an electric field demonstrated by this work is promising for translating this technology to precise droplet manipulation applications. Indirect actuation of droplets could enable the manipulation of liquids with varying electrical properties, which is a limitation of current micropumping technologies. Once optimized, electrically actuated micropost arrays could significantly contribute to the micro-handling of heterogeneous, highly ionic, and/or deionized fluids.

Acknowledgements

To all those who have supported me throughout my research, I sincerely thank you. There would be no road to travel without bricklayers, no bricks without brick makers, and no clearing in the woods without those who came before.

To Dr. Kunal Karan, for believing in my ideas and taking a chance, and to Dr. Dominik Barz for entertaining them. To my dear friends in the Department, especially Dr. Jeffery A. Wood, whose thoughtful discussions helped refine my thoughts and techniques, as well as my ability to forget everything and lose myself in a great time. Thank you all.

Thank you to those students in the Department of Physics, and to all the users of the QFAB, for the late night companionship and troubleshooting. And to Dr. Robert Knobel for keeping that ship afloat and sailing smoothly, even on sometimes rough seas.

Those whose equipment, and skilled use thereof, aided my project, I thank you; Dr. Xiaohu Yan for his skilled SEM work, Dr. Aris Docoslis for the use of his laboratory and goniometer, and Adam Ozwald for his help with mechanical testing techniques. Thank you also to Evonik Industries who generously provided the titanium dioxide samples used in this work.

And to my dearest of friends, Ian Swyer, thank you for reminding me that this is only the beginning – and that I had better finish it one day so that I can get on to the rest!

Thank you to my wife, Allison Turner, without whom I would not be writing this today.

And of course thank you to my parents, for always encouraging my ideas and for whom daydreaming was never considered a bad habit, but rather, something to be encouraged.

Table of Contents

List of Figures

List of Tables

List of Major Abbreviations

μTAS	Micro total analysis system
2-D	Two-dimensional
3-D	Three-dimensional
AC	Alternating current
ALD	Atomic layer deposition
Ar+	Argon ions
ASME	American Society of Mechanical Engineers
ATDA	All terrain droplet actuation
CAD	Computer-aided design
CAH	Contact angle hysteresis
CB	Cassie-Baxter
CVD	Chemical vapor deposition
DC	Direct current
DEP	Dielectrophoresis
DI	Deionized
DLS	Dynamic light scattering
DMSO	Dimethyl sulfoxide
DRIE	Deep reactive ion etching
EBR	Edge bead remover
EDP	Ethylene diamine pyrochatechol
EHD	Electrohydrodynamic
EP	Electrophoresis
Fe_3O_4	Iron oxide
FIB	Focused ion beam
HF	Hydrofluoric acid
KCl	Potassium chloride
KOH	Potassium hydroxide
LED	Light-emitting diode
LIGA	Lithographie Galvanoformung Abformung
MEMS	Micro-electromechanical systems
MUV	Mid-ultraviolet
NiFe	Nickel-iron
PANI	Poly(aniline)
PC	Poly(carbonate)
PDMS	Poly(dimethylsiloxane)
PEM	Proton exchange membrane
PMMA	Poly(methylmethacrylate)
RICM	Reflection interference contrast microscopy
RIE	Reactive ion etching
RPM	Revolutions per minute
SC	Supercritical drying
SD	Standard deviation
SEM	Scanning electron microscopy
TiO_2	Titanium dioxide
TMAH	Tetramethyl ammonium hydroxide
UV	Ultraviolet

Chapter 1

Introduction

1.1 Project Motivation and Overview

Micro-total analysis systems (μTAS) are of great potential towards a number of relevant chemical engineering applications, including those extending to the design of chemical reactors and medical diagnostic devices. The design of these systems would significantly benefit from progress toward developing a μTAS capable of precisely manipulating droplets of heterogeneous fluids on open surfaces. In the case of proton exchange membrane (PEM) fuel cells, the removal of the byproduct water remains an ongoing challenge [1]. The ability to effectively and predictably remove largely deionized water droplets via a controllable microfluidic platform could prove valuable towards the implementation of PEM fuel cells in practical applications. Similarly, by allowing for more precise control of droplet motion at the microscale, more advanced medial diagnostic platforms are theoretically obtainable whose precise control of fluids could advance our abilities to run multiple assays, in series or parallel, on blood and/or other biological analytes [2].

Current approaches to controlled microfluidic droplet manipulation rely largely on direct electrical actuation of a liquid through applying an external electric field [3]. Electrical forces demonstrate favorable scaling with size, and microelectrode geometries are readily fabricated using well-established lithography techniques from the semiconductor industry allowing for high intensity electric-field strengths. Electric fields scale with electrode size, do not require current flow through the structure, and can be used with a wide variety of commonly available materials. The extensive use of these materials for a vast number of other electronic products allows for practical implementation, facilitating the production and practical use of platforms that incorporate electrodes.

However, the use of direct electrical actuation of droplets limits the use of electric-field related techniques to the manipulation of liquids that have some degree of mobile charge [3]. For liquids of insufficient electrical conductivity, the total ion concentration on which the applied voltage can act is too low and droplet actuation will not be achieved. For highly conductive liquids, direct application of electric fields will result in large potential drops and current flow, ultimately leading to sharp increases in fluid temperature [3]. This is particularly problematic when handling temperature-sensitive solvents or biological analytes whose components typically denature upon heating [3].

The alternative to direct actuation relies on the advantage of using mechanical surface wetting gradients to manipulate droplet surface position, which is an indirect actuation technique [4]. Open surface mechanical wetting gradients have been successfully established by using materials prepared with a micropost or microhair surface geometry, which in turn induces changes in the surface energy by altering the surface morphology [5]. However, these systems were largely static in overall approach, whereas the current study aimed to develop a dynamic micropost approach. Although there has been work on utilizing magnetic fields to actuate a surface (as opposed to electric fields), limited success has been achieved to date with this approach [6]. Additionally the need for a magnetic field requires current flow throughout the structure, raising problems for the use of polymeric materials, requiring advanced or specialized materials and techniques to fabricate the devices [7].

The ability to precisely control surface wettability, and therefore droplet position, on complex surfaces via electric field modulation could significantly advance fields linked to ‘open droplet’ microfluidic technologies, particularly in the design of μTAS-encompassing microreactors and medical diagnostic systems, amongst other applications. To date, little progress has been made towards developing a controlled, indirectly actuated micropost system using an electric field, toward the aim of precisely manipulating droplets by modulating wettability gradient.

The development of dielectric polymeric composite micropost arrays could permit the control of droplets of heterogeneous fluids, such as colloidal dispersions and other suspensions including biological analytes, in a broad range of open droplet microfluidic applications. Recent findings point to the ability of bulk PDMS loaded with poly(aniline) (PANI) or titanium dioxide-based materials (TiO_2) to mechanically actuate upon exposure to electric fields [8-10]. By translating these materials to a micropost system, it may be possible to effectively deflect the microposts through applying an external electric field. As a result, droplets placed on super-hydrophobic microposts could be dynamically manipulated via a surface morphology change. This change in surface morphology could allow for droplet manipulation. The surfaces could be designed or tailored according to a variety of design parameters, such as micropost shape, length (or height), spacing, and the surface energy and other material properties such as Young's modulus. This would allow for specific tuning of the surface to a desired end-use application, based on the matching of the analyte properties to the surface of the micropost array(s).

This thesis presents the development and characterization of custom-designed micropost arrays fabricated from TiO_2-loaded PDMS, intended for use in open droplet microfluidics to permit the manipulation of heterogeneous fluid droplets, without the need for direct electrostatic fluid actuation. Preliminary work focused on selecting, preparing, and characterizing bulk polymeric composite materials suitable for use in fabricating mechanically actuatable microposts. Following bulk material refinement and characterization, mathematical predictions were made to design microposts that would remain mechanically robust, deflect under electric fields, and provide a stable, super-hydrophobic surface. Using these predictions, photomasks were designed using computer-aided design (CAD) software, and manufactured by standard photomask fabrication techniques. Using conventional soft lithography techniques, protocols were developed and refined for the preparation of TiO_2-loaded PDMS-based micropost arrays. Finally, the resulting micropost arrays were characterized in terms of microarchitecture, contact angle, and actuation from micropost deflection resulting from an applied electric field.

1.2 Research Hypothesis and Specific Project Objectives

This research tested the hypothesis that custom-designed polymeric composite microposts loaded with dielectric particles and arranged in arrays, could yield stable, super-hydrophobic surfaces that could be actuated by an electric field.

The specific project objectives of this work were to:

i. Develop and characterize polymeric composite materials from which to make microposts:

- Select and fabricate bulk polymeric composite films that can be mechanically actuated by an electric field.
- Characterize the fabricated films via macroscopic evaluation and digital photography, scanning electron microscopy (SEM), Young's Modulus quantification, contact angle measurement, and bulk material deflection by an electric field.

ii. Design stable, super-hydrophobic polymeric composite micropost arrays that are mechanically robust and deflect (move) in the presence of an electric field:

- Utilize mathematical predictions to aid in parameter selection during the micropost design process, to predict the conditions that will yield stable, super-hydrophobic surfaces free of droplet collapse between microposts.

iii. Develop reproducible protocols for fabricating polymeric composite micropost arrays using soft lithography techniques:

- Develop micropost array photomask designs using CAD, and obtain customized photomasks manufactured by laser etching glass.
- Establish protocols by which to fabricate photoresist-based ‘master’ micropost array positive templates.
- Fabricate a polymer-based micropost array negative mold using the photoresist-based master templates.
- Develop and optimize protocols by which to prepare dielectric-loaded polymeric composite microposts using the negative molds.

iv. Characterize the micropost arrays and their ability to modulate droplet behavior:

- Qualitatively examine the micropost arrays and droplet behavior via digital photography.
- Evaluate the fabricated microposts under optical microscopy.
- Quantitatively characterize droplet contact angle as a function of micropost design and/or nominal voltage, using a goniometer and a direct current (DC) power supply.
- Test for micropost deflection and droplet movement in the presence of an electric field using video observation and subsequent image analysis techniques.

Chapter 2

Literature Review

2.1 Overview

To date, droplet manipulation approaches have focused largely on micropump technologies with devices that are fabricated using methods adopted from pre-existing areas of microtechnology. These include technologies such as integrated circuitry, metal oxide semiconductors (MOS), complementary metal oxide semiconductors (CMOS) and the microchip fabrication techniques utilized for micro-electromechanical systems (MEMS) [11]. MEMS compromise a broad field of study that seeks to miniaturize various electromechanical systems for implementation on a micrometer scale for improved efficiency and performance. This overall approach provides specific technological advantages such as improved response speeds and sensitivities of sensors, as well as allowing numbering-up (employing many MEMS devices in series and/or parallel) rather than scaling-up [12]. The extension of the MEMS approach into the realm of fluids handling resulted in the first devices to be called “micropumps” [13].

While these initial micropump systems were fabricated from silicon, glass, and other materials commonly applied in the semiconductor industry, the rapid expansion of interest surrounding micropumps and fluids handling has led to a shift toward less costly materials such as PDMS and other polymeric materials [14]. Through harnessing soft lithography techniques that employ a micro-stamping approach, micropumps have begun to successfully utilize polymers, as opposed to silicon or glass, as base materials [15, 16]. Devices for pumping of constrained fluids at the microscale are readily achieved using these polymeric materials; however, droplet manipulation micropumping technologies are still largely silicon-based due to the inability of current strategies to include kinetic structures with moving parts made from PDMS and/or other polymers [17].

The application of polymers in MEMS, micropump design, and open droplet microfluidic device fabrication is an exciting and highly promising direction toward achieving novel droplet manipulation devices. The relevant background theory, microfabrication techniques, and materials science linked to the development of polymeric MEMS/micropump devices, in addition to current approaches toward droplet manipulation, will therefore be the main focus of this literature review.

2.2 Surface Phenomena

To understand the mechanism of using an actuated micropost for droplet manipulation, the underlying physics of surface wetting and interfacial phenomena are required. Therefore, this section will explore current wetting models and methods by which to model super-hydrophobic surfaces.

2.2.1 Modes of Wetting

2.2.1.1 Young-Dupre Wetting Model

For an ideal surface, wetting is described via the Young-Dupre Equation (Equation 1):

$$\cos\theta = \frac{\gamma_S - \gamma_{SL}}{\gamma_L} \qquad \text{Equation 1}$$

where θ is the contact angle of a liquid droplet with a solid surface, γ_S is the surface tension of the solid (with vapour), γ_{SL} is the interfacial tension between the solid and the liquid, and γ_L is the surface tension of the liquid (with vapour). The Young-Dupre equation gives the relationship between equilibrium contact angle and the interfacial properties of the surface and liquid when the surface is inert, physically flat, and homogeneous and when gravitational forces can be neglected [18]. This relationship is commonly used for characterizing surface interfacial properties by measuring contact angles of known surface tension liquids. However, it cannot describe chemically heterogeneous surfaces and therefore more sophisticated approaches are required.

2.2.1.2 Wenzel Model

As a result of the need for less restrictive assumptions and a more general wetting relationship, studies modeling non-ideal wetting of liquids on rough and/or heterogeneous surfaces have been performed, most notably in work with rough surfaces by Wenzel (1936) [19] and in wetting studies by Cassie and Baxter (1944) [20]. The 'Wenzel' state, generally considered in the case of a 'rough' surface, can be defined in terms of contact angle as shown by the Wenzel Equation (Equation 2):

$$\cos\theta_w = r_w \cos\theta \qquad \text{Equation 2}$$

where θ_w is the apparent contact angle observed on the rough surface and corresponds to the equilibrium state of minimum free energy, r_w is the roughness factor that represents the ratio of true solid surface area as compared to the apparent solid surface area, and θ is the contact angle as predicted by the Young-Dupre Equation for an ideal surface. Overall, the Wenzel Equation shows that rough surfaces can demonstrate large deviations from the contact angle of an ideal flat and homogeneous surfaces.

2.2.1.3 Cassie-Baxter Model

Super-hydrophobic surfaces have been a topic of much study due to their widely ranging practical implications [21-24]. Overall, materials are considered to be super-hydrophobic if they possess a contact angle greater than ~120º, with values as high as 160º and 175º reported [21, 22]. This is in contrast to homogeneous hydrophobic materials, which tend to approach contact angles between 100º and 120º [22]. Super-hydrophobic surfaces are achieved most notably as the result of rough surfaces or composite interfaces but can be achieved through chemical treatment of surfaces [21]. Frequently to achieve super-hydrophobicity, solid geometries are tailored so as to have air pockets at the second material interface. This is relevant given the desire to design and fabricate super-hydrophobic surfaces in this work, through making electrically actuated microposts that could induce droplet movement on these surfaces.

When the contact angle of a liquid on a composite interface composed of solid regions and air reaches a critical point, denoted as θ_c, the droplet will enter what is called the 'Cassie-Baxter' state or super-hydrophobic regime [20]. The Cassie-Baxter regime is described as a heterogeneous state in which air becomes trapped between the droplet (liquid) and the substrate (solid). This is readily achieved by employing a surface geometry that incorporates small pillars (or small posts). Figure 2.1 exemplifies droplets on micro-pillared surfaces in both Wenzel and Cassie-Baxter states.

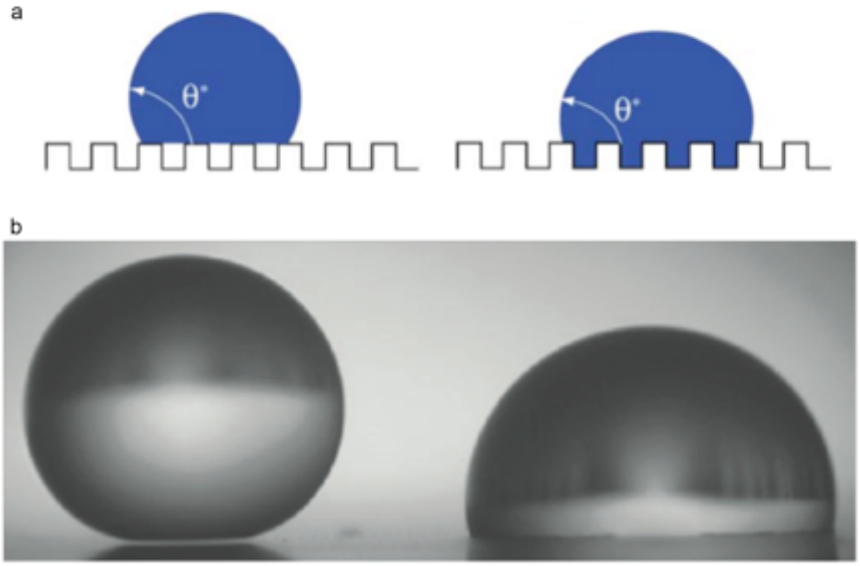

Figure 2.1: Wenzel and Cassie-Baxter droplet states on a micro-pillared surface [25].
Reproduced from Callies *et al.* (2005).
(a) Schematic diagram of the Cassie-Baxter state (left) and Wenzel state (right), and
(b) Photographed droplets demonstrating Cassie-Baxter (left) and Wenzel (right) states.

In a general sense, the Cassie-Baxter state is defined using Equation 3:

$$\cos\theta_E = r_\phi \phi_s \cos\theta_1 + (1-\phi_s)\cos\theta_2 \qquad \text{Equation 3}$$

where $\cos\theta_E$ is the observed equilibrium contact angle, r_ϕ is the roughness factor of the surface being wetted, ϕ_s is the area fraction wetted by the droplet, θ_1 represents the equilibrium contact angle of material 1, and θ_2 the equilibrium contact angle of material 2. For a composite surface composed of solid material 1 and air (material 2), this simplifies the equation as the contact angle of air is 180° [20].

2.2.1.4 Wenzel to Cassie-Baxter Transition

Since the contact angle between air and water is 180°, the entrapment of air beneath the droplet due to microposts greatly increases the observed contact angle, shifting the droplet from a Wenzel regime to a Cassie-Baxter regime through obtaining values of $\theta > \theta_c$. The observed shift between Wenzel and Cassie-Baxter states as a function of contact angle is shown as the inflection point in Figure 2.2, where the dotted line represents a metastable state in which the Cassie-Baxter regime is met [22].

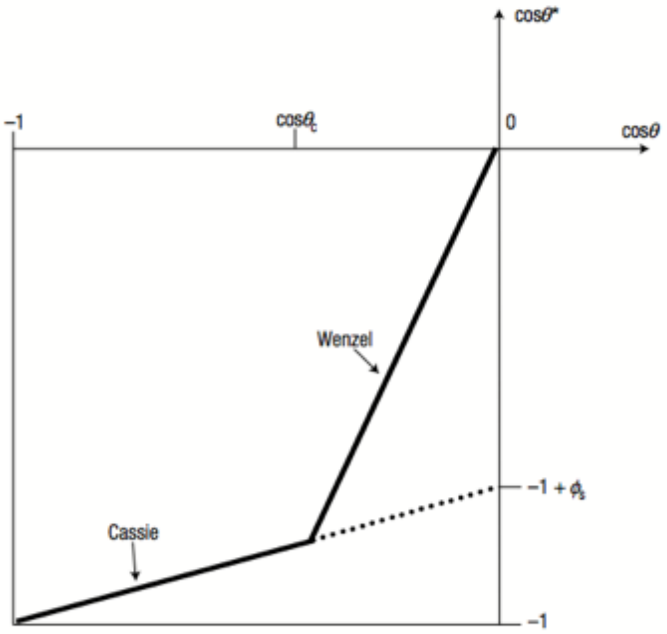

Figure 2.2: The Wenzel and Cassie-Baxter states as a function of contact angle [22].

2.2.2 Contact Angle Hysteresis

For an ideal surface, free of surface defects, the measured contact angle should remain constant, regardless of minor changes in droplet volume. More specifically, the contact angle measured for a certain droplet, as compared to the contact angle measured for a slightly lesser volume of liquid (the receding contact angle) and the contact angle measured for a droplet of slightly greater volume (the advancing contact angle) should all have the same values assuming that the droplet is small enough to neglect gravitational forces. In other words, no difference between the receding and the advancing contact angles will be observed for an ideal surface. In reality, the difference between the receding and the advancing contact angles is not zero and is referred to as the contact angle hysteresis (CAH), as defined by Equation 4:

$$\Delta\theta = \theta_a - \theta_r \qquad \text{Equation 4}$$

where $\Delta\theta$ is the CAH, θ_a is the advancing contact angle, and θ_r is the receding contact angle. Similarly, instead of advancing and receding contact angles, the lefthand (θ_L) and righthand (θ_R) side contact angles may be reported for each droplet analyzed and used to calculate the CAH as was performed in the current work (Equation 5):

$$\Delta\theta = \theta_R - \theta_L \qquad \text{Equation 5}$$

As almost no surface is free of defects, the predicted wettability of a surface is not free of error. The mathematical equations developed toward modeling the contact angle of super-hydrophobic surfaces, as listed in the previous sections, do not completely describe the contact angles of non-ideal systems.

Generally, there is a difference between the advancing and receding (or left and right side) contact angles measured for a droplet deposited on a non-ideal surface. This is due to the 'pinning' of the droplet to small defects on the surface thereby impeding its flow. These defects may be thought of as 'sticky' regions, and the CAH may be thought of as a measure of a liquid's stickiness to a surface or substrate [26]. The ability to control CAH through surface geometry could have large implications for the successful implementation and development of custom-designed super-hydrophobic surfaces.

2.2.3 Super-Hydrophobic Surfaces in Nature

Super-hydrophobic surfaces are found in nature and commonly employ a micro-pillared surface geometry, so as to transition to the Cassie-Baxter state (Figure 2.3). For instance, the petals of a lotus leaf exploit super-hydrophobicity to clear the petals of fluid and/or debris [27]. Interestingly, similar micro-pillar structures, varying by only microns in terms of spacing, can yield very different results from a wetting perspective [28]. These minor differences can account for what is known as the 'Impregnated-Cassie' regime, or rose-petal wetting. Rose-petal wetting occurs when droplets on super-hydrophobic surfaces also adhere to the surfaces, leading to high CAH [29].

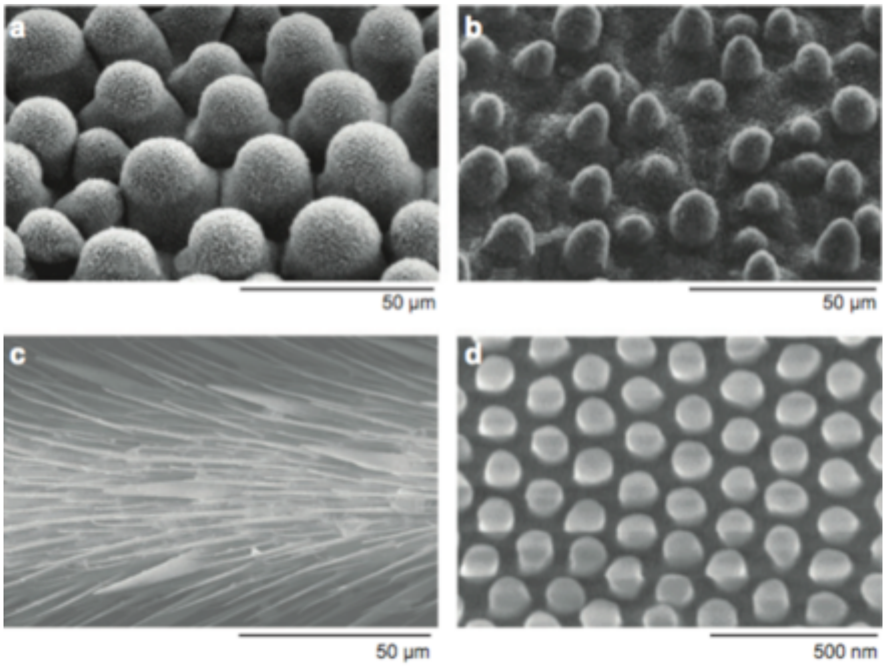

Figure 2.3: Naturally-occurring examples of super-hydrophobic surfaces [26].
Reproduced from Quere *et al.* (2008).
(a) Surface of an elephant's ear plant (*Colocasia esculenta*), (b) Lotus leaf,
(c) Water strider leg, and (d) Mosquito (*Culex pipiens*) eye surface.

2.2.4 Modeling and Design of Synthetic Super-Hydrophobic Surfaces

To drive or manipulate droplets, several key parameters must be readily predictable with great accuracy. More specifically, this includes, but is not limited to, wetting state transition, contact angle hysteresis, and droplet flow through microposts (and the associated wettability gradient).

2.2.4.1 Predicting Wetting State Transition

The study of wetting state transition from the Cassie-Baxter state to the Wenzel state has been explored extensively [30-34]. Many different methods of 'collapse' leading to this transition have been proposed, including transition linked to Laplace pressure (the pressure within a droplet from the surface tension of the droplet with the vapour phase) and transition due to droplet impact [30, 35, 36]. Recently, several thermodynamic models have been introduced to better define this transition phenomenon, but are to date, incomplete for fully predictive purposes [37, 38].

Importantly, evidence from work by Peters *et al.* (2009) points to the fact that this transition may be roughly correlated to the Capillary number, which describes the ratio of viscous forces to surface tension forces across a two-phase interface [39]. For low Capillary numbers ($Ca \ll 1$) flow is dominated by surface tension. In this study by Peters *et al.* (2009), the transition from the Cassie-Baxter state to the Wenzel state was investigated using high-speed photography amongst an array of square microposts. It was found that there was a critical gap size between the microposts that prevented the wetting state transition from occurring [39]. Critical micropost gap size scaled with pillar height indicated that based on micropost configuration and/or spacing, there may be a corresponding optimal micropost height. However, these results relied on only a very small subset of experiments, and thus only represent an empirical estimation.

Alternatively, Bico, *et al.* (2002) proposed the following criteria (Equation 6) needed for the wetting transition to occur:

$$\cos\theta_c = -\frac{1-\phi_s}{r-\phi_s} \qquad \text{Equation 6}$$

where ϕ_s is the areal fraction of the posts compared to the substrate [40]. However, it should be noted that meta-stable states can also exist outside of the predictive values from Equation 6 [22].

To bridge this gap, Moulinet and Bartolo (2006) utilized reflection interference contrast microscopy (RICM) to obtain a topographic image of a droplet in the Cassie-Baxter state [30]. This allowed for the creation of a robust model that was able to predict droplet behavior well beyond the range of the given set of experiments. The rate of droplet evaporation, and therefore droplet diameter, was shown to be strongly tied to droplet ‘impalement’ (as described in Figure 2.4). Simply stated, droplet size affects the wetting state immensely. This will depend on not only the surface the droplet is on, but the smaller the droplet the larger the Laplace pressure, the higher the rate of evaporation, and thus the decreasing droplet diameter will push the droplet to ‘fall’ between the posts. This shows the critical nature of the environment on digital microfluidic systems of this nature.

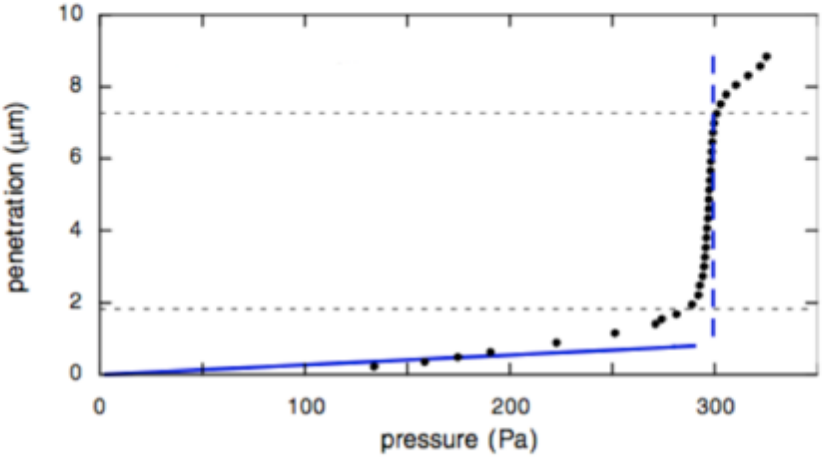

Figure 2.4: Cassie-Baxter to Wenzel state transition model results [30].
Reproduced from Bartolo *et al.* (2006).
The dots represent experimental data, while the curve represents data predicted from the model.
The dotted line indicates the predicted wetting state transition.

This appears to provide a satisfactory model for the prediction of the transition from the Cassie-Baxter state to the Wenzel state, based upon available design parameters.

2.2.4.2 Predicting Contact Angle Hysteresis (CAH)

Since CAH has such a great impact on observed wetting behavior, significant efforts have also been made toward mathematically predicting CAH. However, the results remain elusive, and only recently has a model arisen that can effectively predict contact angles with satisfactory precision [41, 42]. Correspondingly, this model was also able to accurately predict roll-off angles, which refer to the contact angles at which droplets will release from a given surface.

This CAH prediction method involved the use of unique differential parameters in the calculation of the advancing and receding contact angles [42]. The ‘differential area fraction’, represented as ϕ_d, was taken into account and used in modified forms of the Cassie-Baxter equation, as shown by Equation 7 and Equation 8.

$$\cos\theta_{adv} = r_{\phi}\phi_{d,adv}\cos\theta_1 + (1-\phi_{d,adv})\cos\theta_2 \qquad \text{Equation 7}$$

$$\cos\theta_{rec} = r_{\phi}\phi_{d,rec}\cos\theta_1 + (1-\phi_{d,rec})\cos\theta_2 \qquad \text{Equation 8}$$

The differential area fraction (defined as the differential area the droplet sweeps out as it both advances and recedes) is contrasted to the ‘global area fraction’, ϕ_s, which is defined as the ratio of the projected surface area to the whole surface area. Integrating this over the material surface, some limiting cases become apparent based on surface geometry. As the area fraction and roughness factor are directly related to the micropost geometry, both can be easily calculated, allowing for modeling of CAH and subsequently device design.

2.2.5 Wettability Gradients for Droplet Manipulation

Daniel and Chaudhury (2002) explored the motion of droplets due to a wetting gradient [4]. This is particularly applicable in the case of wettability-induced droplet motion. While the work of Daniel and Chaudhury (2002) is not the first study involving wettability-induced droplet movement [43], it does represent a practical approach towards achieving it.

It was found that the force of the droplet was impeded greatly by moving against the wettability gradient. It was also found that while CAH did impede droplet flow to an extent, it did not do so significantly in this case. However, for the case being studied here, the prediction of CAH was of importance for designing a robust surface. The droplets examined in this case were

1-2 µL in volume. Results showed that a droplet would move at speeds ranging from 1-2 mm/s, but with the addition of a square acoustic wave (40 µm amplitude, 100 Hz), droplet velocity was greatly increased to range from 5 to 10 mm/s. There was a clear positive correlation between droplet radius and achievable droplet velocity, due to both the wetting gradient and vibration. In particular, even with a CAH of 9º, a maximum velocity of 5 mm/s was observed.

With the verification of wetting-gradient induced velocity, as well as the ability to model this velocity, Daniel and Chaudhury (2002) provided an excellent framework for the examination of how induced wetting gradients affect droplet motion (Figure 2.5).

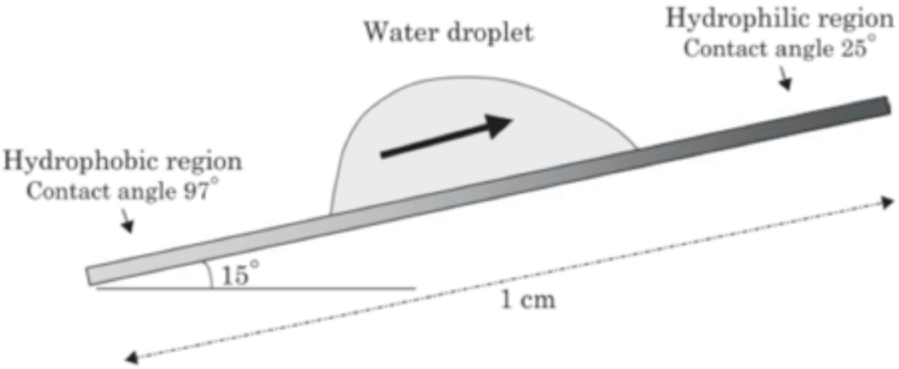

Figure 2.5: Droplet moving against height gradient, due to wettability gradient [43].
Reproduced from Berthier *et al.* (2008).

Based on this observed ability for wettability gradients to drive droplets, other efforts have been made to modulate droplet movement by electro-wetting techniques on smooth surfaces [44]. However, little progress to date has been made to actively change the wettability of a surface based on geometrical alterations of the substrate.

As previously noted, certain natural systems deploy microhair-like structures to increase wetting contrast. Although some efforts have been made to replicate these structures in polymeric substrates, these studies were performed only as static systems [45]. For the purposes of this work, what is instead proposed is the development of dynamic polymeric microposts, that could be deflected or collapsed using electrical forces so as to induce a wetting state transition or a tightly controlled wettability gradient.

The use of polymeric materials in micropost fabrication is numerous [16], and their mechanical stability has been subject to extensive review [46]. Work by Roca-Cusachs *et al.* (2005) examined PDMS micropillars (or microposts), to investigate how length-to-width ratios affect micropost stability [47]. While the microposts were anisotropic due to their method of fabrication, the model used to predict post ground-collapse was done so for an isotropic feature. This was a benefit, as making anisotropic features is relatively difficult as compared to fabricating isotropic features [12]. It should be noted that the model employed in the study of Roca-Cusachs *et al.* (2005) accounted for microposts adhering to one another, rendering this model even more robust for practical application. By exploiting this model to design microposts near their point of collapse, a small perturbation could be utilized to achieve reversible micropost collapse. This, in essence, would seek to mimic the robust, natural surfaces presented by Hsu and Sigmund (2010) and Bernardino *et al.* (2010) [45, 48], which provide simple but highly robust hydrophobic materials.

Microposts displaying multi-scale geometric features would be desirable to use larger features to subsequently decrease manufacturing complexity. This can be accomplished by the varying the geometric shape of the micropost perimeter to enhance hydrophobic character. As the top of the posts wet when the microposts are upright, then by creating a tortuous micropost wall to the droplet, surface hydrophobicity could potentially be greatly increased. Presumably, when the posts are actuated, the droplet would then advance (move forward) due to the wetting gradient created. This concept is central to the work of this thesis.

2.3 Relevant Electrical Forces

While extensive reviews surrounding electric forces are available in the literature, this section aims to provide a brief overview of the basic underlying electrical concepts as they relate to this project. More specifically, as TiO_2 nanoparticles were suspended in PDMS, the following equations defining dielectrophoretic forces acting on particles and dielectrophoresis provide relevant background theory.

2.3.1 Forces on Particles

For submicron particles and/or nanoparticles, although thermal effects due to Brownian motion can be important, the effects of gravity can be largely ignored, with the effects of viscous and applied electrical forces dominating instead [49]. These effects are most noticeable and relevant during the curing and distribution of particles within uncured PDMS during the cross-linking process.

The electrical forces acting directly on submicron particles are largely electrophoresis (EP) and dielectrophoresis (DEP), and are governed by Equation 9;

$$\boldsymbol{F_{DEP}} = (\boldsymbol{p} \cdot \boldsymbol{\nabla})\boldsymbol{E} \qquad \text{Equation 9}$$

where $\boldsymbol{p} \cdot \boldsymbol{\nabla}$ necessitates a field gradient in order to produce a dielectrophoretic effect, $\boldsymbol{p}$ being the charge of the dipole. This is analogous to the Coloumb force for charged particles, represented as Equation 10;

$$\boldsymbol{F_{EP}} = \boldsymbol{QE} \qquad \text{Equation 10}$$

where Q is the total particle charge [49].

Electrophoresis refers to motion of a charged particle due to the action of an applied electric field (DC), while dielectrophoresis refers to the motion of a particle due to action of an applied electric field (AC or DC) on the particle dipole that field induces. While EP relates to particle behavior in the presence of a uniform or non-uniform electric field, DEP requires a non-uniform electric field, and the magnitude of the dielectrophoretic force depends largely on the system dimensions, particle size, voltage, and conductivity [50].

2.3.2 Dielectrophoresis

Dielectrophoresis is concerned with the behavior of particles subjected to non-uniform electric fields. While the particles do polarize, an imbalance in electric field strength occurs during particle polarization and the field strength on one side of a particle as compared to the other side will be higher or lower, but not equal. Overall, this leads to an imbalance in the forces acting on the particle resulting in particle movement.

In cases where the polarizability of a particle is higher than the surrounding medium, the dipole points in the direction of the field and the particle experiences "positive DEP," moving toward the strong electric field regions. The opposite situation leads to "negative DEP," with the particle moving away from the strong electric field regions. Overall, the intrinsic electrical properties of a particle will direct the outcome of particle behavior in a non-uniform field [49]. Generally, for a non-uniform field (spatially or temporally) as shown in Equation 11,

$$\langle \boldsymbol{F_{DEP}} \rangle = \boldsymbol{\pi \varepsilon_m a^3} \mathrm{Re}\left[\frac{\varepsilon_p^* - \varepsilon_m^*}{\varepsilon_p^* + 2\varepsilon_m^*}\right] \boldsymbol{\nabla} |\boldsymbol{E}|^2 \qquad \text{Equation 11}$$

where ε_m is the dielectric pemittivity of the material, particle volume is represented by a^3, and the bracketed portion represents the real components of the complex permittivities of the particles and the medium (ε^* is the complex permittivity (subscripts p and m represent particle and medium)). This is known as the Clausius-Mossotti factor, which describes the motion of the particles and frequency dependence. E is the electric field.

Given the droplet movement on the surface, electrowetting may play a role in droplet movement. In this case, the Maxwell force, alternatively known as the Korteweg-Helmholtz force density is described by Equation 12 [51] on the following page;

$$\mathrm{F} = \boldsymbol{\rho_f E} - \frac{\boldsymbol{\epsilon_0}}{\mathbf{2}}\boldsymbol{\nabla}\left[\boldsymbol{\epsilon} - \boldsymbol{\rho}\left(\frac{\boldsymbol{\partial\epsilon}}{\boldsymbol{\partial\rho}}\right)_{\boldsymbol{T}}\right]\boldsymbol{E}\cdot\boldsymbol{E} \qquad \text{Equation 12}$$

where $\boldsymbol{\epsilon}$ is the dielectric permittivity of the liquid, ρ is the density, T is the temperature, and the electric potential, $\boldsymbol{\phi}$, is encapsulated by the relation $\boldsymbol{E} = -\boldsymbol{\nabla\phi}$.

While both of these forces are reviewed here, determination of their respective dominance for this project is left to be determined for future studies.

2.4 Current Microfabrication Techniques

Toward the aim of developing a MEMS device in this work that could ultimately permit the precise manipulation of fluids or droplets with a wide range of properties, a thorough understanding of the current methods by which MEMS devices are manufactured is required. An overview of the standard microfabrication techniques applied in this field is included herein. Different lithographic techniques, etching, and types of micromachining are discussed to provide a background surrounding commonly employed microfabrication techniques.

2.4.1 Lithography

Lithography refers to the use of light to transfer a pattern onto a substrate, where the substrate is silicon, glass, gallium arsenide, or another material [12]. Since its invention in 1959, lithography has been extensively used as the workhorse for microelectronics, as a result of the rapid growth of the microelectronics sector [16]. Overall, during lithography, light is transmitted through a photomask onto photoresist, and the desired geometric pattern is thereby transferred onto the underlying substrate.

A thin film of polymeric material may be coated onto the substrate, and/or a photoresist applied. Depending on the photoresist used, the resist will either be washed away after exposure to light (as is the case with a ‘positive’ resist), or will remain intact in those areas exposed to light (a ‘negative’ resist). Thin photoresist layers are applied to the substrate through spin-coating and soft-baking at 60-100ºC for 5-30 minutes to evaporate any solvents in the photoresist and improve adhesion of the photoresist.

After selective exposure to light achieved through employing a photomask, the photoresist is hard-baked at 120-180ºC for 20-30 minutes to cure the microfeatures. This enables the substrate and/or thin polymeric film to be selectively etched, with those sections still covered in photoresist remaining un-etched to yield the formation of desired patterns or features.

Subsequently, the remaining photoresist can be removed and the process repeated, perhaps with additional thin-film layers, electroplating, chemical vapor deposition (CVD), atomic layer deposition (ALD), or the application of sputtered materials. Figure 2.6 provides a schematic overview of the major steps used during lithography.

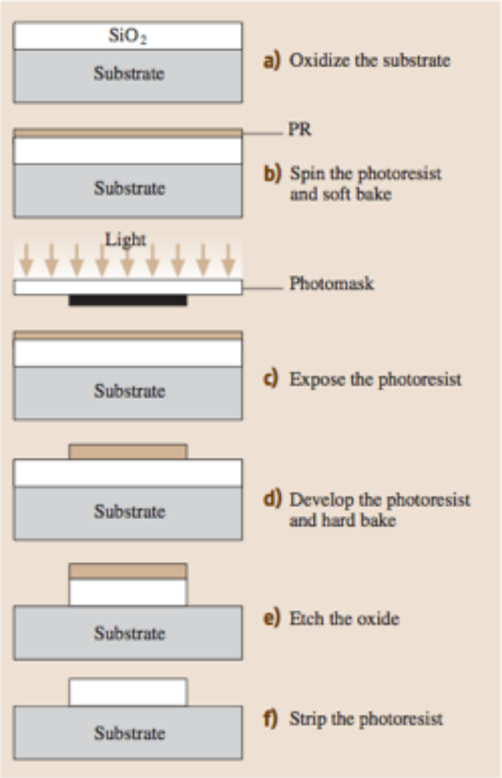

Figure 2.6: A schematic overview of the photolithography process [12].
Reproduced from Bhushan *et al.* (2004).

2.4.1.1 Photomasks and Light Sources

Physically, photomasks refer to a piece of fused silica with a thin layer of chromium approximately 100 nm in thickness [12]. Interestingly, for lithography applications with relatively large feature sizes (>100 μm), simple overhead transparency sheets with laser-printed patterns have served as functional masks [52].

The desired geometric pattern can be transferred to the substrate and/or photoresist by either optical- or electron-beam generators. Generally, wavelengths in the ultraviolet (UV) range (365 nm (UVA), 248 nm (MUV), or 193 nm (UVC)) are used. These wavelengths are produced using high-pressure mercury lamps for features above 0.25 μm in size. However, for features between 0.25 μm and 0.13 μm, deep UV sources must be used. For those features below 0.13 μm in size, extreme-UV (EUV) is the preferred source, although X-rays and electron beams are also available [12]. However, for the use of X-rays and electron beams, different materials are required for device fabrication [12].

2.4.1.2 Etchants

To permit effective etching of the photoresist or substrate upon exposure to light (or some other source), it is desirable that etchants be both selective and directional. Selectivity refers to the etchant's ability to discern between the etching of the substrate and the masking photoresist layer, whereas directionality refers to how the etchant behaves under the masking layers.

For an isotropic etchant, the material is attacked in all directions at the same rate producing a circular etching pattern. In contrast, for anisotropic etchants, certain directions are favored for etching, allowing for the creation of vertical sidewalls and/or non-circular etching profiles [12]. Figure 2.7 illustrates examples of isotropic and anisotropic etching profiles.

Figure 2.7: Representative etching profiles [12].
Reproduced from Bhushan *et al.* (2004).
Isotropic etching (left) and anisotropic etching (right).

During the fabrication of MEMS devices, isotropic and anisotropic etching of glass (non-crystalline) and silicon (crystalline) are both important [12]. Isotropic wet etching is commonly achieved using diluted or buffered hydrofluoric acid (HF). Anisotropic wet etching has proven valuable toward the micromachining of silicon. The main anisotropic etchants used are potassium hydroxide (KOH), ethylene diamine pyrochatechol (EDP), and tetramethyl ammonium hydroxide (TMAH). The corresponding anisotropic wet etching rates are approximately 1 μm/minute at 85-110ºC (as compared to 0.1 μm/minute for isotropic wet etching), but vary with concentration, temperature, and crystal plain [12].

Dry etchants are also applicable in MEMS fabrication, and offer some specific advantages to their wet etchant counterparts, including the ability to create high-aspect ratio structures (or structures of high anisotropy). Three main dry etching techniques include high-pressure plasma etching, reactive ion etching (RIE), and ion milling. Each of these techniques uses a different mechanism to achieve directionality.

In high-pressure plasma etching, the use of reactive species is used to etch the substrate. The reactive species are generated at the surface and assist in the removal of material. This is similar to RIE, in which the reactive ions only interact with a surface species that becomes activated as a result of the collision of incident ions from the plasma.

Ion milling uses inert argon ions ($Ar+$) to remove material at the surface via the perpendicular delivery of ions to the surface, thereby ejecting the material. Pressures are typically 10^{-4} to 10^{-3} torr (thus requiring larger vacuum pumps), and etch rates are on the order of 4 nm/minute, which is considered relatively slow.

Directionality in these techniques is controlled due to the higher number of ions hitting incident to the surface, and therefore favoring the vertical direction. This is not to say that the ions do not interact with the wall, but rather, in order to increase the anisotropy, passivation (the formation of a non-reactive film surface) of the sidewalls is utilized. Deep reactive ion etching (DRIE) is one such example, and is able to achieve high-aspect ratios (30:1 in silicon is possible). The typical etching rate using this approach is on the order of 2 to 3 μm/minute. However, as compared to wet etching, dry etching demonstrates significantly reduced material selectivity; with etch rates of 1:1 for masking and substrate materials. These limitations make dry etching techniques suitable for use with thin layers, but not for etching thicker films [12].

2.4.1.3 Lithographie Galvanoformung Abformung (LIGA)

Lithographie Galvanoformung Abformung (LIGA) relies on the combination of X-ray lithography and electroplating to yield high-aspect ratio micromachined structures. Due to the use of X-rays, thick photoresist layers can be penetrated without scattering. As a result, highly accurate reproduction of photomask microfeatures is possible for high-aspect ratio microstructures. More specifically, microfeatures with 0.2 μm lateral width and aspect ratios exceeding 100:1 have been successfully achieved using LIGA methods [53]. LIGA photoresists are commonly made from poly(methylmethacrylate) (PMMA), while photomasks are typically fabricated from silicon-nitride with a gold absorber for X-rays. Once the resist is developed, the construct can be electroplated with a variety of materials such as nickel (Ni), copper (Cu), gold (Au), or nickel-iron (NiFe).

UV-LIGA (also dubbed ‘poor man’s LIGA’) has been developed using standard UV lithographic techniques, as previously described. Specifically, this UV-LIGA approach uses SU-8 photoresist, which is also commonly used in many other lithography techniques, with aspect ratios of up to 20:1 being achieved. However, removing the SU-8 after electroplating remains a challenge. Also, based on the intensities of the X-rays needed for this approach, the use of a synchotron must be used. This is disadvantageous due to the high costs and limited availability of such synchotron sources.

2.4.2 Soft Lithography

Soft lithography refers to the use of patterned elastomers as stamps, molds, or masks [16]. In doing so, soft lithography provides high-quality patterns with features ranging from 30 nm to 500 μm or greater in size. The advantages of this technology lie with its relatively inexpensive performance, without the need for costly and/or complex manufacturing facilities.

The first step in soft lithography is the creation of a “master template.” This can be achieved using previously discussed techniques to generate a mold from silicon or glass. The primary polymer used within soft lithography is PDMS. This is due to the favorable material properties of PDMS, which include low chemical reactivity, ease of release from molds, high surface conformity to molds (on the order of tens of nanometers), self-sealing ability, and low interfacial free energy [16]. Further, PDMS can be used to fabricate structures directly, be used to pattern surfaces through micro-contact printing (μCP), be treated with plasma and other chemistries for surface functionalization, or be used to pattern non-planar surfaces [16, 54, 55].

Overall, soft lithography is extensive and its intricacies and full capabilities are best described in the literature by Whitesides *et al.* (1998) [16, 56]. Additionally, more recent progress in soft lithography is extensively reviewed in work by Rogers and Nuzzo (2005) [56]. Of particular interest is the ability for soft lithography to provide a way to fabricate low-cost microstructures. Due to its versatility, being able to make micropumps utilizing soft lithography would be highly desirable. However, current micropump designs do not lend themselves well to this technique, largely due to the inability to create moving parts within PDMS, as previously mentioned. In the following sections, current micropumping methods will be discussed.

2.5 Microfluidic Handling Technologies

Digital microfluidics is a relatively new area of study. It is separately defined from microflows, ‘droplet’ microfluidics, and even open microfluidics, despite the fact that there is much overlap between these differently scaled areas of study (Figure 2.8) [43].

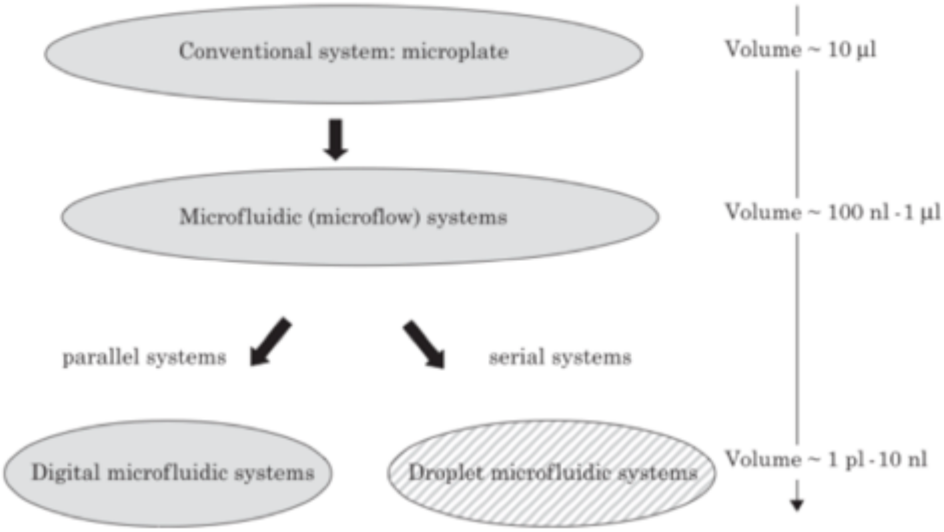

Figure 2.8: Scales of various microfluidic technologies [43].

In taking these definitions, digital microfluidics is the one of most relevance to this thesis (Figure 2.9). Specifically, each droplet is treated as a separate entity on a planar surface, rather than being part of a two-phase flow system.

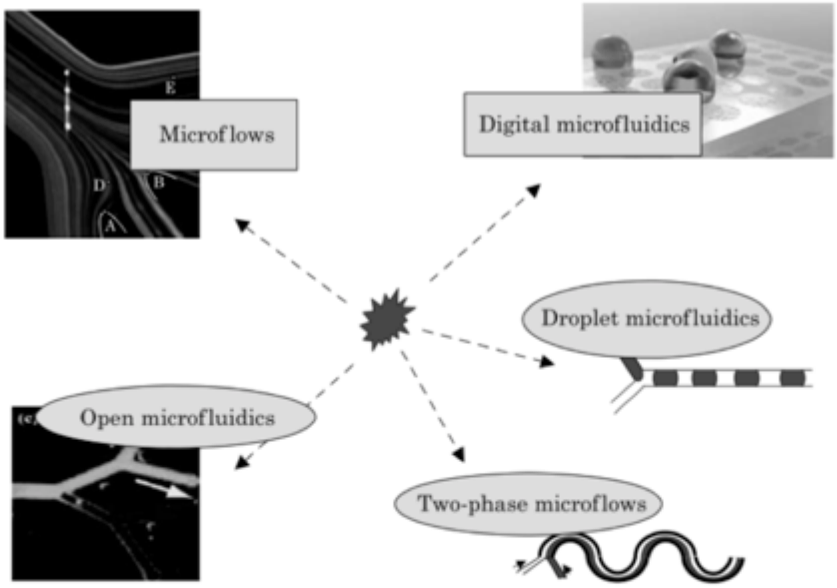

Figure 2.9: Different methods and definitions for microfluidic handling [43].
Reproduced from Berthier *et al.* (2008).

2.5.1 Current Micropumping Technologies

Micropumping technologies have experienced a flurry of activity in recent work [14]. The need to manipulate fluids on the micro-scale for μTAS and Lab-on-a-Chip technologies, amongst many other applications, is an encroaching reality. Many challenges need to be overcome to develop a successful micropump. These are situation-dependent, as the requirements and tradeoffs need to be weighed against one another [15]. For instance, a fuel-delivery micropump would differ in design requirements from one used for single-use drug delivery or medical diagnostics. The mechanisms of creating a driving force vary widely, as do the materials of construction, associated forward pressures generated, back-pressures tolerated, and flow rates achieved. Control and external size considerations must also be made [57, 58].

Additionally, a key criterion is whether the fluid is single phase or two phases. On the microscale, given the small diameters and different physical regime, as well as the utilization of multiple single droplets (for example, digital fluidics) there has been significant motivation to avoid traditional pumping methodologies. This was a primary motivation for this research and thus the following sections focus on alternative methods for fluid handling.

2.5.2 Electro-wetting

Electro-wetting requires a conductive fluid, which when charged moves to the counter-electrode. This is then reversed, having the fluid return to its original location, thus creating an oscillatory motion capable of doing work [57]. This concept is shown in greater detail within Figure 2.10.

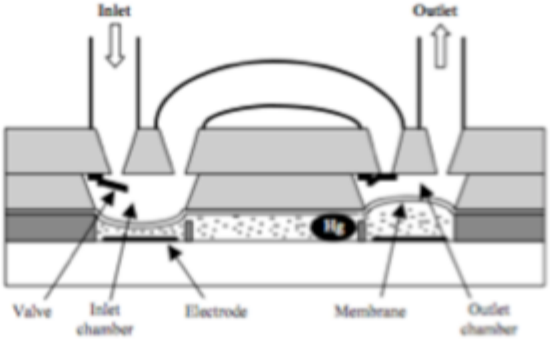

Figure 2.10: Example of a continuous electro-wetting micropump [57].
Reproduced from Yun *et al.* (2006).
The mercury is transferred between two electrodes, forming a bolus, which applies a force to the diaphragm. When the polarity is reversed, the bolus moves to the opposite electrode, which completes either the inflow or outflow step.

2.5.3 Alternative Fluid Handling Methods

Fluid handling aimed at the movement of single droplets have come about as an important paradigm for fluidic manipulation. More specifically, a method has been referred to as 'All Terrain Droplet Actuation' or ATDA for short [59]. ATDA has the ability to move away from traditional two-dimensional (2-D) planar surfaces, as seen in traditional droplet microfluidic platforms, and has shown the ability to move single droplets on inclined, declined, vertical, twisted, and upside-down surfaces (Figure 2.11). This ability was accomplished through the use of flexible copper-clad poly(imide) surfaces in which potentials were applied to matching pairs of electrodes.

Figure 2.11: Flexible copper-clad poly(imide) surface used for ATDA [59].
Reproduced from Abdelgawad *et al.* (2008).

Electro-wetting-on-dielectric is the accepted mechanism for the creation of fluid movement of the droplets [59]. This mechanism represents a new format for microfluidics. As the open manipulation of droplets has become more versatile and broadly applicable, the need to create other methods for manipulating droplets within this 'open droplet microfluidics configuration' now exists [59].

As this thesis is focused on developing such an alternative open droplet microfluidic platform for droplet manipulation, the following sections will further explore current alternative microfluidic handling approaches, including recently developed polymeric micropumps, artificial cilia, and polymeric composite microposts.

2.6 Polymeric Micropump Devices

There has been an effort to move away from using silicon- and glass-based substrates in micropumping technologies. This is attributed to the high costs of these materials as compared to employing polymeric materials. As an example, there has been a shift toward using PDMS for diaphragm materials in thermo-pneumatic micropump designs [60]. The material properties of PDMS also render it an attractive base material for microfluidic devices, as described in the following section.

2.6.1 Poly(dimethylsiloxane) Material Properties

The material properties of PDMS and other alternate materials such as PMMA have been widely studied, as touched on previously in this review. Toward the aim of this thesis to develop actuatable polymeric composite microposts, PDMS will be more extensively investigated herein. However, for a review of alternate materials, namely other polymeric materials and their properties found in microfluidic systems, please refer to work by Becker and Locascio (2002), and Soper *et al.* (2002) [60, 61].

Tables expressing the swelling parameters for PDMS within various solvents are also listed in the literature [62]. Some solvents that induce the least PDMS swelling include water, dimethylsulfoxide (DMSO), and ethylene glycol, while solvents that cause more significant swelling include pentanes and xylenes. Solvents which induce the greatest degrees of swelling may be useful in modifying PDMS surface chemistry and for extracting contaminants from bulk PDMS [62].

Often, the solubility parameter (or Hildebrand value) is used to compare solubilities and/or swelling. The Hildebrand value is measured in units of $\mathrm{cal}^{1/2}\mathrm{cm}^{-3/2}$, and is represented by Equation 13;

$$\delta = c^{1/2} = \left(-\frac{U}{V}\right)^{1/2} \qquad \text{Equation 13}$$

where c is the cohesive energy density (a ratio of the molar internal energy to the molar volume). This parameter is useful for determining the equilibrium swelling of a polymer in a solvent, particularly when little else is known about the solvent.

Other material properties are also important. Table 2.1, replicated from McDonald and Whitesides (2002) [63], lists several characteristic material properties of PDMS.

Table 2.1: Material properties of PDMS [63].

Property	**Characteristic**
Optical	Transparent; UV cutoff 240 nm
Electrical	Insulating; breakdown voltage 2 x 10^7 V/m
Mechanical	Elastomeric; tunable Young's Modulus, typical value ~ 750 kPa
Thermal	Insulating; thermal conductivity of 0.2 W/(m•K), coefficient of thermal expansion 310 μm/(m•°C)
Interfacial	Low surface free energy ~ 20 erg/cm^2
Permeability	Impermeable to liquid water; permeable to gases and non-polar organic solvents
Toxicity	Non-toxic

Additional mechanical properties of PDMS have been explored in regard to designing microdevices in work by Roca-Cusachs *et al.* (2005) [47]. In this work, the properties were applied to high-aspect ratio structures, an area of particular interest for this thesis. In brief, samples were fabricated using a silicon master template that was created using the focused ion beam (FIB) method. FIB was chosen such that microposts of different heights and diameters could be created with ease on a single surface. The selection of PDMS posts had varying ratios of diameter to height, at a variety of total heights and widths. The total diameter range was between 0.36 μm and 2.29 μm, and each diameter had 4 to 7 different heights, with the total number of combinations equating to 23 [47]. For statistical purposes, a set of 9 individual microposts was created for each set (the posts were arranged in a 3 x 3 grid). From the aspect ratios, and imaging of the resulting posts by SEM, the fraction of microposts that were either stable or ground-collapsed was determined. Using this data, the resulting critical aspect ratio for each micropost diameter was calculated. The critical aspect ratio was also explored under different fluid conditions (thus changing the work of adhesion). The results can be seen in the generalized model displayed in Figure 2.12 and Figure 2.13.

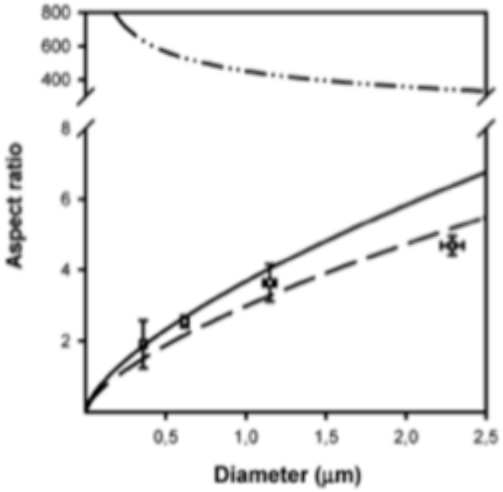

Figure 2.12: Aspect ratio vs. diameter for a variety of microfabricated posts [47].

Reproduced from Roca-Cusachs *et al.* (2005).

The solid line represents the mathematical model, while the dashed line represents experimental results.

The dashed and dotted lines take gravity into account.

If the microfeature is above the model line, it will undergo ground-collapse.

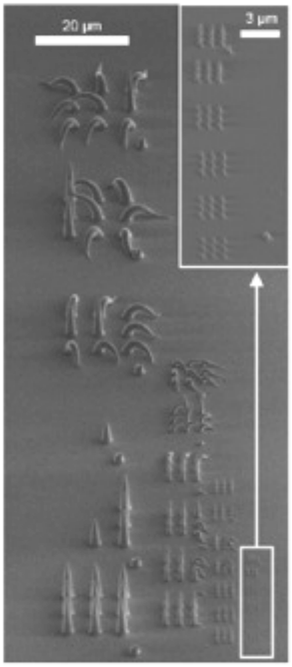

Figure 2.13: Image of different high-aspect PDMS microstructures [47].
Reproduced from Roca-Cusachs *et al.* (2005).
Note the several ratios that have ground-collapsed.

In addition to PDMS as a single material, various material composites have been created and investigated [64]. Surface modification through chemical bonding is an active area of study [16]. An interesting extension of this was evidenced by work in which the PDMS surface was physically modified to yield a super-hydrophobic surface, achieving a contact angle of >160° and a roll-off angle of <5° [55]. This was achieved by direct modification of the PDMS surface with a Nd:YAG laser (532 nm, 20 Hz, energy of 5 J • cm^{-2}). The resulting surface resembled that of a head of cauliflower. The mechanism appeared to follow the formation of nanoparticle-sized droplets that were ejected and solidified on the surface. This process yielded a non-congruent surface that trapped air close to the surface, hence decreasing the liquid contact area. Additionally, the PDMS hydrophobicity was controlled through the creation of corralled domains, referred to as microconvexes. These areas had a 25 μm width, 10 μm depth, and separation (or spacing) of 2 ± 1 μm [55]. By increasing microconvex area, contact angle could be adjusted between 115° and 165° in this case. This technique has applications in self-cleaning of PDMS, as well as generating hydrophobic gradients for enabling or inducing fluid movement.

There have also been efforts to make PDMS electrically conductive [54]. Through the use of silver (Ag) and carbon-black powders, this has been made possible. These studies are highly relevant to this thesis. As shown in Figure 2.14, the concentration and conductivity of each Ag and carbon-black in PDMS composite are graphed. In this work, it was shown that the Ag composites formed were able to be transferred into grooves of a PDMS construct as a paste, cured, and subsequently remained conductive enough to run LED lights; thus demonstrating the promise of this approach for flexible electronics.

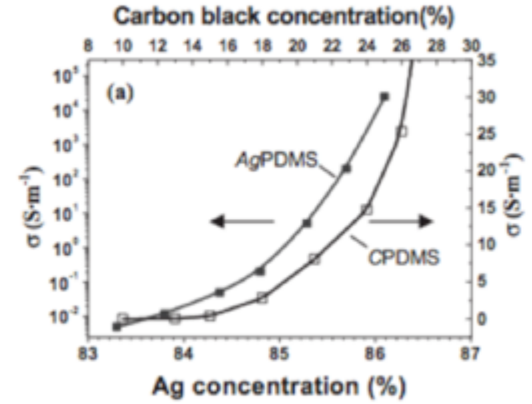

Figure 2.14: Conductivities for Ag and carbon-black in PDMS composites [54].
Reproduced from Niu *et al.* (2007).

This example provides a basis upon which to explore the possibilities for PDMS composites in novel techniques and new microfluidic approaches, such as the creation of new micropumping mechanisms, by overcoming the kinetic limitations presented by pure PDMS. In the following section, current micropumping systems, which employ PDMS and/or other polymeric materials, are discussed.

2.7 Artificial Cilia

Cilia are found almost ubiquitously in nature [65]. Most cells exhibit cilia for the purpose self-propulsion, extracellular fluid propulsion, or sensing stimuli. Physically, cilia can be described as either small hairs or flexible rods, with typical diameters of 250 nm, lengths of ~10 μm, and stroke frequencies between 10 Hz and 30 Hz [66]. As a result, cilia may be thought of as biological micropumping devices to an extent. For instance, human lungs use tracheal epithelium to remove mucus from the lining of the lungs [67]. Extensive studies have been performed surrounding frequency, ciliary motion, and even power output, of cilia in several organisms, providing a good foundation for efforts toward producing artificial analogs [68-70].

Recently, much interest has been garnered toward the creation of biomimetic cilia for use in signaling and μTAS. Much like ATDA, using cilia could allow for 'open droplet' microfluidics, allowing a surface to be active in fluid handling. Actuation performed mechanically, or indirectly (rather than direct actuation as is used for AC eletro-osmosis), may allow for the movement of a wider variety of biological fluids and/or analytes such as blood. The movement of conductive fluids has proven difficult when using direct pumping methods, without causing fluid heating and other undesirable effects [71]. As touched upon in earlier sections, this could prove useful in μTAS for biological and clinical assays. Ideally, by mimicking the biological cilia approach, the difficulties of moving parts at the microscale could perhaps be avoided.

To date, there have already been efforts made toward developing artificial cilia for use in microfluidic handling and sensing, as will be explored in the next section.

2.7.1 Application of Artificial Cilia

Some efforts toward developing artificial cilia have been very fruitful, producing a small surface for the micromanipulation of objects, and in some cases even presenting solutions for micro-satellite docking [72]. The creation of Fe_3O_4 magnetite nanoparticles in solution (a ferrofluid) have been utilized to create ferrofluid/PDMS composite nanostructures [73]. These rods were created using a poly(carbonate) (PC) negative mold, which was in turn loaded with this magnetite/PDMS composite material. After loading and curing, the PC mold was then dissolved in dichloromethane, leaving behind the PDMS composite structure.

The resulting rods were within the micron and nanometer scales, sometimes exhibiting aspect ratios of up to 125 in liquid media. The diameters had a characteristic size of hundreds of nanometers, and the lengths were on the order of tens of microns (Figure 2.15). These rods were then manipulated using a permanent magnet in which they displayed rotational and lateral movements. Note that these were not able to form regular arrays. The rods began to collapse and adhere to one another irreversibly at aspect ratios >50 using this method.

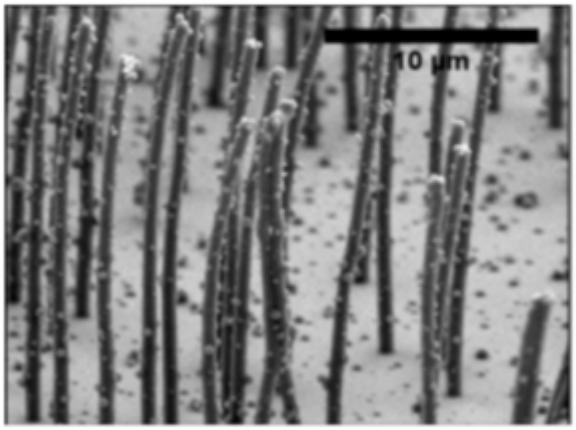

Figure 2.15: SEM image of artificial cilia [73].
Reproduced from Evans *et al.* (2007).

Another application was inspired by the filiform hair on the cerci of crickets, in which microsensors were fabricated for use in acoustic flow sensing [74]. These were created using sacrificial poly-silicon methods to create silicon-nitride membranes, and SU8 polymeric photoresist for creation of the artificial hairs (Figure 2.16) [74].

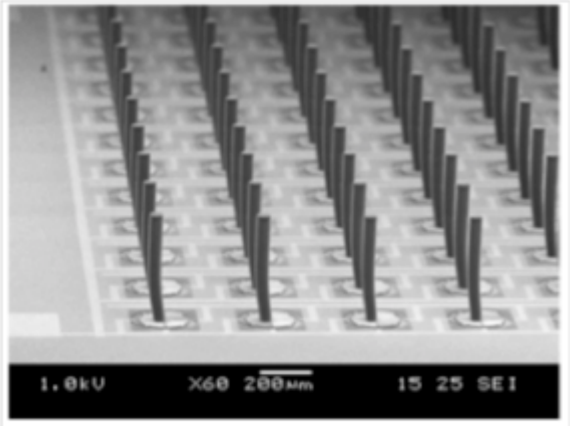

Figure 2.16: SEM image of an array of microsensor hairs [74].
Reproduced from Krijnen *et al.* (2006).

While not true cilia, the use of PDMS micropillars has also been used, to directly measure the mechanical forces that single-cell organisms exhibit on their environment thereby providing another interesting application of these microstructures [75]. Active mixing with artificial cilia has been modeled somewhat extensively, showing that even two simple cilia are enough to create exponential mixing, that overall pumping performance is reliant on phase lag of neighboring cilia, and that the fluid propelled is linearly proportional to the film area swept [76-78]. The details of these analyses are relatively extensive and will not be further discussed in this review.

However, these models generally assume the use of magnetic actuation, and that the cilia exhibit an identical deformation pattern as those of natural cilia, which is rather complex. These models shed light on the associated power and recovery strokes (i.e. forward and back strokes), but raise questions in terms of how far the mimicking of this complex motion should go. By assuming high aspect-ratio beams to be used in artificial systems, this seems logical. But perhaps the use of protrusions that are mechanically stiffer (through the use of either a composite material or different configuration - a cone for instance) may be a topic that would avoid the ground-collapse effect observed with PDMS, and perhaps remove some of the complexity associated with modeling these systems as well [47].

There have been several studies that utilize artificial cilia to actively mix fluids as well as induce fluid movement. These have even been created using inkjet printing technology with the integration of liquid crystals (azobenzene dyes) into two photoactive monomers to allow for selective actuation based on the wavelength of exposed light [79]. Fluid flow was not achieved in this case, but large deflection of the cilia was observed. For the active mixing of fluid, a working system has been demonstrated, although not based solely upon a polymeric technology. This system utilizes poly(imide) for the cilia (Figure 2.17), but the rest of the device is manufactured using conventional methods found in MEMS.

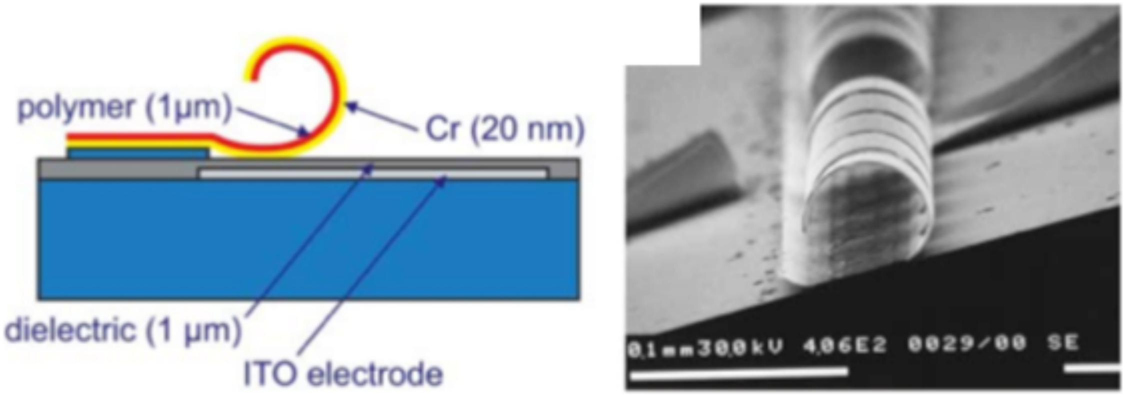

Figure 2.17: Poly(imide)-based cilia for micromixing [66].
Reproduced from Toonder *et al.* (2007).

In other work, a polymer-based system utilizing a Fe-C-PDMS composite was created to actuate fluid, but only achieved fluid velocities of 0.5 mm s^{-1}. The composite used up to 3 % (by volume) of the Fe-C nanoparticles (the Fe is covered in C, preventing oxidation), but exhibited the undesirable characteristic of having to remain wet, otherwise irreversible sticking and destruction of the cilia was observed [6, 66, 79]. Due to the attraction of composite particles between cilia, swelling was needed to maintain the structure. Additionally, there was a need to provide cross-linking of the PDMS to maintain the nanoparticles on the structure [6, 66, 79].

Overall, although further work is required, artificial cilia point to the potential to fabricate arrays of micropillar-like structures, and the promise of the open droplet microfluidic handling approach.

2.8 Composite Polymeric Material Approaches

As this thesis is centralized around the development of electrically actuated micropost arrays through a composite polymeric material approach, promising composite materials have been reviewed in the following sections, as candidates for use in micropost array fabrication during this project.

2.8.1 Poly(aniline)-Loaded Poly(dimethylsiloxane)

The use of a PDMS composites containing camphorsulfonic acid-doped PANI particles has yielded interesting results in the literature [80]. Physically, PANI has good thermal and environmental stability, low density, and ease of conductivity control (through the use of protonic acids). Therefore, these material properties allow for the control of particle properties without the need for modification of the PDMS. Also reported is the reversibility of polarization in the presence of an AC electric field, allowing for a switching effect to take place; ideal for the asymmetric movement needed in artificial cilia or actuatable micropost arrays [6].

More specifically, in the study by Fahrni *et al.* (2009), the PANI particles used had a mean diameter of 23.5 µm ± 3.58 µm, but were able to be well dispersed throughout PDMS [6]. Some hysteresis (residual polarization of the particles even after the electric field was turned off) was observed. The authors accounted for this hysteresis as being due to the rather large crystalline particles that helped to maintain polarization. To overcome the hysteresis observed, and thus make this approach applicable to artificial cilia or actuatable microposts, smaller domains would likely have to be created, possessing negligible irreversible polarization.

There have been efforts to create PANI thin films, although these methods would need to be adapted for use with PDMS [8, 81]. However, a promising approach could lie with the use of micro-contact printing [82]. Through such methods, it could be possible to pattern PDMS surfaces, and those with high-aspect ratio surfaces, effectively reducing hysteresis. This could also be accomplished through using PANI nanoparticles [83].

When a sample of 10 % (volume) PANI particles in a composite membrane with PDMS (with a size of 1 x 2 x 27 mm) was exposed to an electric field in a silicon oil bath (viscosity = 100 CSt) there was deflection observed toward the anode [83]. Reversal in field polarity changed the direction of deflection, as expected. The highest deflection of the film at 10 % (by volume) particles occurred at 520 V/mm (Figure 2.18). Undoped PANI particles produced no noticeable deflection.

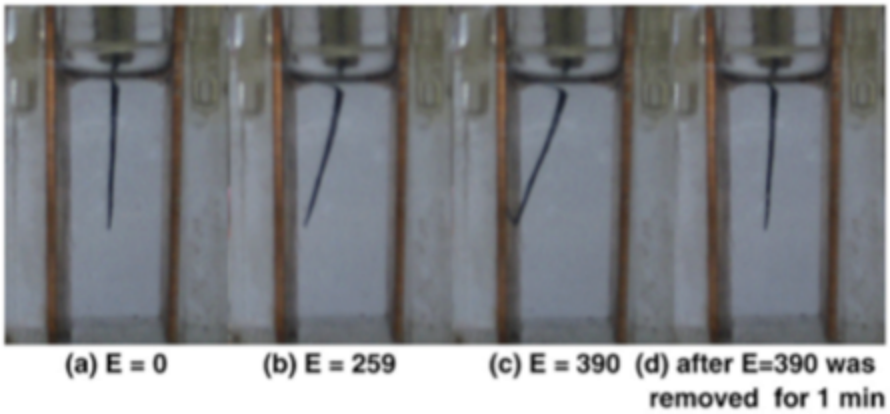

Figure 2.18: PANI/PDMS composite films being deflected by an electric field [8].
Reproduced from Zaharias *et al.* (2006).

Based on the results of this study, it is possible that a 2-D array of PANI-loaded PDMS composite microhairs could be well suited for open droplet microfluidic applications. It is also possible that through the use of finer PANI particle sizes, that hysteresis could be minimized.

2.8.2 Titanium Dioxide-Loaded Poly(dimethylsiloxane)

Research to date has also highlighted that the deflectability of bulk TiO_2-loaded composite polymers is possible under exposure to static electric fields. More specifically, as exemplified by the work of Zrinyi *et al.* (2000), TiO_2/PDMS gels were deflected under high voltage fields (Figure 2.19) [9]. Maximum deflection was achieved at 9 kV and 3 cm separation, or with an electric field strength of 300 kV/m.

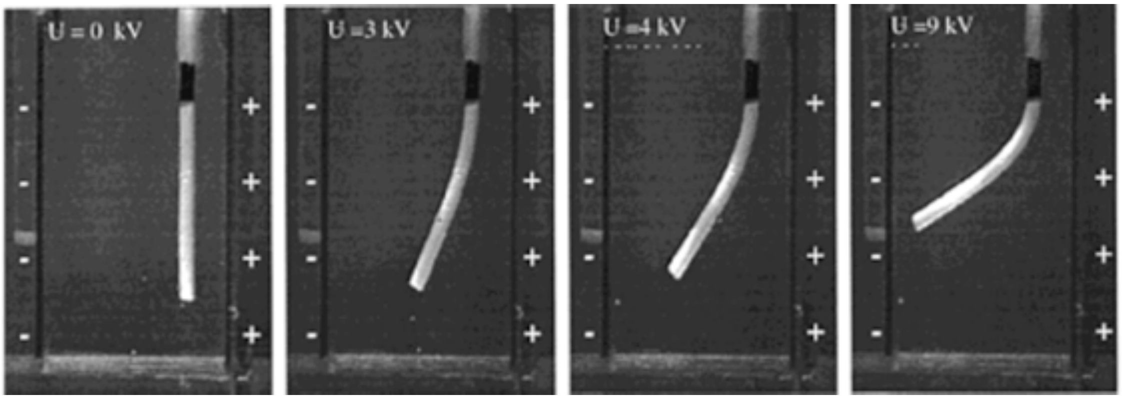

Figure 2.19: TiO2/PDMS gels deflected under electric fields [9].
Reproduced from Zrınyi *et al.* (2000). Electrode plates (50mmL, 50mmH, 1.2mmW) with 30 mm spacing.

Coupled with additional work in the literature that has documented the successful use of TiO_2-loaded PDMS for use in actuators and beyond [10, 84], TiO_2-loaded PDMS presents a promising composite material for examination during the current study. Its ease of procurement, low cost, widespread use throughout industry, variety of surface coatings, and nanoparticle size makes TiO_2-loaded PDMS a very promising material for this project. However, it is acknowledged that alternative particles could be used to load PDMS, such as silica, and could be included as future work related to this project.

2.9 Summary

Microfluidics and microhandling technologies encompass a broad field of study, with many exciting new directions. The use of conventional micropumping methods has evolved to include direct methods for fluid actuation using both DC and AC electro-osmosis. Micropumping is now expanding to include biomimetic methods for indirectly handling fluids, through the development of artificial cilia and other such structures, so as to widen the heterogeneity and types of fluids that might be manipulated using an open droplet microfluidic approach. It is possible that through implementing a moderately conductive polymeric composite material with a micropost array surface geometry, open droplet manipulation could be achieved through indirect electrical actuation of microposts, forming the basis for this thesis.

Chapter 3

Materials and Methods

3.1 Materials

All chemicals were purchased from Sigma-Aldrich Canada Ltd. (Oakville, ON) unless otherwise stated, and were used as received.

3.2 Bulk Material Development and Characterization

3.2.1 Composite Polymer Film Preparation

Two-part clear PDMS was prepared using the SYLGARD® 184 Elastomer Kit from Dow Corning (Ellsworth Adhesives, Toronto, ON) in weight-based ratios of 10 parts PDMS to 1 part heat cure (10:1 w/w) and 5 parts PDMS to 1 part heat cure (5:1 w/w). Each PDMS polymeric film was fabricated by first combining the PDMS and crosslinking agent together in a 4 oz. poly(propylene) mixing cup (McMaster-Carr, Chicago, IL) with a wooden mixing paddle. After mixing, any resulting bubbles were removed by degassing the PDMS mixture under vacuum for at least 1 h, or until no bubbles were present. The degassed PDMS/cross-linker mixture was poured into a stainless steel mold (3 mm film thickness), left to evenly spread throughout the mold, covered with the mold top, and placed within a stainless steel, heated hydraulic press for curing (1 h, 110°C). The mold used complies with ASME specifications. Finally, the cured PDMS film was contact-cooled in a secondary stainless steel hydraulic press (1 h, room temperature) and removed for subsequent characterization. This overall process was repeated for additional PDMS film preparation, as well as for the fabrication of various PDMS composite films.

Initially, PDMS loaded with PANI microparticles (1-3 μm mean particle size, Sigma 561134-10G) was investigated as a polymeric composite material from which to ultimately prepare the micropost arrays. Using methods analogous to those presented for the preparation of the unloaded PDMS films, 20 % (w/w) PANI-loaded PDMS mixtures were prepared by thorough mixing, and combined with the heat cure agent. PANI-loaded PDMS films were then fabricated using identical degassing, molding, curing, and cooling steps, as previously outlined for the preparation of unloaded PDMS films.

Based on the results obtained for the PANI-loaded PDMS films, PDMS loaded with TiO_2 nanoparticles was also investigated as a potential polymeric composite material for use in micropost fabrication. Titanium has mainly favourable properties compared to PANI, particularly in regards to cost. Evonik Industries (Piscataway, NJ) Aeroxide® brand TiO_2 nanoparticles were obtained and used to prepare TiO_2-loaded PDMS films. The Aeroxide® TiO_2 nanoparticle size distributions were measured using dynamic light scattering (DLS) techniques via a Malvern Instruments Zetasizer.

Using similar film preparation methods, hydrophilic TiO_2 nanoparticles (P25 Aeroxide®), or hydrophobic negatively charged TiO_2 nanoparticles (NKT90 Aeroxide®) were combined with PDMS in varying mass percentages (10, 20, and 30% (w/w) TiO_2) to yield a range of different bulk film formulations. To ensure even nanoparticle dispersion throughout the PDMS, the TiO_2/PDMS mixtures were sonicated for 1 h (50-60°C). Following sonication, the PDMS crosslinking agent was added to the TiO_2/PDMS mixtures, and the TiO_2/PDMS films were made following like methods as those employed to fabricate the unloaded PDMS films and the PANI-loaded PDMS films.

3.2.2 Macroscopic Characterization and Scanning Electron Microscopy

The resulting pure polymer, PANI-loaded, and TiO_2-loaded PDMS films were macroscopically inspected for overall physical appearance, as well as any qualitative differences in material surface properties, malleability, and noticeable bubbles or voids. All samples were digitally photographed using a Canon Powershot A640 digital camera (macro setting).

To qualitatively assess the particle dispersion throughout the TiO_2-loaded PDMS films, representative film samples were examined using SEM. Each film formulation was mounted onto a microscopy stud using carbon tape, gold-sputtered, and viewed under a Hitachi S-2300 microscope (working distance 10 mm, accelerating voltage 10 kV).

3.2.3 Young's Modulus Determination

Based on the results obtained from the macroscopic and microscopic evaluation of the bulk polymeric composite films, select formulations were identified as more optimal for use in subsequent sample fabrication. These selected formulations were in turn subjected to further bulk material characterization. Young's Moduli were determined for the polymeric composite films, as compared to pure PDMS films, using an Instron® 3369 Dual Column Tabletop testing system (Figure 3.1) with Bluehill® software, Version 1.13. The Young's Modulus is useful for predicting the actuation behaviour of PDMS and PDMS-composite microposts.

Figure 3.1: Instron® 3369 Dual Column Tabletop testing system.

To test the films, tensile bars were prepared through placing the films in a steel die (ASTM D412), and punching out the desired testing shape (Figure 3.2). No visible defects (such as bubbles or ripples) were observed upon inspection of the bulk films produced. Excellent uniformity of film thickness was observed across all tensile bars. Differences in film thickness were minimized through depositing identical volumes of mixture into each plate during film preparation.

Figure 3.2: Tensile bar die.

All composite samples were measured over low elongation (0 – 0.2 mm), with data expressed as means with standard deviations (*n*=10). Pure, non-composite, PDMS tensile bars were also tested as controls, with a sample size of 7 (*n*=7) due to the fact that 3 tensile bars failed during tensile bar preparation.

3.2.4 Contact Angle Measurement

Following Young's Moduli determination, contact angle measurement was performed on selected film formulations using a VCA goniometer (Figure 3.3) equipped with VCA Optima XE software (AST Products Inc., Billerica, MA) and 4 μL volume (or lower in volume) deionized (DI) water droplets delivered via micropipette to aid in droplet ejection. This droplet volume range was used to ensure that droplets would be in the low Bond regime. The low Bond regime corresponds to low Bond numbers ($B \ll 1$), which express the ratio of gravitational force to capillary force/surface tension. Therefore, these droplets would remain unaffected by the force of gravity and therefore yield more accurate contact angle measurements.

Figure 3.3: VCA goniometer used for contact angle measurements.

Contact angle measurements were determined using ImageJ image analysis software (National Institutes of Health) equipped with BIG>Drop (École Polytechnique Fédérale de Lausanne); measured in the form of the righthand side contact angle (θ_R) and the lefthand side contact angle (θ_L) for each droplet, based on pixel fits of the resulting image. These angles may also be reported as the advancing (θ_A) and receding (θ_R) contact angles. In this work, the contact angle measurements were expressed as lefthand and righthand angles to identify any differences surrounding which side was advancing/receding for each droplet. The righthand (θ_R) and lefthand (θ_L) contact angles determined via image analyses were in turn used to calculate the CAH for each investigated droplet. All bulk film samples were measured for their contact angles in triplicate (*n*=3).

3.2.5 Bulk Material Deflection

A major step of this project worked toward being able to test the deflection of novel micropost arrays in the presence of an electric field. As a result, a custom-designed set of electrodes was required, and was assembled using aluminum tape and glass slides in the laboratory. This electrode set was connected to a high-voltage DC power supply (Gamma High Voltage ES20P-5W/DAM, Ormond Beach, Florida, USA) using standard alligator clips and copper electrical wires. During deflection experiments, the power supply was switched on, and the voltage varied so as to subject samples placed between the electrodes to specified electric field strengths. Figure 3.4 shows the electrodes (Figure 3.4a) and the DC power supply (Figure 3.4b) used in bulk material deflection experiments. This apparatus was also used during the micropost deflection experiments described in Section 3.5.2.

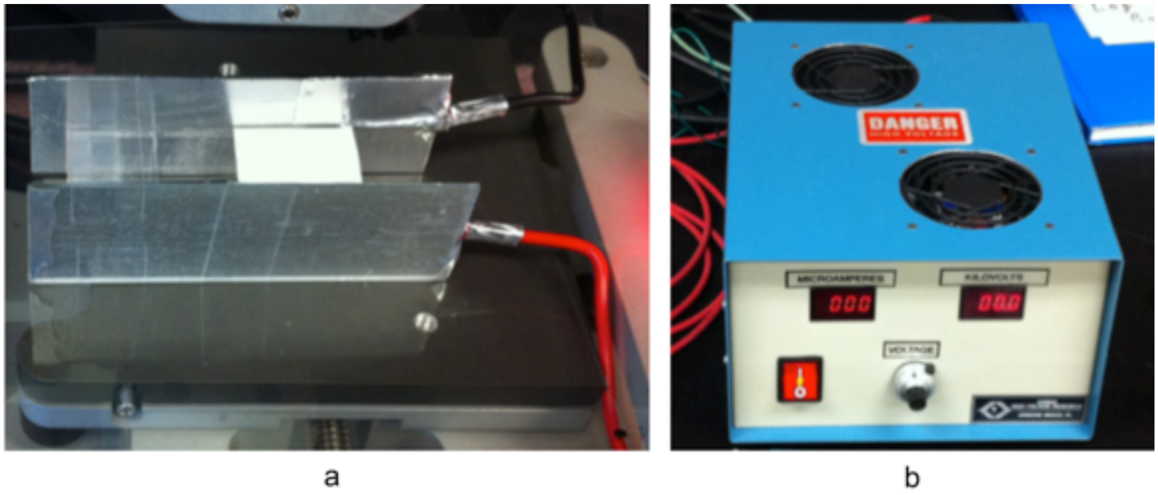

Figure 3.4: Deflection experimental apparatus.
(a) Customized electrodes, and (b) DC power supply.

Bulk material deflection tests were performed using TiO_2-loaded PDMS cylinders of varying weight percent TiO_2 (0, 10, and 20 % (w/w)) prepared using glass "melting point" capillary tubes. Un-crosslinked PDMS was loaded with hydrophobic (NKT90) TiO_2 nanoparticles and deposited into a 50 mL volume plastic syringe. To prevent material from leaking from the syringe, the extrusion end was sealed with parafilm. Following syringe loading, the material was mixed with a wooden stirrer and then sonicated for 1 hour at 50°C to reduce viscosity and better disperse the TiO_2 nanoparticles. After sonication, the mixture was allowed to cool to room temperature, the crosslinking agent was added and combined with the mixture using a stir stick, and the material was allowed to rest in the vacuum dessicator for 10-20 minutes at room temperature to remove any air bubbles. The plunger was placed in the syringe, the parafilm was removed from the other end of the syringe, the material was extruded until it was visibly homogenous, and a 22-gauge hypodermic needle was screwed onto the syringe end to facilitate in filling the capillary tubes. Finally, the TiO_2/PDMS mixture was injected into glass capillary tubes sealed at one end with aluminum tape to prevent material leakage, and crosslinked in an oven (120°C) for at least 20 minutes. To obtain the cylindrical samples following crosslinking, the glass tubes were manually cracked, and all shards were removed through lubrication of the samples with isopropanol. Final samples for use in bulk material deflection experiments were either 500 microns or 1 mm in diameter, and were trimmed to 50 mm in length.

Deflection of cylindrical samples was assessed using a gap spacing of 24 mm, a nominal voltage of 7.2 kV, and an electric field strength of 300 kV/m. Grid paper with major and minor gridlines (in centimeters and millimeters, respectively) was used in conjunction with the electrodes/power supply apparatus to visually follow the position of each sample as a function of electric field strength. Samples were rinsed with ethanol immediately prior to testing so as to remove any dust.

3.3 Micropost Design

3.3.1 Design Algorithm Development

Towards the aim of fabricating electrically actuatable micropost arrays, mathematical modeling was employed to make predictions for viable baseline geometries. Microsoft Excel was employed for solving the developed model, using the Solver algorithm.

The goals of this model were to mathematically predict the behavior of super-hydrophobic surfaces comprised of micropost arrays that would be subject to minute electro-physical forces, and to therefore allow for droplet detachment and free movement, especially given the low Bond numbers involved (with droplet volumes on the scale of 1 to 10 uL).

In this model, the contact angle was calculated using the Wenzel method and the Cassie-Baxter method, to aid in designing stable surfaces for microfluidic manipulation. To predict the final ratio of the micropost height to diameter, work by Roca-Cusachs *et al.* (2005) was particularly applicable. In their work, using the moment of inertia (I) for a circle (Equation 14);

$$I_{circle} = \frac{\pi a^4}{64} \qquad \text{Equation 14}$$

where a was defined as Equation 15;

$$a = \left[\frac{16\left(1-v^2\right)}{\pi E} W \right]^{1/3} b^{2/3} \qquad \text{Equation 15}$$

and v the Poisson ratio, W work of adhesion, E the Young's Modulus of the material, and b the micropost diameter. Using this information, Roca-Cusachs *et al.* (2005) developed the relationship between micropost height (h) and diameter (or base, b) for a round (or circular) micropost shape (Equation 16);

$$\left(\frac{h}{b}\right)_{crit}^{circle} = \frac{\pi^{5/3}}{2^{11/3}3^{1/2}}(1-v^2)^{-1/6}\left(\frac{E}{W}\right)^{2/3} b^{2/3} \qquad \text{Equation 16}$$

Expanding this approach to apply to additional micropost shapes, during the current study the moments of inertia (I) for a cross and hexagram were used to re-derive the Roca-Cusachs *et al.* (2005) relationship (h/b) in terms of cross and hexagram micropost shapes as follows. Given that the moments of inertia (I) for a cross and hexagram are, respectively (Equations 17 and 18);

$$I_{cross} = \frac{29a^4}{81} \qquad \text{Equation 17}$$

$$I_{hex} = \frac{11a^4}{216\sqrt{3}} \qquad \text{Equation 18}$$

and through defining the strain energy (U_S) as did Roca-Cusachs *et al.* (2005) in Equation 19;

$$U_S = \frac{EI\pi^2}{2h} \qquad \text{Equation 19}$$

dU_S was solved for and subsequently inserted into the Roca-Cusachs *et al.* (2005) expression for each different shape. Finally, the following relationships between the micropost height and diameter (or base) were obtained for a hexagram shape (Equation 20), and a cross shape (Equation 21), respectively;

$$\left(\frac{h}{b}\right)_{crit}^{hexagram} = \frac{11^{1/2}\pi^{7/6}}{3^3 2^2} 2^{-2/3}(1-\nu^2)^{-1/6}\left(\frac{E}{W}\right)^{2/3} b^{2/3} \qquad \text{Equation 20}$$

$$\left(\frac{h}{b}\right)_{crit}^{cross} = \sqrt{\frac{29}{81}}\,\frac{\pi^{7/6}}{2^{2/3}3^{1/2}}(1-\nu^2)^{-1/6}\left(\frac{E}{W}\right)^{2/3} b^{2/3} \qquad \text{Equation 21}$$

These resulting expressions were incorporated into the predictive model, along with the round-shaped Roca-Cusachs *et al.* (2005) expression, to aid in predicting micropost geometries that would yield stable, super-hydrophobic surfaces.

Additionally, given the method of Yeo *et al.* (2010) [24], the predicted contact angles from the model were graphed as a function of micropost spacing for a given micropost diameter and shape. Specifically, micropost spacing was chosen in a region in which the Cassie-Baxter result showed micropost stability. This is to say, a region in which micropost spacing would result in a fall into a lower-energy state (the Wenzel condition) [24]. This Cassie-Baxter micropost spacing was in turn checked against the micropost spacing required to avoid lateral micropost collapse conditions, given the micropost height needed for both deflection and to avoid ground collapse. Different micropost shapes were taken into account to increase surface hydrophobicity [23, 85]. This overall process was iterated using the model until an optimal design was chosen, as represented by the design algorithm depicted by Figure 3.5.

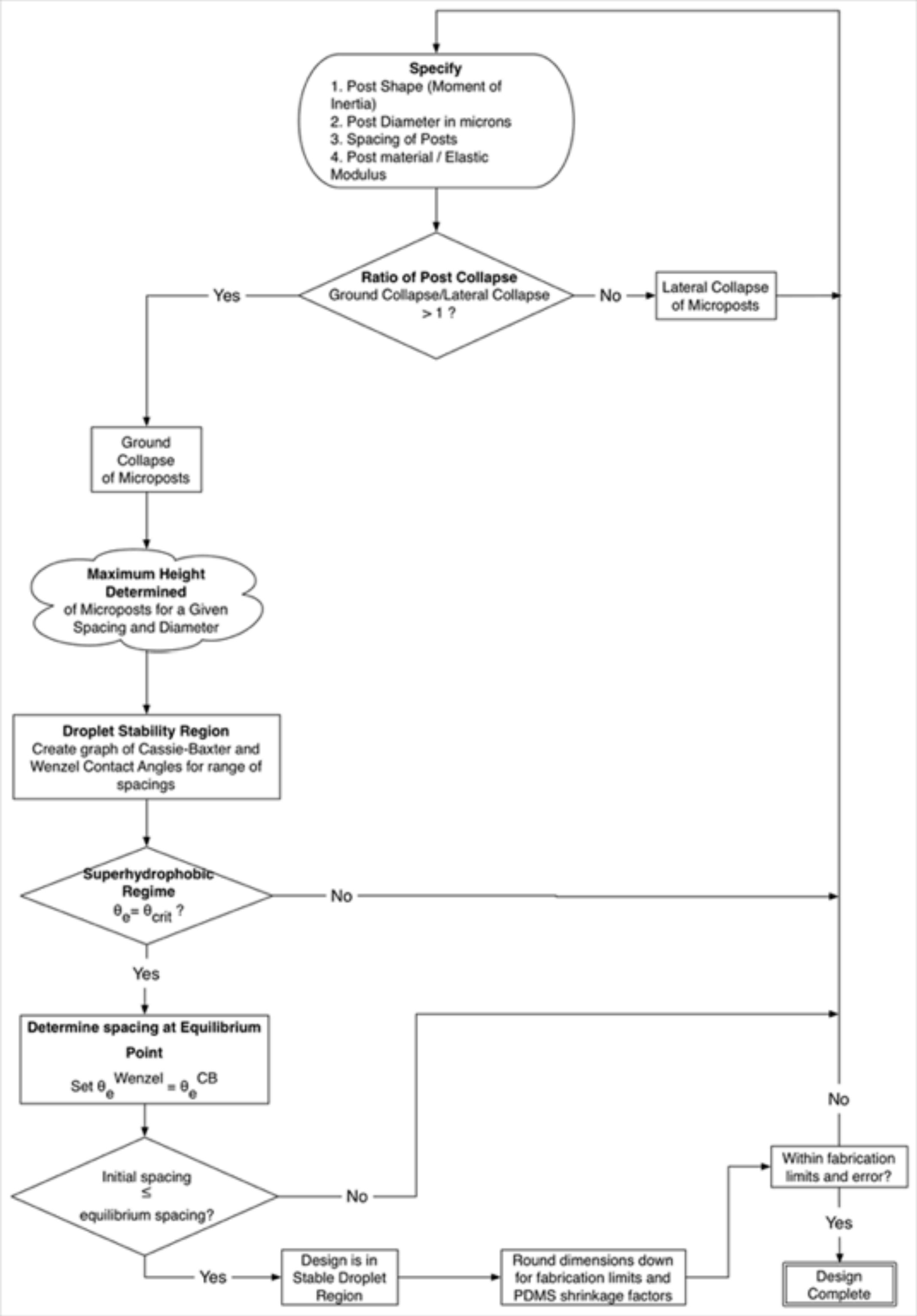

Figure 3.5: Design algorithm for the development of customized microposts.

The end result of this process was intended to lead to the development of a super-hydrophobic surface with microposts that would be resilient to both ground and lateral micropost collapse, yet also deflectable in the presence of an electric field. In the model, micropost collapse was calculated with varying Young's Moduli values (as determined through measurement as described in Section 3.2.3), given that these moduli change as a function of TiO_2 content in the PDMS. Micropost ground collapse was also calculated assuming partial droplet penetration by the microposts, to avoid the occurrence of micropost collapse beneath droplets during micropost actuation. This assumption was handled within the model through modifying the value of the work of adhesion to account for the use of water (as opposed to air) and assuming complete submersion of the surface.

3.3.2 Computer-Aided Design and Fabrication of Micropost Array Photomask

Upon determining the designed micropost geometry from the mathematical model, these outputs were in turn applied toward the CAD of photomasks using L-Edit Pro software (Tanner Research, Inc., Version 13.0). Nine equally-sized square arrays of microposts, varying in post geometry (or shape), were drafted by CAD to fit onto a 4-inch diameter silicon wafer, while taking into account the specific micropost geometries.

A custom-designed photomask was manufactured for this work using traditional mask fabrication techniques via laser etching of gold-plated borosilicate glass. After completing the photomask design within L-Edit software, the electronic file was uploaded to the Alberta NanoFab facility located in Edmonton, AB, for subsequent processing to yield the desired photomask for use in micropost fabrication, as outlined in Section 3.4.

3.4 Micropost Array Fabrication

TiO_2-loaded PDMS micropost arrays were fabricated using varying concentrations of NKT90 (hydrophobic) TiO_2 (10 % (w/w) and 20 % (w/w) TiO_2) using the methods described herein, and compared to unloaded PDMS microposts of like lengths. Specifically, 10 % (w/w) TiO_2, 20 % (w/w) TiO_2, and unloaded PDMS microposts were each fabricated at post lengths of 100 μm, 200 μm, and 300 μm. Table 3.1 lists the various micropost sample groups (*n*=9) prepared during this work, and characterized as described in Section 3.5. Unless otherwise specified, all micropost array fabrication steps were performed in a Class 1000 Clean Laboratory located in the QFAB micro- and nano-fabrication facility in Jackson Hall, Queen's University.

Table 3.1: Micropost sample groups investigated.

Group	Formulation	Micropost Length
1	Unloaded (0 % (w/w) TiO_2) PDMS	100 μm
2	Unloaded (0 % (w/w) TiO_2) PDMS	200 μm
3	Unloaded (0 % (w/w) TiO_2) PDMS	300 μm
4	10 % (w/w) TiO_2-loaded PDMS	100 μm
5	10 % (w/w) TiO_2-loaded PDMS	200 μm
6	10 % (w/w) TiO_2-loaded PDMS	300 μm
7	20 % (w/w) TiO_2-loaded PDMS	100 μm
8	20 % (w/w) TiO_2-loaded PDMS	200 μm
9	20 % (w/w) TiO_2-loaded PDMS	300 μm

3.4.1 Master Template Fabrication

3.4.1.1 Silicon Wafer Preparation

In preparation for fabricating the master micropost template, a 4-inch diameter silicon wafer was thoroughly cleaned. Wafer tweezers were used to carefully remove a silicon wafer from the resealable wafer plastic storage case. Moving to the fume hood in the QFAB Clean Laboratory, the wafer was thoroughly rinsed with DI water, ensuring the surface was entirely wetted. Without permitting the wafer surface to dry, the wafer was next thoroughly rinsed with isopropanol (99.9 %) during which the wafer was rotated and tilted alternatively to ensure comprehensive wafer coverage. Once visual inspection indicated no residual water remained dispersed throughout the isopropanol, the wafer was washed with acetone (100 %) following identical methods as those used for the isopropanol rinse. Finally, the wafer was subjected to an additional isopropanol rinse, followed by a second rise with DI water.

Without allowing the wafer surface to dry, the water from the final rinse was displaced from the wafer with the aid of a pressurized nitrogen jet (15 psi) by applying the jet in a sweeping motion over the wafer. A dust-free laboratory wipe was used to absorb water drips falling from the wafer edges until the nitrogen jet effectively drove all water from the wafer surface.

To ensure removal of any residual liquid from the wafer, wafer tweezers were used to transport the wafer onto a hot plate, and the wafer was dried for 20 minutes at 120ºC. After the 20-minute drying time was complete, the wafer was removed using tweezers and left to cool to room temperature on a dust-free laboratory wipe in the Clean Laboratory.

3.4.1.2 Photoresist Preparation

While the cleaned silicon wafer dried on the hot plate, the photoresist needed to create the micropost master template was prepared. For this work, SU8-50 photoresist was selected and dispensed into a DART plastic mixing cup. Using a 10 mL-volume McMaster and Carr plastic syringe, ~10 mL of SU8-50 were manually drawn into the syringe from the cup, as slowly as possible and at a qualitatively constant rate to minimize air uptake into the syringe. The SU8-loaded syringe was permitted to rest vertically for at least 20 minutes, or until visible inspection showed that no remaining air bubbles were trapped in the viscous SU8 photoresist.

3.4.1.3 Photoresist Spin-Coating

Upon permitting the SU8 to gravity settle, thereby clearing all bubbles from the SU8 in the syringe, the SU8 was deemed ready for spin-coating onto the cleaned silicon wafer. After drying, the wafer was carefully centered onto the chuck of the QFAB vacuum spin-coater (Laurell Technologies Corporation) using wafer tweezers.

Once properly centered, the vacuum was initiated to retain the wafer in place on the chuck. The top of the spin-coater chamber was closed, and the SU8-loaded syringe was wiped free of any undesirable dripping using a dust-free laboratory wipe. Between 2-4 mL of SU8-50 were manually extruded from the syringe onto the center of the silicon wafer within the spin-coater.

To coat the deposited SU8 evenly across the wafer to the desired thickness, a spin-coating program was adapted from established methods for ultra-thick SU8 film preparation [86]. Initially, the spin-coater was run at 500 RPM for 30 s, to uniformly distribute the SU8 across the silicon wafer. The speed was increased to 1250 RPM for 30 s, then ramped down to 800 RPM for an additional 30 s. Using a 10 mL disposable plastic dropper device, ~1-2 mL of edge bead remover (EBR PG, MicroChem) were added to the wafer edge during spinning (800 RPM) so as to remove any SU8 that may have built up along the edge. Finally, the spin-coater speed was ramped up to 2500 RPM for 10 s, before stopping the spin-coater and allowing the SU8 to rest on the wafer for at least 30 s.

Following spin-coating, the vacuum was released, and the wafer was removed from the spin-coater chamber using wafer tweezers and transferred onto a hot plate. The SU8-coated wafer was heated at 65ºC for 10 minutes, after which the hot plate temperature was ramped up to 95ºC for 30 minutes. After soft baking, the SU8-coated wafer was removed from the hot plate and allowed to cool at room temperature for at least 10 minutes.

Through following the outlined spin-coating protocol, a 100 μm-thick layer of SU8-50 was effectively applied to the surface of a 4-inch silicon wafer. This provided the base from which the 100 μm-long micropost master template could be made, as outlined in the following sections. To fabricate a 200 μm-long micropost master template, an additional layer of SU8-50 was applied to the already-coated wafer (totaling two layers of SU8-50 on the wafer), via identical methods as those previously described for preparing the 100 μm-long micropost master template. Similarly, for the preparation of a 300 μm-long micropost master template, two additional layers were applied to the initial layer of SU8 (totaling three SU8 layers on the wafer).

3.4.1.4 Photoresist Exposure and Selective Photosensitization

After the desired number of SU8-50 photoresist coats (1, 2, or 3) were applied to the wafer to yield the preferred photoresist thickness (~100 μm, ~200 μm, or ~300 μm), the coated wafer was allowed to rest for 10 minutes. During this period, the Oriel mask aligner (Model 83210) was switched on, and the mask aligner lamp power supply was set to either 800 W or 1000 W. The shutter time was set to either 65 s or 70 s.

Using the custom-designed photomask ordered from the Alberta NanoFab facility (Edmonton, AB), the SU8-coated silicon wafer was selectively exposed to broad spectrum UV light (350 - 500 nm). Once again working carefully within the QFAB Clean Laboratory, the photomask was manually inserted into the frame on the mask aligner. Lifting the frame cover, the SU8-coated wafer was lightly placed onto the vacuum stage using wafer tweezers. The frame cover was replaced over the wafer and the mask aligner stage was then raised until almost in contact with, but not directly touching, the frame and the photomask. The main system vacuum was switched on to effectively contact the wafer with the photomask. Finally, the entire stage was manually returned to lie beneath the main lens on the mask aligner, and the shutter was manually triggered; exposing the spun-coat wafer to broad spectrum UV light (350 - 500 nm) for the desired time period, thereby selectively photosensitizing the SU8 on the wafer.

3.4.1.5 Photoresist Crosslinking and Microfeature Developing

After exposing the photomasked SU8-coated wafer using the mask aligner, the wafer was removed from the stage and placed onto the hot plate for 10 minutes at 65ºC and then 30 minutes at 95ºC, to effectively crosslink the photo-exposed microfeatures. Following crosslinking, the coated wafer was permitted to gradually approach room temperature for 10 minutes, through switching the hot plate off, but leaving the wafer on the hot plate to cool.

To remove any unexposed and therefore uncrosslinked SU8 from the wafer surface, SU8 Developer (MicroChem) was applied to the wafer within a 6-inch diameter glass petri dish. After immersing the wafer in the Developer, the glass petri dish cover was placed over the wafer, and the entire petri dish was placed over a water-filled glass beaker. The beaker and wafer-containing petri dish were placed on a water-filled 500 mL plastic beaker submerged in a sonicating bath and the wafer was sonicated and monitored at 5-minute intervals until macroscopic inspection revealed complete removal of residual uncrosslinked SU8. After each 10-minute interval of sonication, the SU8 Developer was replaced with fresh Developer. This was performed by transferring the wafer to a new petri dish containing fresh Developer.

3.4.1.6 Master Template Drying and Silanization

After developing, the wafer was carefully removed from the Developer solution. To avoid undesirable microfeature collapse, the wafer was not permitted to air dry. Rather, to remove the residual Developer, the excess was gravity drained into a petri dish, and a low-pressure nitrogen jet (~5 psi) was applied in a sweeping motion across the microfeatures to carefully remove any excess liquid. Once the wafer was largely free of Developer, the coated wafer was placed on a hot plate for 30 minutes at 120ºC to hard-bake the SU8. The micropost master template on the silicon wafer was permitted to cool through switching off the hot plate, and leaving the wafer on the hot plate, thereby allowing both the wafer and the hot plate to approach room temperature together.

To render the surface of the SU8-based micropost master templates chemically inert, the SU8 masters were silanized. For each master template, 3 drops of silanizing agent (trichloro(1*H*,1*H*,2*H*,2*H*-perfluorooctyl)silane, Sigma 448931) were added to an unsealed 5 mL glass vial, and the vial and the master were placed in a vacuum dessicator for 3 h. The resulting silanized micropost master templates were stored in resealable plastic wafer containers until their use in preparing PDMS-based negative micropost molds, as described in the following section.

3.4.2 PDMS-Based Negative Mold Fabrication

To prepare the PDMS solution to make the PDMS-based negative molds, for subsequent use in fabricating the 100 μm-, 200 μm-, and 300 μm-long microposts, comparable methods were followed as those presented in Section 3.2.1, with minor modifications. In brief, two-part PDMS was prepared in a 4 oz. poly(propylene) Dart cup (McMaster-Carr, Chicago, IL). Any residual bubbles were removed by degassing for 2 h. To facilitate the removal of PDMS applied to the SU8 master template, prior to pouring the PDMS/heat cure solution onto the master, the SU8 was sprayed with a mold release agent (Mann Ease Release 200) [87], and left to rest for 5 minutes in the fume hood. A second coat of Mann Ease Release 200 was applied, and the master left for an additional 5 minutes. The prepared PDMS solution was then poured onto the surface of the SU8 master template, and permitted to spread by gravity across the wafer. To remove any remaining bubbles within the applied PDMS, the entire wafer was degassed for an additional hour.

To crosslink the PDMS on the SU8-based micropost master template, the PDMS-covered wafer was placed in the oven for 1 h at 120°C. After crosslinking, the wafer was removed from the oven and allowed to cool to room temperature. Excess PDMS was carefully trimmed around the wafer edge using a razor blade, and tweezers were used to gradually and concentrically separate the PDMS negative layer from the SU8 master. During separation of the PDMS from the SU8, droplets of isopropanol were added at the interface between the two layers, and allowed to percolate throughout the microfeatures to aid in separating the PDMS from the master without imparting structural damage to the microfeatures. Additional droplets of isopropanol were added at interface of the PDMS and the SU8 as needed during the entire separation process. Finally, upon removing the PDMS negative mold from the master, the PDMS negative was thoroughly rinsed with isopropanol, and stored in a re-sealable plastic wafer container until future use during micropost fabrication.

3.4.3 Fabrication of Micropost Arrays

To permit the fabrication of TiO_2-loaded PDMS-based micropost arrays, the PDMS-based negative molds (described in the previous section) were used to prepare the micropost arrays. Before applying uncrosslinked TiO_2-loaded PDMS to the negative mold, the PDMS mold was sprayed with the Mann Ease Release 200 mold release agent, as described in Section 3.4.2. This was done to enable the micropost arrays to be effectively separated from the negative PDMS molds.

Following comparable methods as those outlined in Section 3.2.1 for the preparation of TiO_2/PDMS bulk films, 10 % (w/w) and 20 % (w/w) TiO_2/PDMS solutions were prepared. Depending on the specific formulation (10 or 20 % (w/w) TiO_2) and the desired micropost length (100 μm-, 200 μm-, and 300 μm-long), the appropriate TiO_2/PDMS solution and volume was poured over a particular PDMS-based negative mold housed on aluminum foil, and degassed for 1 h. Upon confirming the absence of any macroscopically detectable bubbles in the TiO_2/PDMS solution atop the PDMS mold, the TiO_2/PDMS-loaded mold was placed in the oven for 1 h at 120ºC. Following crosslinking, the loaded mold was removed from the oven and left to cool to room temperature. Using an identical separation technique as that applied to remove the PDMS negative mold from the SU8 master template (as described in Section 3.4.2), the TiO_2/PDMS film complete with micropost array microfeatures was peeled from the PDMS-based negative mold and rinsed thoroughly with isopropanol.

To rectify micropost collapse as a result of air drying with isopropanol, the resulting micropost arrays were dried with supercritical CO_2. This also aided in removing any residual mold release agent. The micropost arrays were inspected by optical microscopy (Zeiss) before and after supercritical drying to confirm non-collapsed micropost geometry. Finally, the micropost arrays were stored in plastic resealable wafer containers until subjection to subsequent characterization.

3.4.4 Micropost Array Fabrication Summary

Overall, TiO_2-loaded PDMS micropost arrays were fabricated using standard soft lithography techniques, with unloaded PDMS micropost arrays made as a control. Initially, a positive micropost array master template was prepared from SU8 photoresist through selective SU8 UV photosensitization and thermal crosslinking. This positive master template was used to make negative PDMS-based molds for the micropost arrays. Following crosslinking of the PDMS negative and its careful removal from the SU8 master template, this negative mold was finally used to allow the fabrication of the TiO_2-loaded PDMS micropost arrays. Figure 3.6 illustrates an overview of the major steps through which the microposts were fabricated.

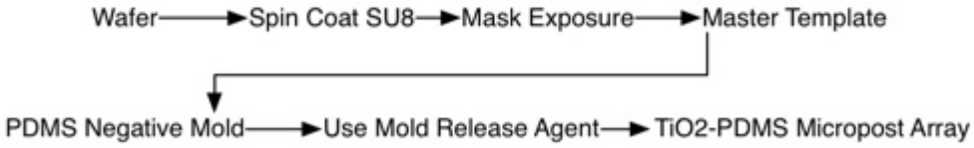

Figure 3.6: Flow chart depicting the major micropost array fabrication steps.

3.5 Micropost Array Characterization

Following fabrication of the TiO_2-loaded PDMS micropost arrays, the different sample groups were qualitatively evaluated to confirm the presence of readily distinguishable and non-collapsed microfeatures, as well to probe the ability to fabricate microposts with precisely-shaped microgeometries. More quantitatively, the observed micropost lengths were recorded via image analysis software, and the micropost effects on surface hydrophobicity were evaluated by performing contact angle measurements. Finally, the micropost mechanical actuatability due to the application of an electric field was assessed, to characterize the potential for liquid droplets to be manipulated by the arrays of TiO_2-loaded PDMS microposts.

3.5.1 Macroscopic and Microscopic Evaluation

Each micropost array sample (as listed in Table 3.1) was macroscopically evaluated by visual inspection and digital photography using a Canon Powershot A640 digital camera (macro setting). Physically, the arrays were assessed for any readily discernable qualitative differences across different micropost formulations, in terms of appearance and mechanical feel.

Optical microscopy equipped with image analysis software was employed to size and qualitatively evaluate individual microfeatures on the SU8 master templates, the PDMS negative molds, and the micropost arrays using a Zeiss optical microscope.

3.5.2 Contact Angle Measurement and Micropost Deflection

The contact angle of a deionized water droplet (4 μL or lower in volume) on each micropost array sample was measured through following identical methods to those outlined in Section 3.2.4. In brief, contact angles of droplets were determined using a VCA goniometer equipped with VCA Optima XE software (AST Products Inc., Billerica, MA). All contact angle measurements were taken in triplicate (n=3).

Following static (0 V) contact angle measurement of the droplets on the micropost arrays, the goniometer was connected to a Gamma High Voltage ES20P-5W/DAM power supply (Figure 3.4), and the contact angle as a function of voltage was measured incrementally (0 kV, 5 kV, 7.5 kV, 10 kV, 12.5 kV) until post deflection was observed, or until dielectric breakdown occurred. Contact angle measurements were once again recorded as the righthand side contact angle (θ_R) and the lefthand side contact angle (θ_L) for each droplet, and the CAH was determined for each investigated droplet. Microscopic video observation was used to capture deflection of individual microposts.

3.5.3 Conductivity Impact on Contact Angle and Contact Angle Hysteresis

Non-conductive fluids should have high CAH in the presence of a high electric field, due to dielectric effects. The contact angle and CAH data collected using DI water droplets, as described in the previous section, provided a foundation to investigate the impact of micropost deflection on CAH. To further probe droplet behavior on the array surfaces, highly conductive water droplets were prepared and deposited on the bulk PDMS and 20 % (w/w) TiO_2-loaded PDMS films, as well as on unloaded PDMS and 20 % (w/w) TiO_2-loaded PDMS 300 µm-long micropost arrays. Due to the high number of ions in conductive water, dielectric effects and therefore the overall effect of the electric field on the droplets geometry could be minimized.

Therefore, deionized water conductivity was modulated via the addition of KCl. The final value chosen for the current study was 100 mS/m, and was verified by a standard conductivity meter. The CAH for each conductive water droplet was determined using methods analogous to those employed to determine CAH for the DI droplets in Section 3.5.2. Coupled with the CAH data obtained for the DI droplets, CAH as a function of water conductivity (in units of mS/m) was evaluated.

3.5.4 Droplet Motion on Micropost Array Surfaces

To gain preliminary insight into achieving droplet motion, DI water droplets (4 µL) were deposited on the micropost arrays, and comparable experimental conditions (24 mm gap spacing, 12.5 kV nominal voltage) were applied to the system resulting in a 520.8 kV/m electric field. Any resulting droplet motion was monitored qualitatively by video observation. The electric field strength was then increased up to 666.7 kV/m (16 kV nominal voltage). Again, any droplet motion achieved was recovered in the form of videos.

Chapter 4
Results and Discussion

4.1 Bulk Material Development and Characterization

4.1.1 Bulk Polymeric Film Preparation and Macroscopic Evaluation

Immediately following fabrication of the pure PDMS-based polymeric films, all produced PDMS films appeared physically colorless and translucent (Figure 4.1), and were readily manipulated by hand and/or by using laboratory forceps.

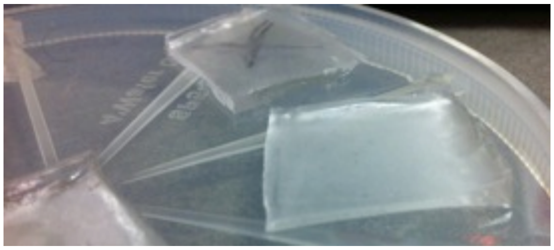

Figure 4.1: Representative bulk unloaded PDMS films.
PDMS to heat cure ratios of 5:1 and 10:1. No visual difference observed.

The 10:1 ratio bulk films were not visually distinguishable from the 5:1 ratio bulk films on a macroscopic level. Although both PDMS formulations were highly flexible during manual qualitative examination, the PDMS films fabricated with a 5:1 ratio were observed to be qualitatively stiffer than the 10:1 ratio PDMS to heat cure samples. For subsequent experiments performed in this work, a 10:1 ratio was applied during the fabrication of all bulk films and micropost arrays to facilitate mold separation during fabrication.

In developing the bulk starting materials for use in micropost array fabrication, significant challenges were overcome to avoid bubble formation during film preparation. Degassing steps were introduced to overcome initial problems caused by air trapped within the samples. Further, vacuum desiccation steps were also introduced to aid in the removal of any air bubbles. The removal of residual bubbles was paramount, as their presence would skew mechanical characteristics of the films, thereby affecting the behavior of droplets deposited on the films. The degassing protocol utilized during bulk polymeric film preparation was found to be effective, as no bubbles were observed in the cured samples, and none were found after performing the curing treatment in the laboratory oven. Overall, the methods by which the bulk films were produced enabled PDMS films to be reproducibly prepared with ease.

Identical methods as those used to fabricate the unloaded PDMS films (as shown in Figure 4.1) were successfully used to prepare PANI-loaded PDMS films (Figure 4.2) without the need for protocol alteration or further optimization of film preparation methods. Macroscopically, the PANI-loaded PDMS films appeared black in color and were entirely opaque to light (Figure 4.2).

Figure 4.2: Representative bulk film of 20 % (w/w) PANI-loaded PDMS. Significant tearing and crumbling of the sample is apparent along the film edges.

In contrast to the mechanically robust unloaded PDMS films previously described, all PANI-loaded PDMS films produced during this work were highly susceptible to structural damage, tearing, and crumbling upon manipulation; both by hand and using forceps. Moreover, the PANI particles were only available in the form of microparticles (as opposed to nanoparticles), and the TiO_2 nanoparticles used in this work were significantly lower in cost as compared to the PANI microparticles. Therefore, no further experimentation was performed with

PANI-loaded PDMS films in this work, and TiO_2-loaded PDMS films were focused on instead as an electrically actuatable composite material.

Prior to fabricating the TiO_2-loaded PDMS films, the mean (Z-average) particle diameters of both the hydrophobic (NKT90 Aeroxide®) and the hydrophilic (P25 Aeroxide®) TiO_2 nanoparticles were measured (while dispersed in uncrosslinked PDMS) using dynamic light scattering (DLS) to be 52.98 ± 8.41 nm and 56.49 ± 9.88 nm, respectively (as shown by the particle size distributions shown in Figure 4.3). The statistically comparable mean particle sizes were an indication that hydrophobic and hydrophilic TiO_2 particles had similar dispersion within uncrosslinked PDMS.

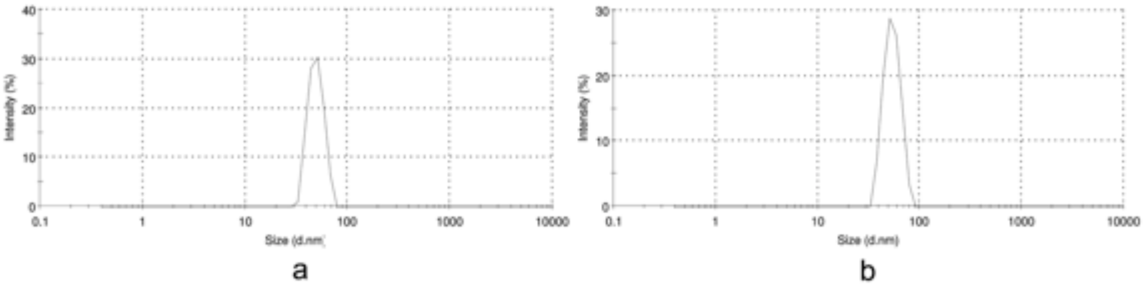

Figure 4.3: Size distributions (by intensity) of TiO_2 nanoparticles.
(a) Hydrophobic (NKT90 Aeroxide®) TiO_2 nanoparticle size distribution, and
(b) hydrophilic (P25 Aeroxide®) TiO_2 nanoparticle size distribution,
as measured using dynamic light scattering.

During TiO_2-loaded PDMS film preparation, like fabrication methods as those used to produce the pure PDMS films successfully yielded 10 and 20 % (w/w) TiO_2-loaded PDMS bulk polymeric films. Figure 4.4 shows a representative TiO_2-loaded PDMS film.

Figure 4.4: Representative TiO_2-loaded PDMS film (20 % (w/w) TiO_2).

Upon macroscopic examination, the resulting TiO_2/PDMS film formulations (10 and 20 % (w/w) TiO_2) appeared opaque and white in color, and could not be visually distinguished from one another.

The TiO_2/PDMS solutions prepared using hydrophobic TiO_2 nanoparticles carrying a net negative charge (NKT90 Aeroxide®) were notably more viscous than the TiO_2/PDMS solutions made with the hydrophilic uncharged TiO_2 nanoparticles (P25 Aeroxide®). However, TiO_2-loaded PDMS solutions prepared using concentrations greater than 20% (w/w) TiO_2 (in the case of both hydrophilic and hydrophobic TiO_2) proved too viscous to permit fabrication of films. Therefore, only 10 and 20 % (w/w) TiO_2-loaded PDMS films were investigated thereafter.

Qualitatively, no difference in mechanical feel was observed across the TiO_2-loaded PDMS film samples, which is consistent with the insignificant differences in the hydrodynamic radii (as measured by DLS) of TiO_2 in liquid PDMS. With respect to the different TiO_2 nanoparticles used to load the PDMS, no macroscopic difference was visually observed in terms of appearance or mechanical feel between TiO_2/PDMS samples prepared using hydrophilic (P25 Aeroxide®) or hydrophobic (NKT90 Aeroxide®) TiO_2 nanoparticles. As compared to the pure PDMS films, the TiO_2-loaded PDMS films were similarly flexible and mechanically robust, and demonstrated significantly enhanced structural integrity as compared to the fragile and easily damaged PANI-loaded PDMS samples.

4.1.2 Particle Distribution in PDMS

Obtaining a uniform distribution of TiO_2 nanoparticles throughout the PDMS proved challenging during initial experiments. To solve this problem, sonication steps were introduced during preparation of the TiO_2-loaded PDMS to yield a more homogeneous base material from which to fabricate the microposts. Ultimately, this could lead to increased physical property uniformity across micropost arrays and reduce the probability of observing non-uniform deflection of microposts in the presence of an electric field.

SEM was used to visualize the TiO_2 nanoparticle distribution throughout the PDMS. Figure 4.5 depicts representative SEM images of 10 and 20 % (w/w) TiO_2-loaded PDMS films, and shows the hydrophobic NKT90 TiO_2 nanoparticle distribution as compared to the hydrophilic P25 TiO_2 nanoparticles (at both 10 and 20 % (w/w) formulations). TiO_2 nanoparticles were identified on the SEM images as individual white- and/or lightly-colored specs, with the smaller diameter specs pointing to a decreased level of TiO_2 nanoparticle agglomeration (enhanced nanoparticle dispersion).

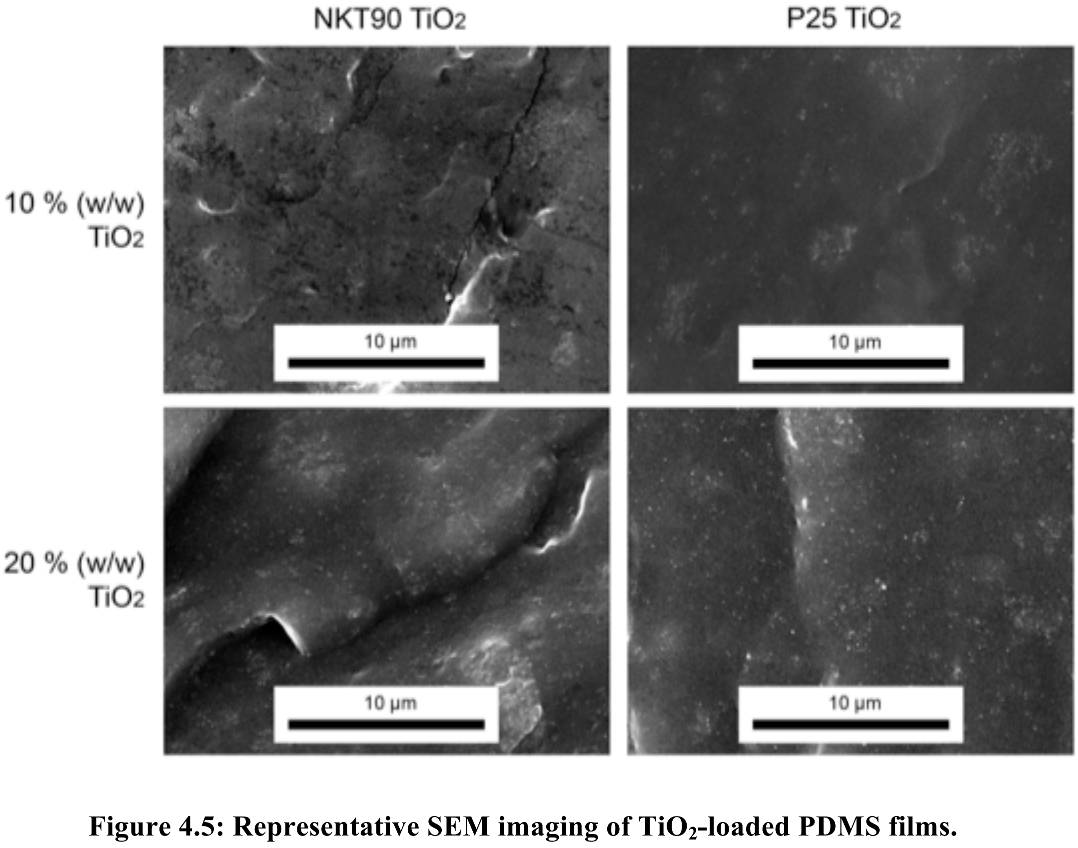

Figure 4.5: Representative SEM imaging of TiO_2-loaded PDMS films.
All scale bars are 10 µm in length.
10 and 20 % (w/w) TiO_2/PDMS with NKT90 TiO_2 nanoparticles (left) and P25 TiO_2 nanoparticles (right).
Magnification 5000 x, Accelerating Voltage 10 kV, Working Distance 10 mm.

As anticipated, a larger density of particles was qualitatively observed throughout the 20 % (w/w) TiO_2-loaded PDMS films (Figure 4.5, bottom row) compared to the 10 % (w/w) TiO_2-loaded PDMS films (Figure 4.5, top row). The TiO_2-loaded PDMS films fabricated using the hydrophobic charged TiO_2 nanoparticles (NKT90 Aeroxide®) demonstrated enhanced particle dispersion throughout the cured PDMS, with reduced agglomeration of particles across samples as compared to TiO_2-loaded PDMS films fabricated using the hydrophilic P25 Aeroxide® TiO_2 nanoparticles. This is an indication that while in dilute quantities, electrostatic forces do not play a significant role in stability (given the similar particle diameters observed by DLS); but while in the higher concentrations, this is no longer the case based on the differences observed for particle dispersion under SEM and qualitative rheological observations. Based on the enhanced viscosity and particle dispersion qualitatively observed for the PDMS films loaded with NKT90 Aeroxide® hydrophobic TiO_2 nanoparticles, NKT90 Aeroxide® TiO_2 was selected for use in subsequent experiments. Unloaded PDMS films were not visualized under SEM given their lack of conductivity.

Overall, during the investigation of various TiO_2 particles when preparing the loaded PDMS mixtures, interesting differences were observed for hydrophobic TiO_2 nanoparticles (NKT90), as compared to hydrophilic TiO_2 nanoparticles (P25). Despite the relatively comparable mean particle size of the hydrophobic (NKT90) and hydrophilic (P25) TiO_2 nanoparticles (52.98 ± 8.41 nm and 56.49 ± 9.88 nm, respectively), as characterized in this study using dynamic light scattering, SEM imaging performed to visually assess the distribution of the TiO_2 nanoparticles throughout the PDMS showed that hydrophobic NKT90 nanoparticles were less agglomerated and slightly better distributed throughout the PDMS, as compared to the P25 hydrophilic TiO_2 nanoparticles. This is logical, given that the NKT90 nanoparticles carry a net negative charge, and would therefore be free flowing throughout the PDMS (which is also hydrophobic). Based on this enhanced distribution of the TiO_2 nanoparticles observed in PDMS, the higher viscosity observed for the hydrophobic TiO_2/PDMS formulation (as compared to the hydrophilic P25 TiO_2/PDMS formulation) is also logical. This higher viscosity is likely the result of the decreased frequency of particle interactions, in the mixture due to the greater dispersion of the TiO_2 nanoparticles throughout the PDMS, giving a more homogenous dispersion.

4.1.3 Young's Modulus Measurement

Figure 4.6 shows a representative bulk TiO_2-PDMS film that was used during sample preparation (from which multiple tensile bars were punched). An individual resulting tensile bar is shown to the right of the bulk film in Figure 4.6.

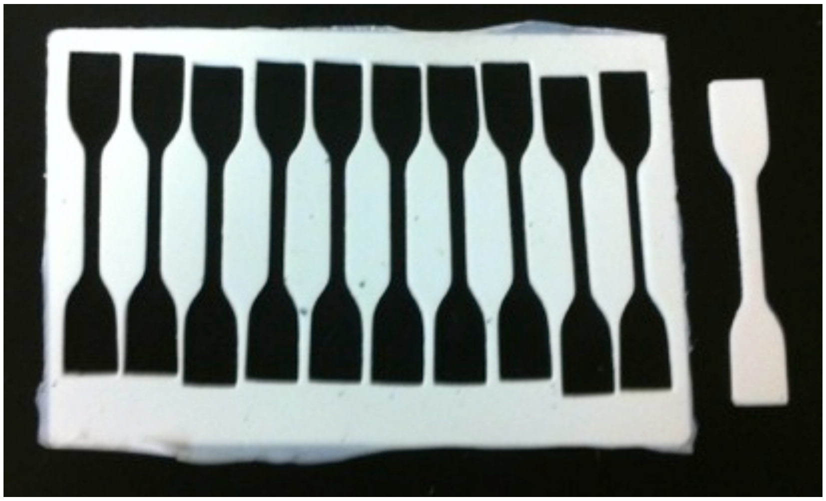

Figure 4.6: Preparation of PDMS tensile bars used for Young's Moduli measurement.

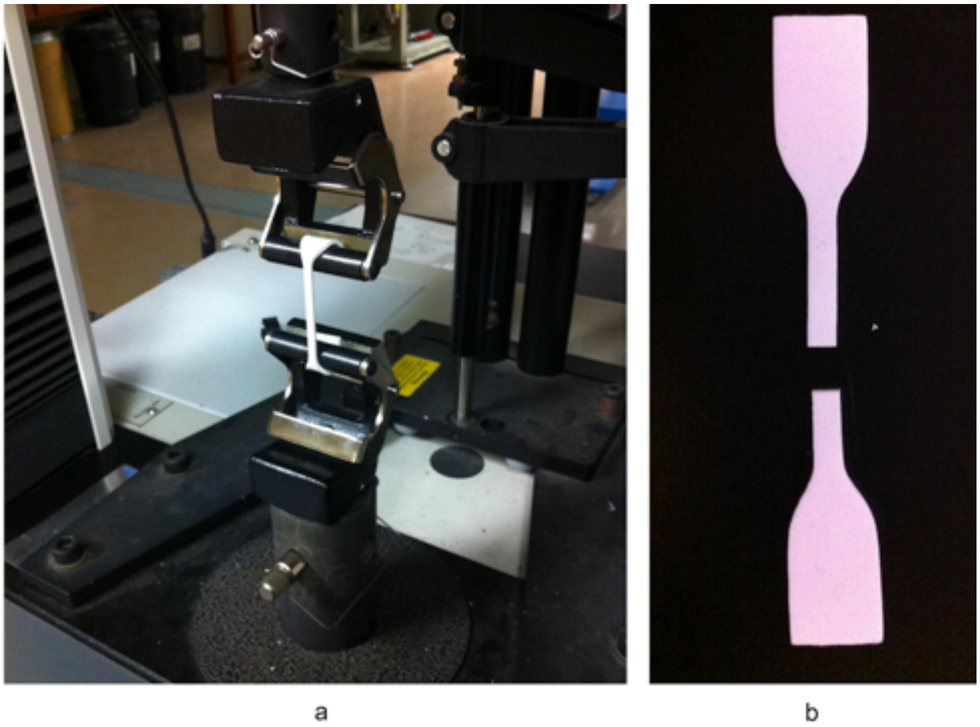

Figure 4.7: (a) Tensile bar testing in progress and (b) a tensile bar post-failure.

Figure 4.7 shows testing of the tensile bars in progress on the Instron machine, as well as a tensile bar post-failure. Table 4.1 lists the mean measured Young's Moduli values, along with standard deviations, measured for PDMS films loaded with 10 % and 20 % (w/w) TiO_2 (NKT90 Aeroxide®), as well as the value for an unloaded (0 % (w/w) TiO_2) PDMS control film.

Table 4.1: Young's Moduli measured for bulk film formulations.
All data are expressed as the mean ± the standard deviation (SD).

Formulation	**Young's Modulus**
Unloaded (0 % (w/w) TiO_2) PDMS	4.22 ± 0.51 MPa (*n*=7)
10 % (w/w) TiO_2-loaded PDMS	2.27 ± 0.18 MPa (*n*=10)
20 % (w/w) TiO_2-loaded PDMS	1.39 ± 0.20 MPa (*n*=10)

To ensure Young's Moduli measurements were statistically meaningful, at least seven (*n*=7) tensile bars were tested for unloaded PDMS, with the polymeric composite Young's Moduli measurements averaged from ten (*n*=10) tensile bars from each formulation (10 and 20 % (w/w) TiO_2). The values for the standard deviations listed in Table 4.1 point to the statistically low variability of the Young's Moduli values measured, and the reliability of the mean Young's Moduli values calculated across multiple samples.

As anticipated, an inverse relationship between TiO_2 % (w/w) and the observed Young's Modulus was apparent, with a greater TiO_2 % (w/w) corresponding to a lower mean Young's Modulus value. The mean Young's Moduli values determined for the 10 and 20 % (w/w) TiO_2-loaded PDMS tensile bars (2.27 ± 0.18 MPa and 1.39 ± 0.20 MPa, respectively) were significantly lower than the mean Young's Modulus value determined for the unloaded PDMS tensile bars (4.22 ± 0.51 MPa). Through loading the PDMS with 10 % (w/w) TiO_2, the mean Young's Modulus value was reduced by almost twofold, while the addition of 20 % (w/w) TiO_2 resulted in an approximately threefold decrease in the mean Young's Modulus value.

Interestingly, as compared to the mean Young's Modulus value for unloaded PDMS found in the literature (1.7 ± 0.3 MPa [47]), the unloaded PDMS mean Young's Modulus value observed during this work (4.22 ± 0.51 MPa) was ~ threefold higher in value. This higher value may be attributed to the doubled quantity of crosslinking agent used in the current work during PDMS film preparation, toward the aim of yielding a more robust starting material for use in fabricating the micropost arrays. More specifically, through utilizing PDMS with a higher Young's Modulus, undesirable mold release challenges were reduced during micropost array fabrication, and the microposts themselves were more likely to retain their structural/geometrical integrity over the course of the many required microfabrication steps.

Young's Moduli measurements taken for different PDMS formulations were in keeping with the expectation that, upon increasing the level of impurities in the PDMS (in the form of TiO_2 nanoparticles), the elasticity of the material increased and the corresponding values for the Young's Moduli decreased. Qualitatively, the difference in elasticity was noticeable during tensile bar testing, with the unloaded PDMS tensile bars snapping in two almost immediately, whereas those tensile bars loaded with TiO_2 visibly stretched over a period of time before failing.

4.1.4 Contact Angle Measurement

To provide contact angle measurements for the bulk films (free of microposts), the contact angles of DI water droplets deposited on bulk unloaded PDMS films, 10 % (w/w) TiO_2-PDMS films, and 20 % (w/w) TiO_2-PDMS films were determined using image analysis, as demonstrated by the representative screen shots shown in Figure 4.8. The top row of Figure 4.8 has no electric field applied (electric field strength was 0 kV/m). Given the experimental conditions of a 24 mm electrode spacing and a nominal voltage applied of 12.5 kV, the electric field strength applied in the bottom row of Figure 4.8 was 520.8 kV/m.

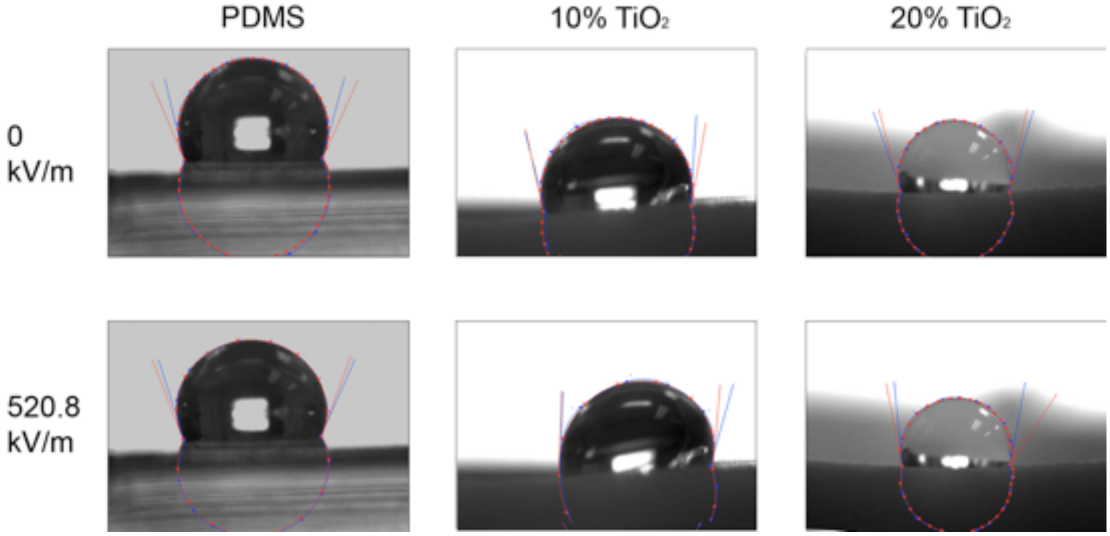

Figure 4.8: Contact angles, as measured using image analysis techniques.
Deionized (DI) water droplet volume = 4 μL.

The screenshot from Figure 4.8 depicting a droplet on 10 % (w/w) TiO_2-loaded PDMS subjected to a 520.8 kV/m electric field (12.5 kV nominal voltage) shows CAH, in which the lefthand side contact angle (θ_L) is visibly different than the righthand side contact angle (θ_R). In the cases of all bulk film formulations, the contact angle for droplets was readily measured using image analysis. These determined mean contact angle values (θ_R and θ_L) and their corresponding mean CAH values are summarized in Table 4.2 as a function of electric field strength (*n*=3 for each film formulation).

Table 4.2: DI water contact angle data for bulk film surfaces.

θ_L = lefthand side contact angle, θ_R = righthand side contact angle, CAH = contact angle hysteresis. Data for each film formulation are listed as the mean ± standard deviation (SD), with electric field strengths of 0 and 520.8 kV/m.

	Electric Field = 0 kV/m			Electric Field = 520.8 kV/m		
Film Surface	θ_L	θ_R	CAH	θ_L	θ_R	CAH
PDMS	113 ± 2°	114 ± 2°	1 ± 2°	110 ± 1°	101 ± 9°	-9 ± 9°
10% TiO_2	106 ± 3°	103 ±1°	-2 ± 4°	92 ± 5°	111 ± 11°	19 ± 6°
20% TiO_2	107 ± 2°	107 ± 14°	0 ± 12°	100 ± 1°	124 ± 8°	24 ± 9°

With the exception of one mean contact angle value measured on a 20 % (w/w) TiO_2 sample, all contact angle measurements remained below 120° (which is often used as the threshold to define super-hydrophobic surfaces). Therefore, as expected, it is apparent that the bulk films prepared were not super-hydrophobic.

To more easily visualize the CAH data in Table 4.2 the following graph clearly depicts the general trends in CAH observed for the different bulk film formulations (Figure 4.9).

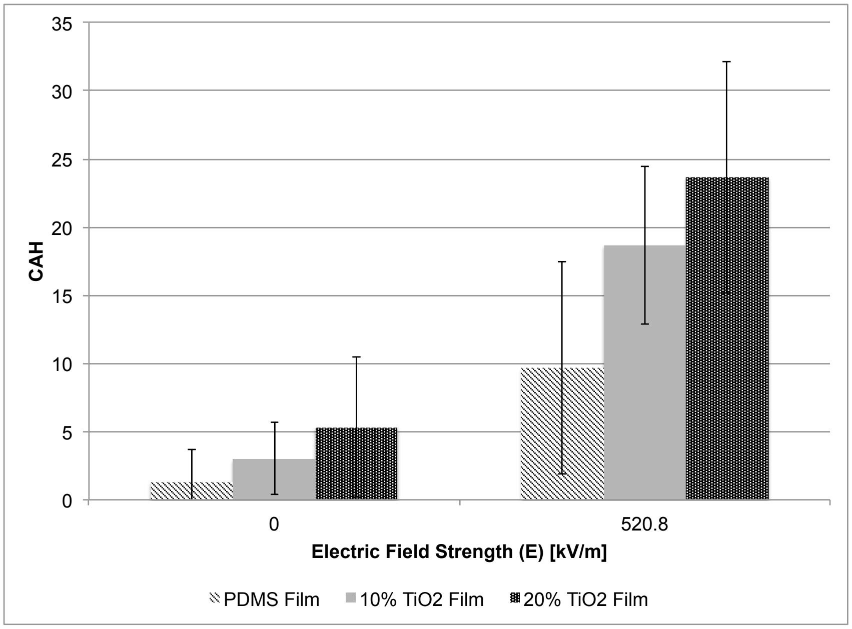

Figure 4.9: Bulk film contact angle hysteresis (CAH) versus electric field strength (E). All data are expressed as the absolute value of the mean CAH ± SD (*n*=3).

Based on the mean absolute CAH values obtained, it was apparent that the greatest mean CAH values were observed for the PDMS loaded with 20 % (w/w) TiO_2, with the 10 % (w/w) TiO_2 samples next highest, and the unloaded PDMS demonstrating the lowest mean CAH values. No significant CAH was observed for the unloaded PDMS samples. In the presence of an electric field, large increases in the mean CAH values were observed for the loaded samples.

During this work, each contact angle measurement was performed in triplicate (*n*=3) to enable the calculation of the mean and simple statistical analyses yielding standard deviation values. Despite any variability observed during this work across measured values, the trend in mean angle value and CAH is still evident.

Reasons for the observed standard deviations of measured contact angles (and in subsequent CAH values) could vary widely. It is possible that a less clean surface contributed to the higher values of CAH observed. This is not wholly unexpected; the TiO_2 used (NKT90) carries net charge, and is thus much more likely to capture positively charged particles from the air. While all samples were rinsed with ethanol before testing, the experiments were not conducted in a high classification “Clean Room” area. In the case of an applied electric field, there was an observed bending of the sample which necessitated being extremely careful during measurements to obtain a locally flat area for contact angle analysis. Slight variations in film profile under the droplet may also account for error. However, the impact of applying an electric field on achieving CAH is quite clear (Figure 4.9) for the TiO_2-loaded PDMS samples.

4.1.5 Bulk Film Deflection

As anticipated, the unloaded PDMS cylindrical samples prepared as controls did not deflect in the presence of the electric field. However, both 10 and 20 % (w/w) TiO_2-loaded PDMS cylinders demonstrated significant bulk material deflection under the investigated conditions (24 mm gap spacing, 7.2 kV nominal voltage, 300 kV/m electric field strength). Figure 4.10 shows the preparation of a representative cylindrical sample prepared using a glass capillary tube (Figure 4.10a) and the resulting sample before being trimmed in length (Figure 4.10b).

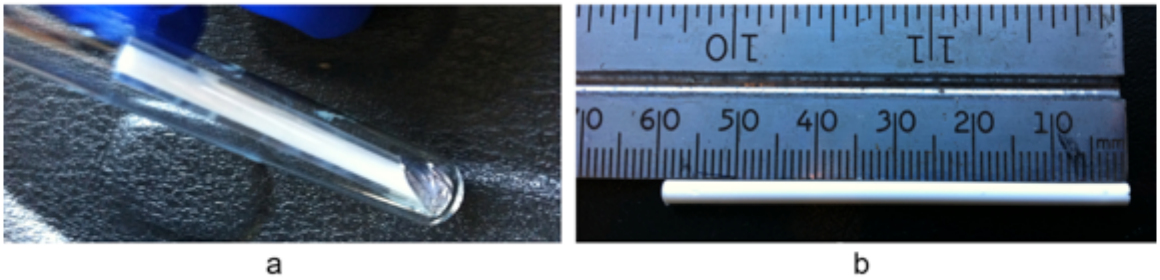

Figure 4.10: Cylindrical sample preparation for bulk material deflection testing. (a) Sample preparation in capillary tube, and (b) resulting cylindrical sample (free of debris).

Figure 4.11 illustrates the representative deflection of the 10 % (w/w) TiO_2-loaded PDMS cylinders. Figure 4.12 illustrates the representative deflection of the 20 % (w/w) TiO_2-loaded PDMS cylinders.

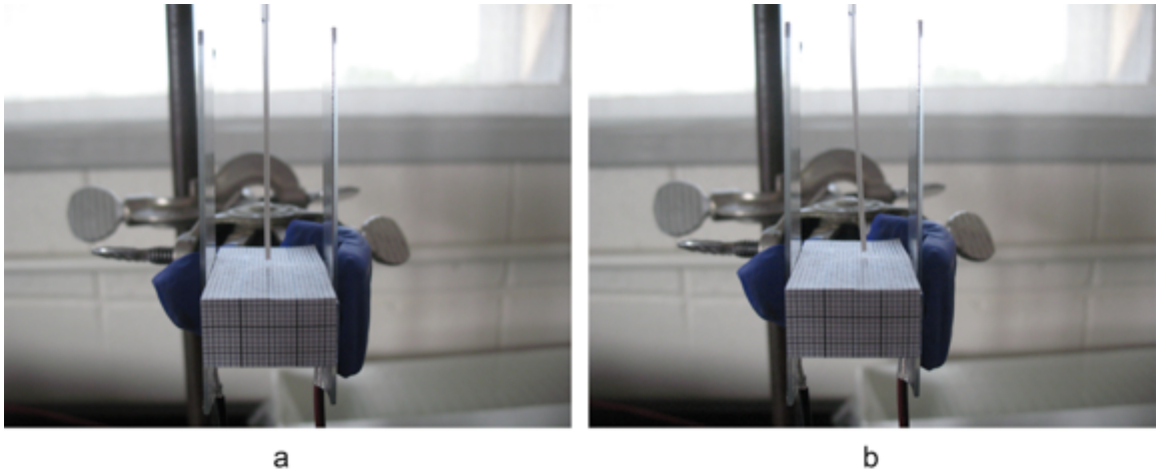

Figure 4.11: Representative bulk material deflection of 10 % (w/w) TiO_2-loaded PDMS.
24 mm gap spacing. Negative electrode on the righthand side.
(a) 0 kV nominal voltage, 0 kV/m electric field strength (no deflection observed).
(b) 7.2 kV nominal voltage, 300 kV/m electric field strength (deflection observed).

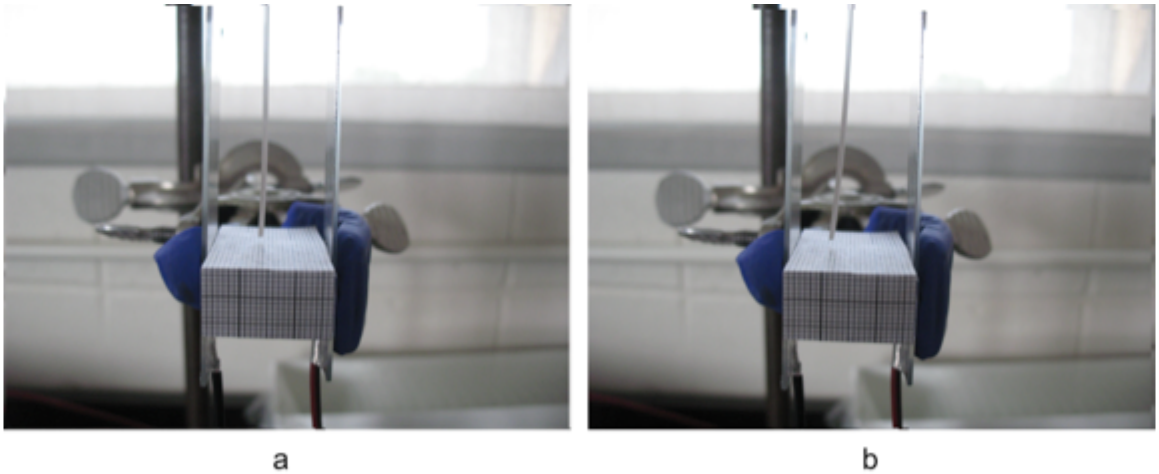

Figure 4.12: Representative bulk material deflection of 20 % (w/w) TiO_2-loaded PDMS.
24 mm electrode spacing. Negative electrode on the righthand side.
(a) 0 kV nominal voltage, 0 kV/m electric field strength (no deflection observed).
(b) 7.2 kV nominal voltage, 300 kV/m electric field strength (deflection observed).

Using the grid as a visual guide, it is evident in Figure 4.11 that in the presence of the 300 kV/m electric field, the 10 % (w/w) TiO_2-loaded PDMS cylinder deflected laterally ~ 2.5 mm, whereas the 20 % (w/w) TiO_2-loaded PDMS cylinder shown in Figure 4.12 deflected laterally ~ 5 mm. Overall, an approximate twofold increase in deflection was observed as a result of increasing the TiO_2 weight percentage from 10 to 20 % (w/w). This confirmation of bulk material deflection validated not only the apparatus, but also the use of 10 and 20 % (w/w) TiO_2-loaded PDMS as starting materials for the fabrication of the micropost arrays detailed in the sections that follow.

The reversal in direction of the sample movement (deflection) is most likely attributed to the increased polarizability of the 20 % (w/w) TiO_2 sample due to higher loading of negatively charged particles in this sample as compared to the 10 % (w/w) TiO_2 sample, as both materials have similar Young's Modulus values. The specific mechanism by which deflection occurs remains to be determined, as discussions surrounding this topic in the literature remain inconclusive [10].

4.2 Micropost Design

4.2.1 Mathematical Model

Microsoft Excel was successfully employed to solve an iterative mathematical model that, when given input values for the desired micropost shape and diameter, predicted the desired micropost length (height) and micropost spacing (center to center) corresponding to a micropost array yielding a stable, super-hydrophobic surface. Figure 4.13 shows a representative screenshot of this model. In this particular example, the model was used to iteratively predict that for 15 μm-diameter cylindrical microposts, an array with microposts ~ 300 μm in length and spaced 50 μm apart from one another, would yield a stable, super-hydrophobic surface.

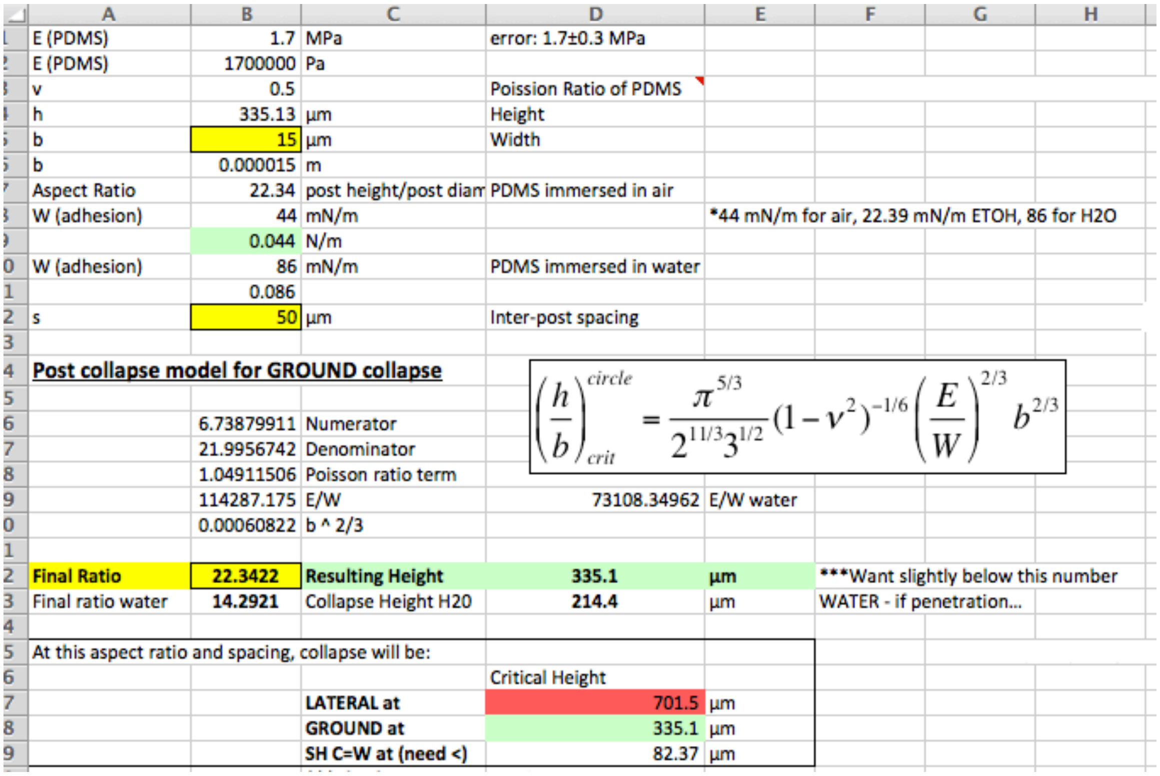

A	B	C	D	E	F	G	H
E (PDMS)	1.7	MPa	error: 1.7±0.3 MPa				
E (PDMS)	1700000	Pa					
v	0.5		Poission Ratio of PDMS				
h	335.13	µm	Height				
b	15	µm	Width				
b	0.000015	m					
Aspect Ratio	22.34	post height/post diam	PDMS immersed in air				
W (adhesion)	44	mN/m		*44 mN/m for air, 22.39 mN/m ETOH, 86 for H2O			
	0.044	N/m					
W (adhesion)	86	mN/m	PDMS immersed in water				
	0.086						
s	50	µm	Inter-post spacing				
Post collapse model for GROUND collapse							
	6.73879911	Numerator					
	21.9956742	Denominator					
	1.04911506	Poisson ratio term					
	114287.175	E/W	73108.34962	E/W water			
	0.00060822	b ^ 2/3					
Final Ratio	**22.3422**	**Resulting Height**	**335.1**	**µm**	***Want slightly below this number		
Final ratio water	**14.2921**	Collapse Height H20	**214.4**	µm	WATER - if penetration...		
At this aspect ratio and spacing, collapse will be:							
			Critical Height				
		LATERAL at	701.5	µm			
		GROUND at	335.1	µm			
		SH C=W at (need <)	82.37	µm			

$$\left(\frac{h}{b}\right)_{crit}^{circle} = \frac{\pi^{5/3}}{2^{11/3}3^{1/2}}(1-\nu^2)^{-1/6}\left(\frac{E}{W}\right)^{2/3} b^{2/3}$$

Figure 4.13: Representative screenshot of the micropost Excel model.
Through iteratively inputting geometrical specifications, predictions were made using this model for micropost geometries that would yield arrays forming stable, super-hydrophobic surfaces. This example links round, 15 µm diameter microposts to a 50 µm spacing and ~300 µm height.

The successful measurement of the mean Young's Moduli for the bulk PDMS and the TiO_2-loaded PDMS formulations proved instrumental in applying the mathematical model developed in this work to effectively predict micropost geometries to yield stable yet super-hydrophobic surfaces comprised of micropost arrays. Through integrating the Young's Moduli measured with the model, the impact of the micropost elasticity as a function of TiO_2-loading could be taken into account while iteratively designing the different micropost geometries.

The model was also successfully used to generate a corresponding graphical representation of the hydrophobicity of a material as a function of micropost spacing within an array for different micropost shapes. A diagram depicting the meaning of relevant boundaries and regions for this graph is shown in Figure 4.14.

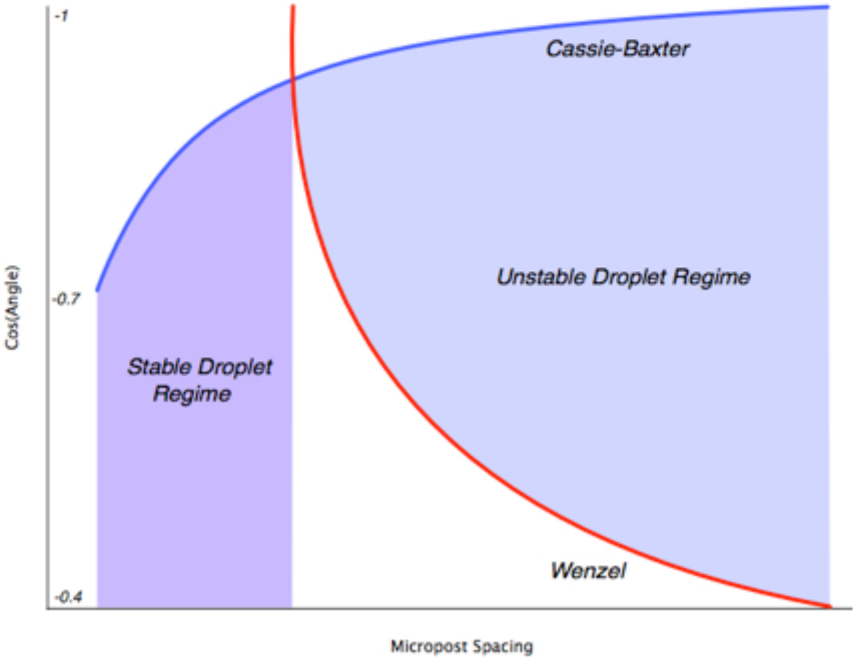

Figure 4.14: The stable, super-hydrophobic micropost design regions.

Figure 4.15 depicts an actual graphical output from the predictive model.

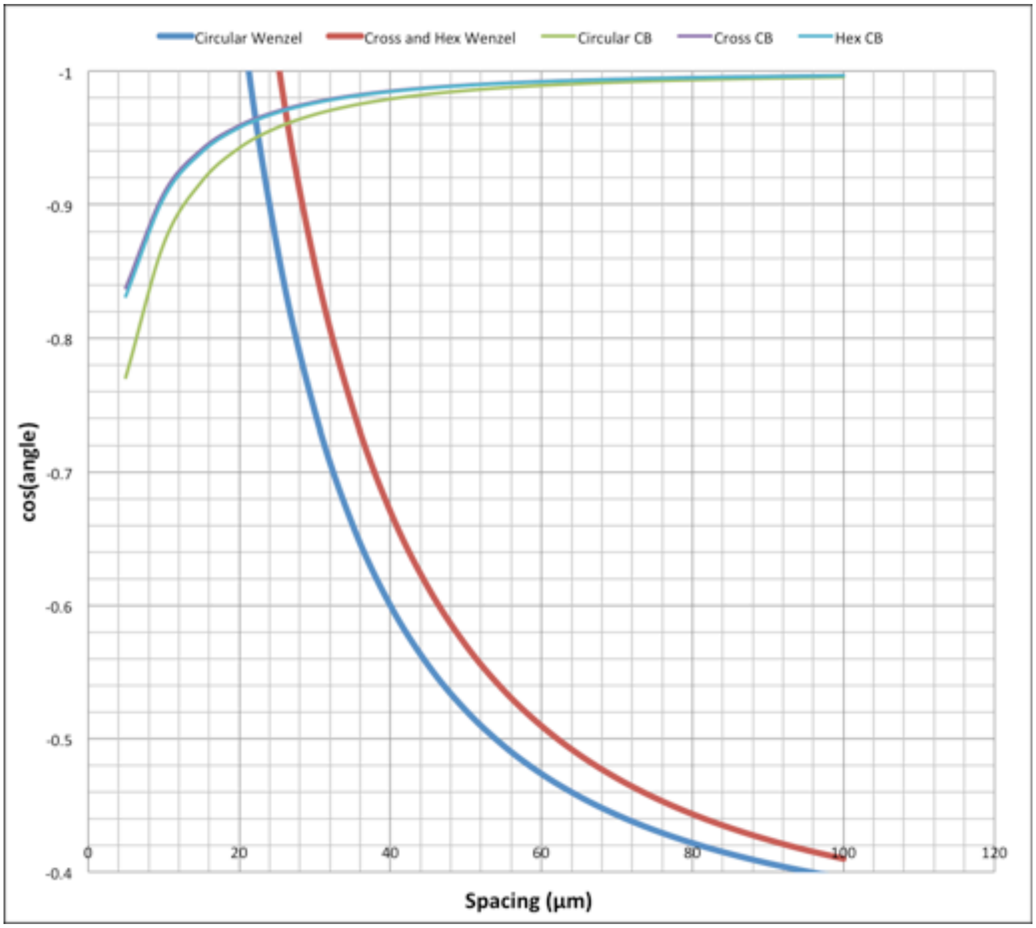

Figure 4.15: Representative graphical predicted from micropost model.
This figure shows a representative graphical prediction from the model illustrating contact angle as a function of micropost spacing. CB = Cassie-Baxter. Micropost spacing within the region approaching cos(angle) = -1 will yield stable, super-hydrophobic surfaces without leading to droplet collapse. Predicted values take into account the film formulation (unloaded PDMS versus a customized % of TiO_2).

Through comparing the labeled Figure 4.14 to the predicted representative graph shown in Figure 4.15, the micropost geometries that could, upon fabrication, yield stable, super-hydrophobic surfaces could be readily identified.

As the value for cos(θ) approaches -1, the value of the contact angle approaches 180°. A droplet of water deposited on a perfectly hydrophobic surface would theoretically display a contact angle of 180°. Therefore, to achieve a super-hydrophobic surface through the use of micropost arrays, it was desirable that the micropost shape and spacing yield a surface that could yield a high contact angle but without resulting in droplet collapse between the microposts, which would render the surface as no longer super-hydrophobic.

Use of the design algorithm to predict ideal micropost array geometries as a function of micropost diameter, spacing (center to center), length (height), shape, and material, provided a robust methodology for designing and developing micropost arrays. This methodology can be adapted to specific liquids being handled, and the material of fabrication, while maintaining predictions over stable, super-hydrophobic surfaces that can undergo micropost deflection without experiencing undesirable micropost collapse.

With respect to forces acting on the microposts, the following equation was used to predict the magnitude of the force required to deflect a micropost:

$$F = \left(\frac{3EI}{L^3}\right)\delta \qquad \text{Equation 22}$$

where E is the Young's Modulus, I is the moment of inertia for a cylinder, L is the characteristic length, δ is the resulting deflection, and F is the calculated force. Based on the micropost diameter of 15 μm, and lengths ranging from 100 to 300 μm examined in this work, the force on the composite microposts was between approximately 15 and 45 nN in magnitude. This range corroborates findings in the literature, which report forces in the range of 1-100 nN [7, 75]. However, as previously discussed, the causative mechanism behind micropost bending remains to be determined specifically [10]. However, either electrostriction, the Maxwell stress effect, or both, are most likely the causative agent(s) in this system [88].

Overall, this model was successfully developed and used to iteratively predict micropost array geometries for different micropost shapes that would yield stable, super-hydrophobic surfaces, once fabricated. The outputs from this model were in turn used as micropost geometry specifications (such as micropost diameter, spacing, and height to avoid ground collapse, as can be seen in Figure 4.13) to design and make photomasks for use in micropost array fabrication.

4.2.2 Micropost Array Photomasks Design and Fabrication

Figure 4.16 shows the completed CAD design for the micropost array photomask in the form of representative screenshots taken from the software program L-Edit Pro.

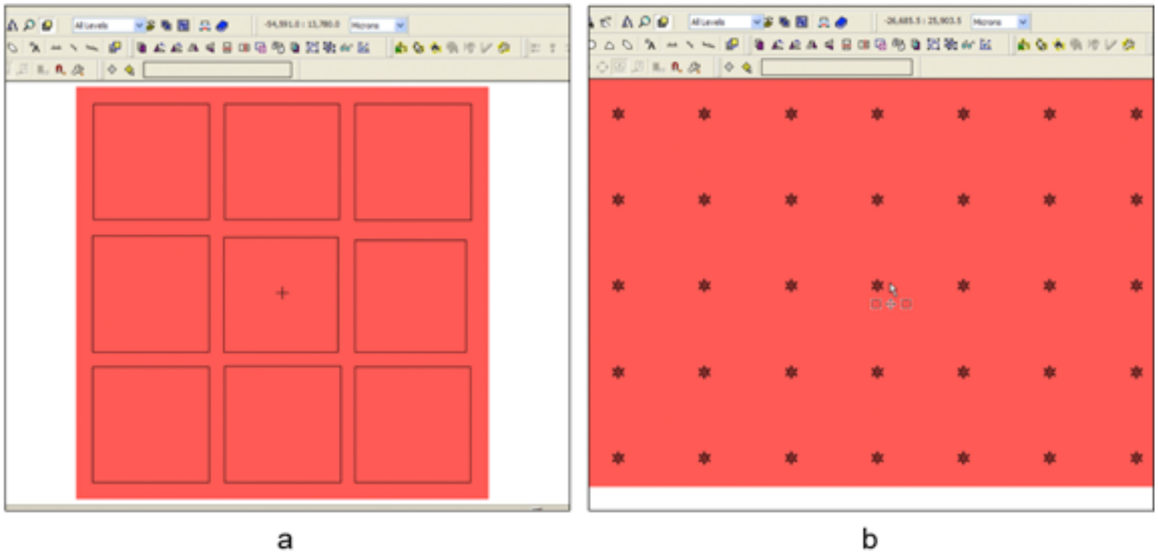

Figure 4.16: Representative photomask design images, as drafted in L-Edit software.
(a) Nine-array overall photomask design, and
(b) a higher magnification screenshot highlighting a single micropost array (microfeatures visible).

Once this CAD design was completed, it was submitted to the fabrication center in Edmonton, AB, where a physical photomask was successfully made for use in this work. Figure 4.17 includes representative optical microscopy images taken at varying original magnifications of the custom-designed photomask. Varying micropost spacings, shapes, and diameters were effectively included in the physical photomask (Figure 4.17).

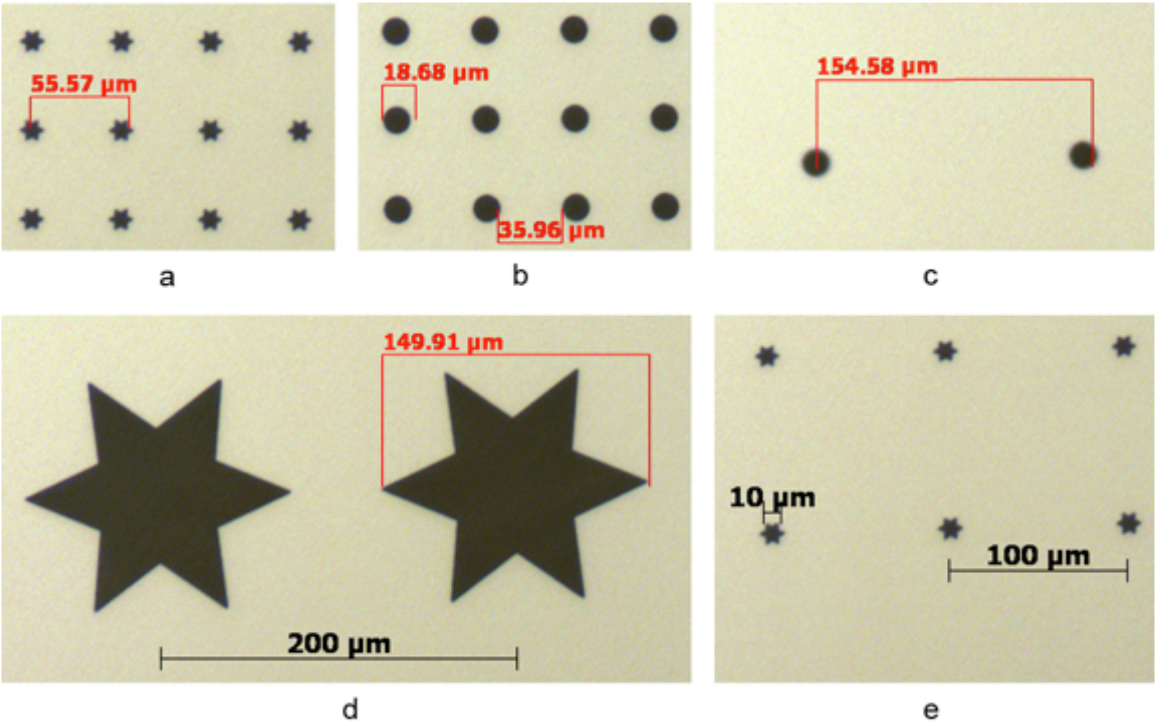

Figure 4.17: Representative optical microscopy images of the physical photomask. Star-shaped (a,d,e) and round-shaped (b,c) microfeatures from various regions of the photomask.

Through comparing the designed micropost spacing values (for example, 10 µm) to the microfeature spacings observed on the photomask using optical microscopy and approximated by image analyses, the accuracy with which the photomask was manufactured was verified to be adequate to proceed with its use in preparing the master templates.

4.3 Micropost Array Fabrication

4.3.1 Master Template Preparation

Master templates for the preparation of the PDMS negatives were successfully prepared from SU8 via traditional spin-coating and photomask UV exposure techniques. Challenges in obtaining adequately thick SU8 layers so as to yield master templates for the 200 μm and 300 μm micropost arrays were overcome through adapting general methods across literature and spin-coating many thin layers of SU8 successively onto the silicon wafers (Figure 4.18).

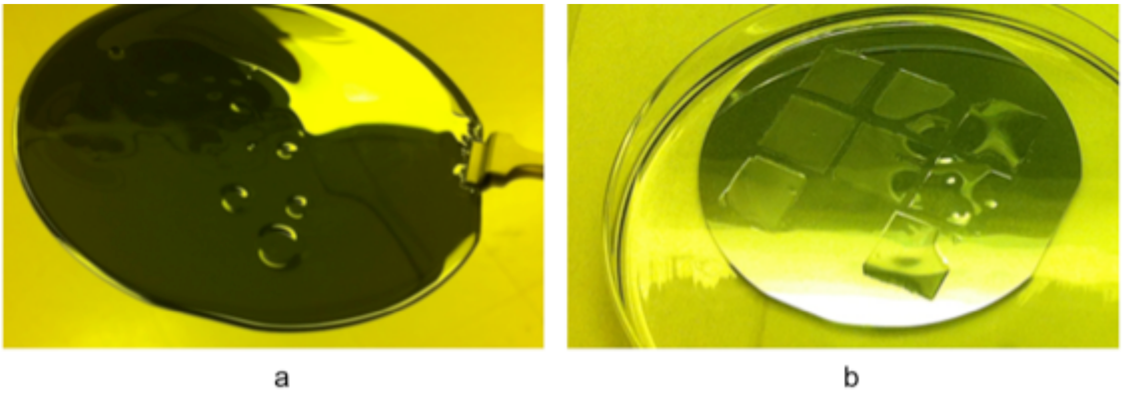

Figure 4.18: Master template preparation.
(a) Silicon wafer (4-inch) mid-spin coating with SU8, and
(b) the resulting “master template” with the square arrays of SU8 microposts evident.

Figure 4.19 shows representative optical microscopy images of the SU8 master templates generated from the photomask, for use in preparing the PDMS-based negative molds discussed in Section 4.3.2.

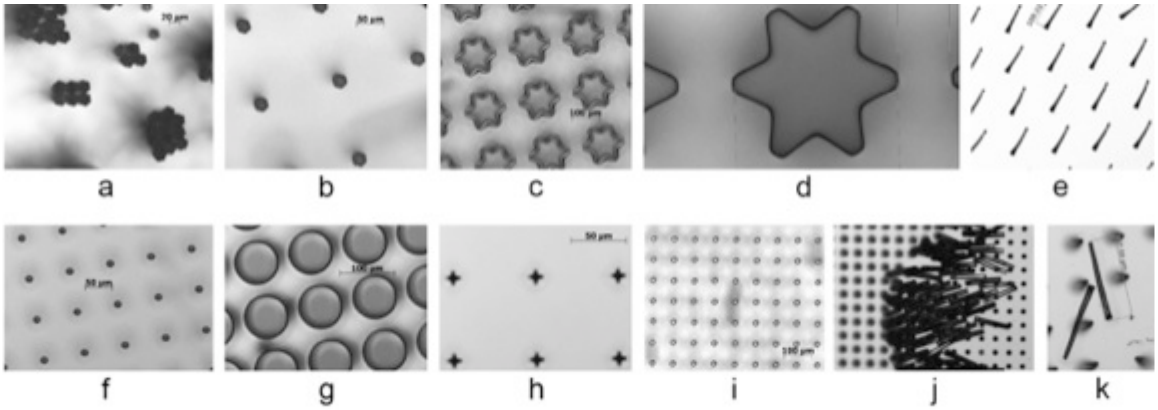

Figure 4.19: Representative optical microscopy images of SU8 master templates.
(a) Mid-removal of excess SU8, (b) resulting SU8 template with individual microposts, (c) star-shaped array of SU8 microposts, (d) examination of SU8 template geometric integrity, (e) unoptimized round SU8 microposts showing collapse (f) optimized round SU8 microposts from above, (g) closer inspection of a round SU8 micropost array, (h) cross-shaped template achieved, (i) diamond-shaped template achieved, (j) non-collapsed vs. collapsed SU8 microposts, and (k) examination of isolated 300 μm long SU8 microposts (scale bar along micropost = 298 μm).

As shown in Figure 4.19, the fabrication methods developed in this work effectively removed all excess SU8 from the surface of the wafer, leaving behind only the arrays of SU8 microposts (Figure 4.19a, b). Varying SU8 template geometries were effectively produced from the photomask. More specifically, different micropost shapes including rounded, star-shaped, hexagram-shaped, cross-shaped, and diamond-shaped SU8 microposts of differing diameters and spacings were successfully made as master templates (Figure 4.19b, c, d, g, h, i). Furthermore, the SU8 template arrays were largely free of defects and uniform in appearance, without the loss of any individual microposts from the arrays during fabrication steps.

Figure 4.19e and Figure 4.19j provides visual contrast between the appearance of the upright microposts compared to collapsed microposts. Spin-coating protocols employed to coat the silicon wafers with specific thicknesses of SU8 were validated based on micropost length characterization performed via image analyses. For example, the SU8 microposts from the master template spun-coat with an intended thickness of 300 µm were measured using image analyses to be ~300 µm in length (Figure 4.19k, micropost scale bar = 298 µm in length).

Figure 4.20 shows a side profile of 15 µm diameter, star-shaped, 300 µm design length SU8 microposts on a silicon wafer, depicting the high quality of the final master templates.

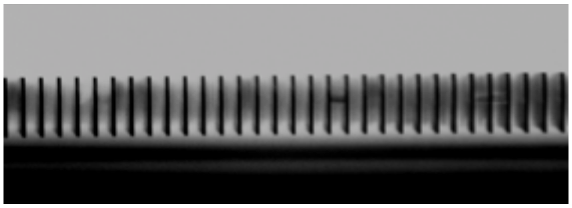

Figure 4.20: Side profile of SU8-based 300 µm long micropost master template.

Testing the SU8 microposts for hydrophobicity by depositing droplets on the surface of the SU8 master templates demonstrated the ability for the SU8 microposts to provide a hydrophobic surface for DI water, as shown by the highly rounded droplet morphology shown in Figure 4.21. Further, the contact angle was measured to be 139°, with negligible CAH observed. In this case, a droplet volume of 7 µL was used, as droplets of volumes below 7 µL were too difficult to release by gravity onto the array surface due to the low wettability of the SU8 microposts.

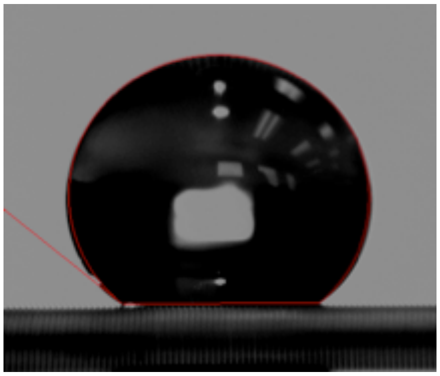

Figure 4.21: SU8 master templates provide a hydrophobic surface.

As the 100 µm-, 200 µm-, and 300 µm-thick master templates fabricated from SU8 were found to be structurally sound and largely defect-free, these "master templates" were retained and used to make the PDMS-based negative molds.

4.3.2 Fabrication of PDMS-Based Negative Molds

The PDMS-based negative molds produced during this intermediate micropost array fabrication step were comparably translucent and pliable to the unloaded PDMS films (Figure 4.1) produced during the initial bulk material characterization phase of this project. The "holes" created in the PDMS negative molds by the SU8 master templates were clear of debris, and there were no discernable signs of SU8 micropost breakage during removal of the PDMS negative molds from the master templates (Figure 4.22a,b).

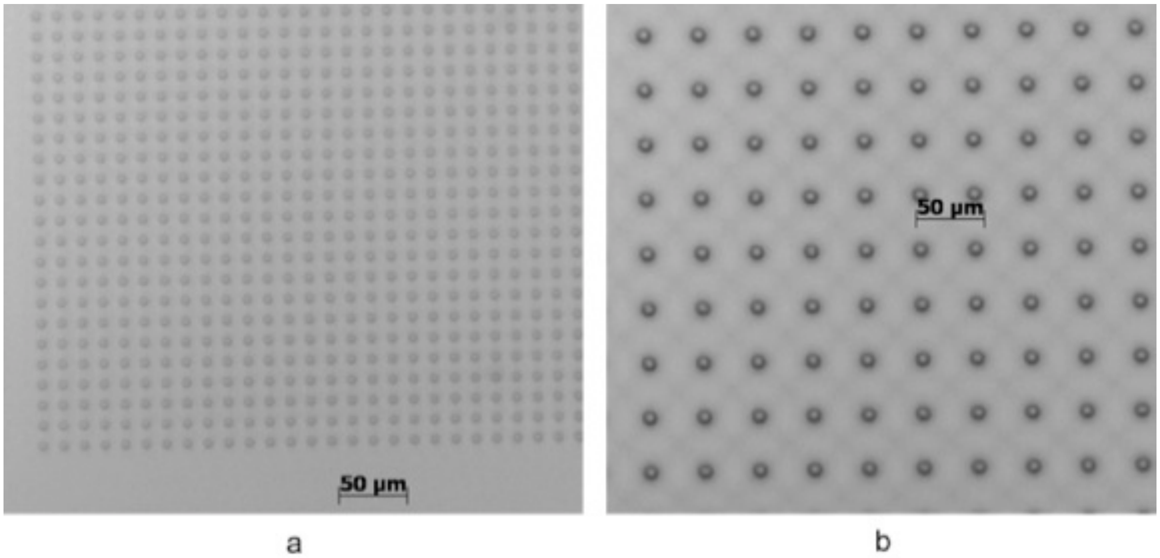

Figure 4.22: PDMS-based negative molds made from SU8-based master templates.
Scale bars are 50 µm in length.
(a) Overall mold appearance, and (b) individual holes free of debris.

4.3.3 Micropost Array Preparation

Coupled with the use of the mold release agent and/or the application of isopropanol, the unloaded and TiO_2-loaded PDMS micropost arrays made using the PDMS-based negative templates were readily removed without significantly shearing and/or damaging the microposts.

Originally, the PDMS molds cast on the SU8 master template were made with the standard (10 % (w/w) amount of crosslinker. However, to ease separation, this was increased to 20 % (w/w). This greatly aided in the release of the PDMS from the SU8 master template. The use of a corona generator was investigated to prepare the PDMS mold for silanization, to prevent bonding of the PDMS-TiO_2 composite to the PDMS negative. This proved to be technically unfeasible due to the high aspect ratio of the micropost structures involved. Instead, the use of the off-the-shelf solution of Mann Ease-Release provided a simpler, cheaper, and more robust method. This greatly reduced the time needed and increased the success rate. With the use of the supercritical drying to restore the micropost features, this proved a very successful way to create high aspect ratio structures with PDMS while using minimum resources.

Overall, the micropost arrays were successfully fabricated using the methods described in Chapter 3 of this thesis. The resulting micropost arrays are characterized in Section 4.4.

4.4 Micropost Array Characterization

4.4.1 Macroscopic Evaluation

Upon inspecting the micropost array samples post-fabrication with the naked eye, a distinctly velvet-like surface was readily identified on the locations of the surface that corresponded to the locations of the micropost arrays. Although specific micropost shapes (such as rounded versus star-shaped) could not be discerned without the use of a microscope, the micropost arrays could be readily identified without the need for a microscope. Figure 4.23

includes representative macroscopic images taken with a digital camera depicting a PDMS micropost array (Figure 4.23a) and a TiO_2-loaded micropost array (Figure 4.23b).

Figure 4.23: Macroscopic images of representative micropost arrays.
(a) PDMS micropost array fabricated as a control, and (b) TiO_2-loaded PDMS micropost array.

Tactilely, the micropost arrays were significantly softer to the touch as compared to the polymeric films produced during the bulk material characterization phase of this project.

4.4.2 Microscopic Evaluation

With the aid of optical microscopy, the geometry of individual microposts produced in this work was more readily observed. Specifically, the micropost length, spacing, diameter, and shape of the microposts, in addition to whether or not the microposts demonstrated any collapse, could be visualized. Overall, the images obtained through optical microscopy confirmed the reproducibility and efficacy of the methods developed during this work to fabricate micropost arrays of various geometries from TiO_2-loaded PDMS. Figure 4.24 includes a low-level magnification representative side profile of the resulting microposts.

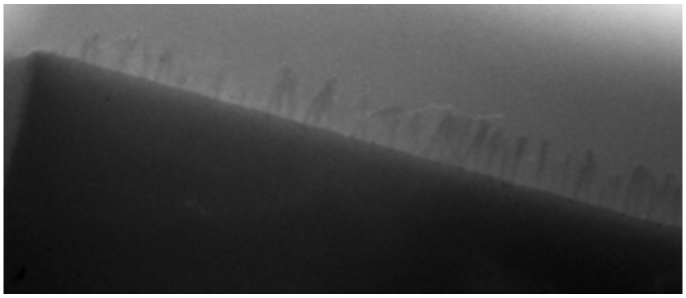

Figure 4.24: Representative side profile of TiO_2/PDMS microposts (300 µm design length).

Figure 4.25 includes selected optical microscopy images depicting a range of the different unloaded PDMS micropost arrays produced over the course of this work.

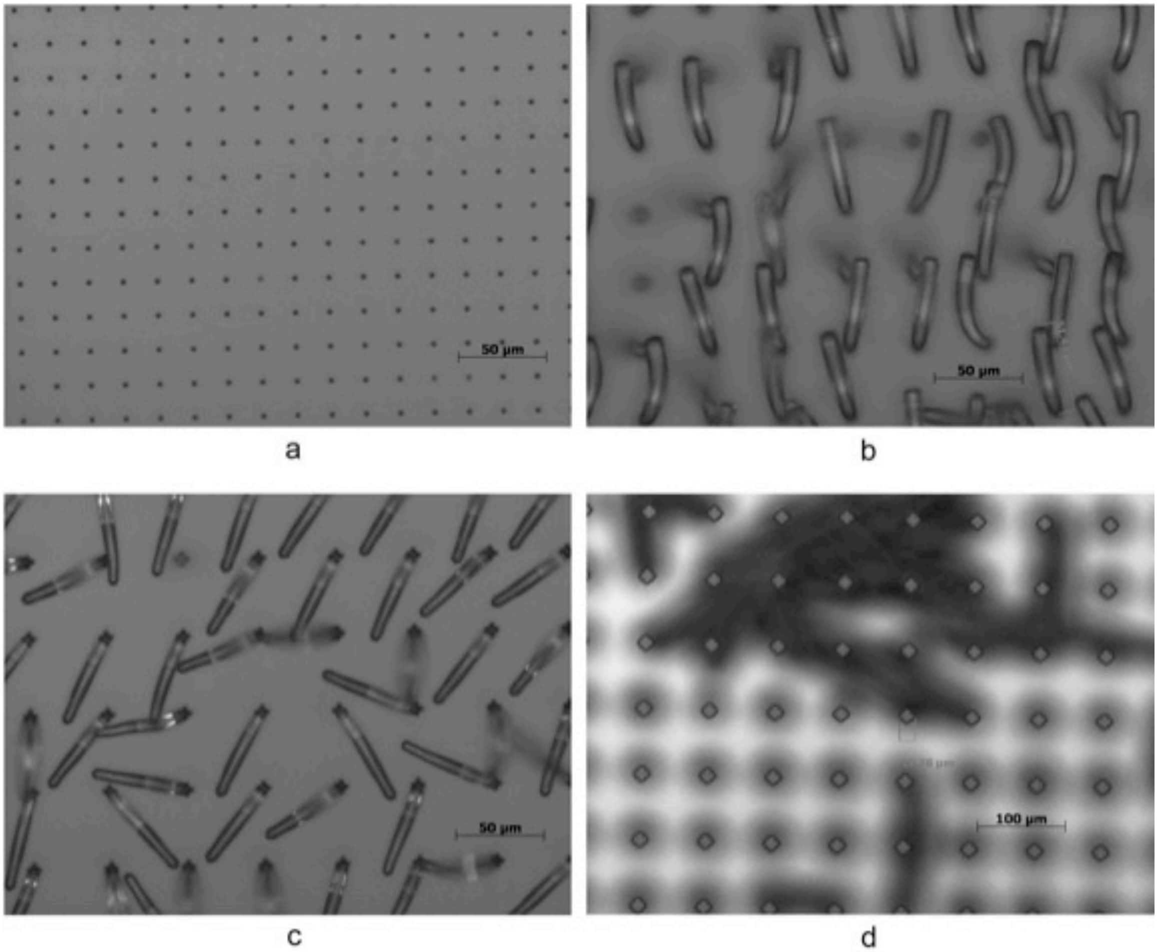

Figure 4.25: Representative images of unloaded PDMS micropost arrays.
Scale bars are 50 µm in length, except (d) that has a 100 µm scale bar.
(a,b) Round microposts, (c) cross-shaped microposts, and (d) diamond-shaped microposts.
Note that (b) and (c) have suffered irreversible collapse do to mold adherence.

Figure 4.25a and Figure 4.25d show representative successfully-produced unloaded PDMS micropost arrays, whereas the arrays depicted in Figure 4.25b and Figure 4.25c show arrays where mold release protocols were unoptimized and separation of the arrays from the negative molds resulted in micropost damage. However, Figure 4.25c emphasizes that the fabrication methods employed permitted the ability to fabricate PDMS microposts with detailed geometries (such as the cross-shape in this instance).

Figure 4.26 includes representative optical microscopy images of the different micropost lengths examined (100, 200, and 300 μm) for both 10 and 20 % TiO_2 loading, before and after performing supercritical CO_2 drying (SC) drying of the micropost arrays.

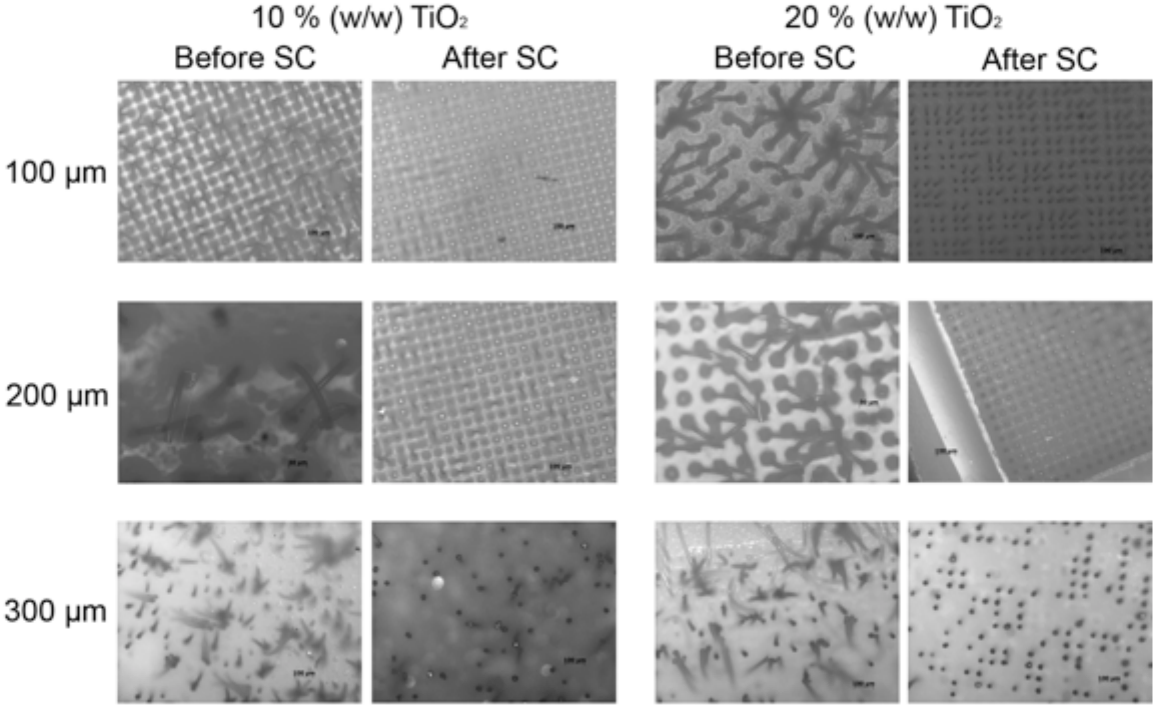

Figure 4.26: Representative microscopy images of the TiO_2-loaded micropost arrays. SC = supercritical drying. 100, 200, and 300 μm labels refer to the micropost design length.

For all samples, the SC drying step yielded vertical-standing microposts, without significant numbers of collapsed microposts or undesired adhesion between micropost tips (as was evident before performing supercritical drying and can be seen in the lefthand columns of Figure 4.26). The arrays visible in the righthand columns of Figure 4.26 appear as many individual dots when viewed from above using optical microscopy, pointing to their vertical (non-collapsed) alignment. Attaining this uniformly erect micropost orientation throughout the different array geometries was crucial for moving forward with contact angle measurements and deflection experiments. The micropost arrays designed for a micropost length of 300 μm were the most challenging to fabricate, as can be seen in the bottom row of Figure 4.26. Based on the successful ability to prepare 100, 200, and 300 μm in length microposts for both 10 and 20 % (w/w) TiO_2 formulations, all three of these microposts lengths were investigated for their surface hydrophobicity (through contact angle measurements) and deflectability (through exposure to an electric field).

4.4.3 Surface Hydrophobicity and Micropost Deflectability

Macroscopically, the super-hydrophobicity of the micropost arrays was visually apparent upon depositing DI water droplets (1, 2, and 4 μL volume droplets) onto the arrays and observing the highly rounded droplet morphology characteristic of super-hydrophobic surfaces. Water beaded up on the templated TiO_2-PDMS microposts immediately, as seen in Figure 4.27.

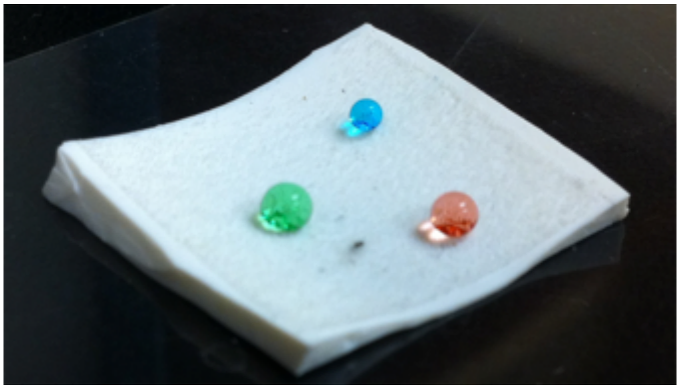

Figure 4.27: Macroscopic evaluation of surface hydrophobicity.
Sample = 100 μm microposts (15 μm diameter, 50 μm spacing), 20 % (w/w) TiO_2 loading.
Blue droplet = 4 μL, red droplet = 8 μL, green droplet = 10 μL.

Under the goniometer, the microposts supporting the droplets could often be readily observed, as shown in Figure 4.28. In particular, Figure 4.28a most clearly depicts the structural integrity of the microposts and their uniform layout in the array beneath the droplet. All droplets in Figure 4.28 are highly rounded in morphology pointing to the highly hydrophobic nature of the arrays.

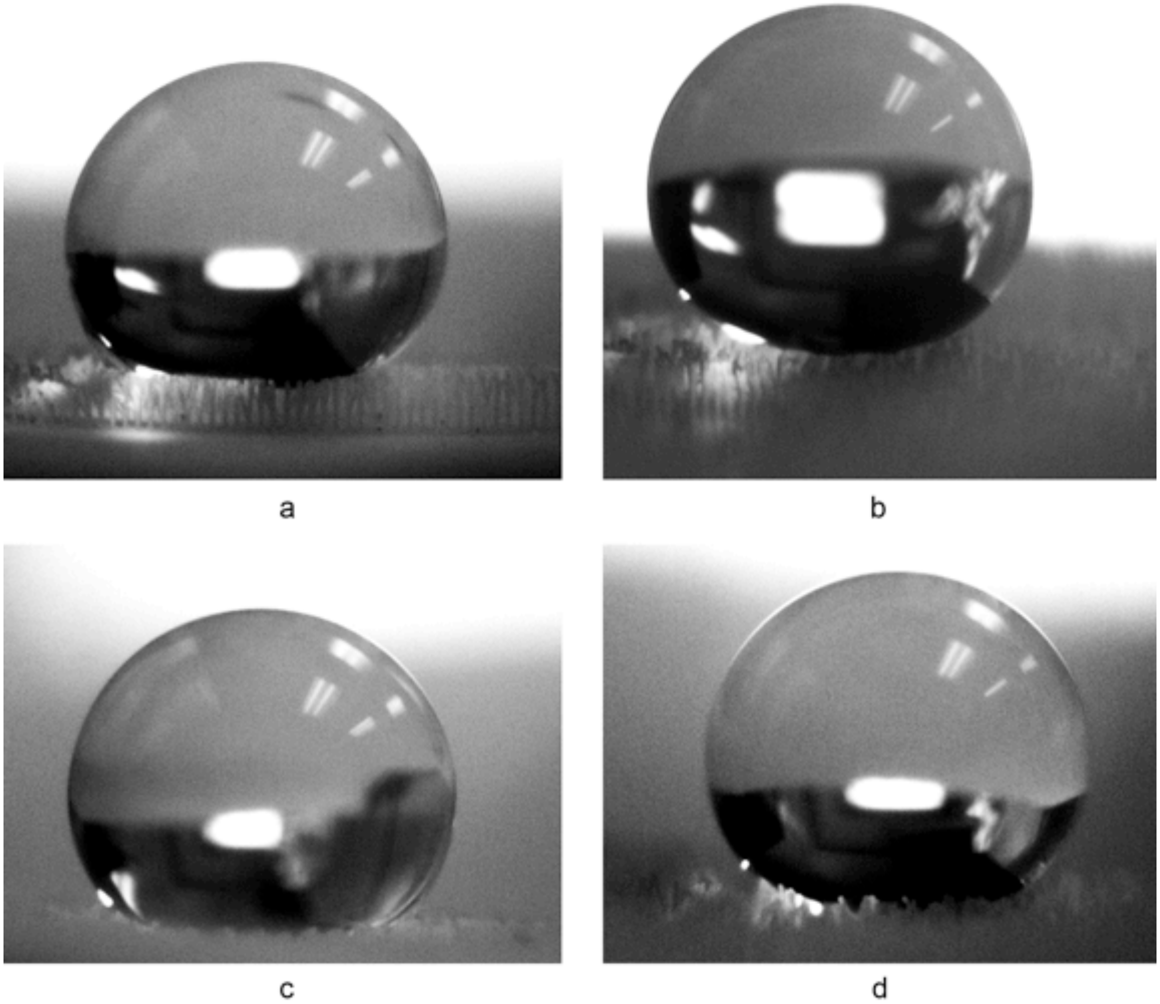

Figure 4.28: Droplets resting on micropost array surfaces.
All droplets are 4 µL in volume.
(a) 10 % (w/w) TiO_2 microposts (200 µm length), (b) 20 % (w/w) TiO_2 microposts (200 µm length),
(c) 10 % (w/w) TiO_2 microposts (300 µm length), and (d) 20 % (w/w) TiO_2 microposts (300 µm length),.

Micropost array surface hydrophobicity was more quantitatively assessed through measuring the contact angles for DI droplets deposited on the various array geometries, with contact angle values being similarly predicted as shown for the bulk film samples in Figure 4.8.

The measured mean contact angle values (θ_R and θ_L) and their corresponding mean CAH values are summarized in Table 4.3 as a function of electric field strength (*n*=3 for each film formulation).

Table 4.3: DI water contact angle data for micropost arrays.
θ_L = lefthand side contact angle, θ_R = righthand side contact angle, CAH = contact angle hysteresis.
Data for each micropost array formulation are listed as the mean ± standard deviation (SD), for electric fields of 0 and 520.8 kV/m (nominal voltage of 0 and 12.5 kV, respectively).
Round microposts with a 15 µm diameter, 50 µm spacing, and varying lengths (100, 200, and 300 µm).

	Electric Field = 0 kV/m			**Electric Field = 520.8 kV/m**		
Array Surface	**θ_L**	**θ_R**	**CAH**	**θ_L**	**θ_R**	**CAH**
PDMS 100 µm	117 ± 9°	134 ± 19°	16 ± 12°	159 ± 5°	147 ± 21°	-11 ± 21°
10% TiO_2 100 µm	148 ± 5°	130 ± 7°	-18 ± 6°	146 ± 13°	137 ± 21°	-10 ± 20°
20% TiO_2 100 µm	142 ± 14°	146 ± 15°	4 ± 4°	151 ± 19°	150 ± 3°	-2 ± 16°
PDMS 200 µm	151 ± 10°	148 ± 10°	-3 ± 10°	141 ± 27°	147 ± 13°	6 ± 15°
10% TiO_2 200 µm	159 ± 10°	142 ± 7°	-18 ± 16°	117 ± 12°	152 ± 8°	34 ± 10°
20% TiO_2 200 µm	160 ± 3°	138 ± 21°	-22 ± 24°	162 ± 6°	144 ± 16°	-18 ± 19°
PDMS 300 µm	152 ± 11°	142 ± 19°	-10 ± 29°	137 ± 15°	144 ± 2°	6 ± 14°
10% TiO_2 300 µm	156 ± 10°	158 ± 8°	3 ± 14°	141 ± 15°	144 ± 27°	3 ± 40°
20% TiO_2 300 µm	157 ± 10°	150 ± 19°	-7 ± 14°	159 ± 3°	144 ± 20°	-15 ± 23°

As compared to the contact angle values measured (and listed in Table 4.2 for the bulk film samples, most contact angle values determined for droplets deposited on the different micropost arrays were above 120° (Table 4.3), pointing to the success of achieving super-hydrophobic surfaces via the micropost array approach. As was the case for bulk film testing, each contact angle measurement was performed in triplicate (*n*=3) to enable the calculation of the mean and standard deviation. Upon comparing the mean measured contact angle values to those predicted by the mathematical model, the measured results aligned with the predicted contact angle values, when taking into account the standard deviations. For example, for a round, 15 µm diameter, 50 µm spaced, and 300 µm in length TiO_2-loaded microposts, the model predicted contact angles of ~170°, while the mean measured values were all above 150°, and in some cases equal to ~170° when considering error. These results point to the usefulness of the model in helping predict array super-hydrophobicity as a function of micropost geometry.

During contact angle measurements performed for droplets deposited on the micropost arrays, the high contact angles obtained for the micropost surfaces pointed to the highly hydrophobic nature of these novel surfaces and validated the model, with mean contact angle values remaining above at least 120° for all samples, many approaching 160°. During contact angle measurements, droplet volume selection was an important parameter for this work. Specifically, droplets too great in volume would effectively exceed a low Bond regime (Bond Numbers << 1), resulting in gravitational effects becoming significant and droplet sagging occurring; thereby introducing undesirable error in contact angle measurements. For this reason, droplets employed in this work were confirmed to have Bond numbers much lower than 1, which resulted in using DI water droplet volumes of 4 μL or lower for all experiments.

Contact angle hysteresis experienced by droplets on the micropost arrays was best visualized through imaging the droplet over time as a function of increasing electric field strength. Figure 4.29 shows a droplet undergoing CAH as the nominal voltage is increased from 0 to 16 kV (corresponding to an increase in electric field strength of 0 to 666.67 kV/m).

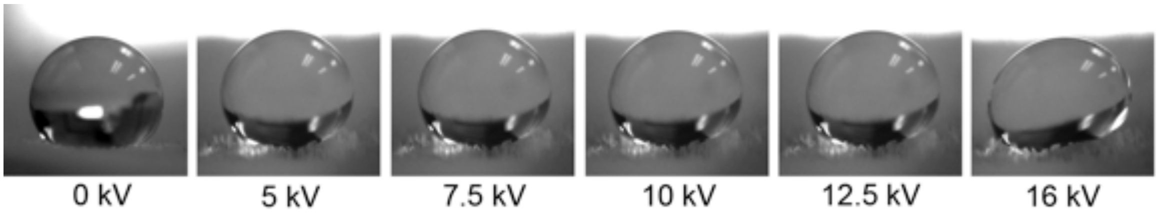
0 kV 5 kV 7.5 kV 10 kV 12.5 kV 16 kV

Figure 4.29: CAH occurring as the nominal voltage is increased.

Considering the mean contact angles observed, some negative CAH values are reported. This is due to charge neutralization during the recorded final measurement. This caused the droplet, under high electric field, to suddenly change direction, resulting in a 'negative' CAH result. These results illuminate the dynamics of the experimental situation.

Toward the aim of assessing ionic droplet behavior in both the absence and presence of an electric field, the contact angles of droplets of DI H_2O+KCl solutions prepared to have a conductivity of 100 mS/m were measured and are listed in Table 4.4.

Table 4.4: Representative 100 mS/m conductive water contact angle data.
θ_L = lefthand side contact angle, θ_R = righthand side contact angle, CAH = contact angle hysteresis.
Data for each selected surface are listed for electric fields of 0 and 520.8 kV/m.
Microposts have a 15 µm diameter and a 50 µm spacing.

		Electric Field = 0 kV/m			**Electric Field = 520.8 kV/m**		
Sample Surface	**Droplet**	θ_L	θ_R	**CAH**	θ_L	θ_R	**CAH**
PDMS Film	4 µL H_2O (DI)	112°	116°	4°	110°	111°	1°
PDMS Film	4 µL H_2O (100 mS/m)	112°	117°	5°	114°	120°	6°
PDMS 300 µm	4 µL H_2O (DI)	141°	164°	23°	132°	144°	12°
PDMS 300 µm	4 µL H_2O (100 mS/m)	146°	129°	-16°	148°	158°	9°
20% TiO_2 300 µm	4 µL H_2O (DI)	152°	156°	4°	155°	166°	11°
20% TiO_2 300 µm	4 µL H_2O (100 mS/m)	158°	149°	-8°	148°	131°	-17°

To investigate micropost movement, conductivity of the droplets was increased markedly (to 100 mS/m), in an attempt to suppress the effects of the electric field on the droplet. This would allow for observation of micropost movement independent of the electric field. The results of the contact angle results obtained for highly conductive water reveal a lack of net micropost movement or a dramatic change in micropost geometry that would lead to any morphological change of the droplet. This could be due to several effects and non-idealities of the experiment, as micropost deflection was observed independently of the contact angle experiments.

Overall, the experiments performed on conductive droplets led to results and questions that require further study beyond the scope of this project to be resolved. Specifically, whether micropost movement is the direct cause of changes in contact angles observed, or if the placement of the entire system within the strong electric field is the ultimate cause of the observed deflections. This could be resolved by fabricating smaller electrodes that could be placed within the structure itself, and is discussed in more detail in the Future Work portion of Chapter 5.

Video observation of individual microposts taken while steadily increasing the electric field strength (from 0 – 187.5 kV/m) permitted visualization of successful micropost deflection. Figure 4.30 demonstrates the deflection of two individual microposts over time, as shown on the individual frames captured from the video.

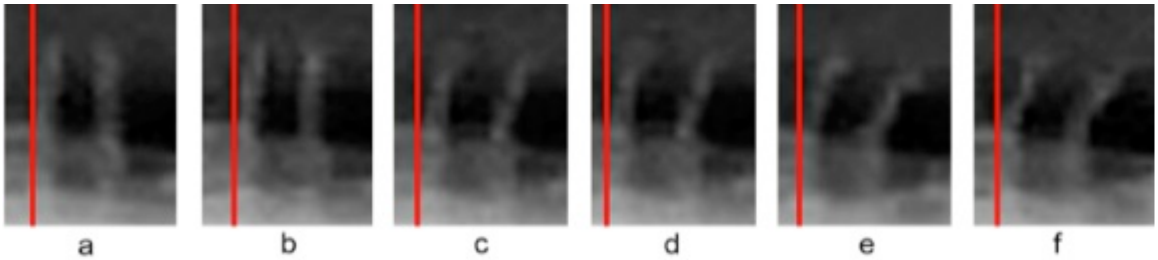

Figure 4.30: Micropost deflection as a function of increasing electric field strength.
Micropost length 300 μm, diameter 15 μm, spacing 50 μm. Two microposts/image.
20 mm electrode spacing, 0 – 3.75 kV nominal voltage, 0 -187.5 kV/m electric field strength.
(a): t=0 and E=0 kV/m (no deflection observed).
(b, c, d, e, f): electric field strength is increased from 0 – 187.5 kV/m (deflection observed).
Red lines provide a vertical reference point.

The microposts in this case were located near the edge of the patterned area. Deflection was clearly observed in the video captured of the experiment, which validated the proof-of-concept presented in this project. The micropost design algorithm was a success, as it produced robust super-hydrophobic arrays with easy to manufacture micropost diameters (between 1 and 10 microns as compared to nanometers), requiring only the minimum of equipment for microfabrication. The surfaces created never resulted in droplet collapse into an irreversible Wenzel state during any of the experiments, even after repeating many of the experiments on the same sample, further demonstrating that the stability graph from the mathematical model generated surfaces that were reliable for microfluid manipulation.

4.4.4 Droplet Motion on Micropost Array Surfaces

Preliminary studies performed to probe the ability to induce droplet movement yielded interesting results. While no droplet motion was observed during video observation for droplets (4 μL volume) deposited on the different micropost arrays produced during this work below nominal voltages of 12.5 kV (electric field strength of 520.8 kV/m), droplet movement was detected in some cases when the nominal voltage was raised to exceed 12.5 kV and steadily increased to 16 kV (666.7 kV/m). This movement was captured on video, and a representative set of images that depict a droplet moving are included in Figure 4.31.

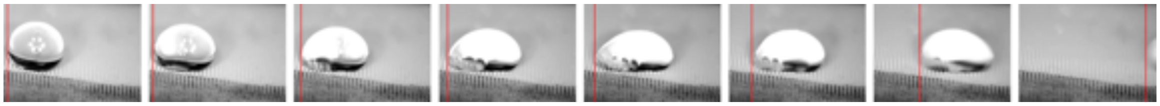

Figure 4.31: Representative droplet movement observed on super-hydrophobic array.
Image frames were available from 10 fps video.
High CAH likely led to droplet motion observed.

Overall, although further work and optimization is necessary, and direct manipulation of droplets via the microposts remains yet to be shown, the electrical actuation of individual microposts observed by video microscopy points to the promise of the results obtained during this work.

4.5 Global Discussion

The results obtained during this work point to the ability for novel, custom-designed micropost arrays fabricated from TiO_2-loaded PDMS to provide super-hydrophobic surfaces that could potentially be used to dynamically control droplet movement by applying an electric field.

Specifically, microposts of varying geometries, diameters, spacings, and heights were investigated and found to successfully deflect as a result of applying a varying electric field. While unloaded PDMS controls did not deflect upon exposure to an electric field, both the 10 % and 20 % (w/w) TiO_2-loaded PDMS microposts demonstrated deflection upon exposure to an electric field ranging from 0 to ~600 kV/m. Although further experimentation and optimization of this work is required to probe the ability to more precisely control micropost deflection, and to perhaps fabricate arrays of selectively-controllable (deflectable) microposts, the findings presented by this work provide a promising foundation for a novel platform by which to manipulate droplets of heterogeneous fluids in the fields of PEM fuel cell design, other microreactor design, and biological/medical diagnostics.

Previous work investigating actuatable micropost arrays, although focused largely on the use of magnetic fields to drive micropost manipulation [6, 73, 77], supports the overall approach of using actuatable micropost arrays to enable the precise control of microdroplets. From a more global perspective, the ability to precisely manipulate droplets would significantly contribute to the fields of microreactor design and bioanalytical technologies [2]. In a closed system, as channel diameter decreases, the resulting pressure drop increases. As a result, the external force required to directly move fluid becomes too high to be maintain small overall device size, due to an increase in manifolding and pumping infrastrucutre. It is desirable that the pumping mechanism and the channel be integrated via usage of digital microfluidics as used in this work. The practicality of such an open microfluidic approach is further supported by the ability to operate such a system in the low Bond number regime, where surface forces dominate and fluid flow is laminar, allowing for the use of EHD to move liquid. While this is promising, such an EHD approach is limited to certain classes of liquids or solutions, with any fluids that approach very high or low conductivity becoming problematic to manipulate using traditional EHD methods.

In the case of hydrogen fuel cells, very clean water approaching a "deionized" state is produced. During fuel cell operation, it is desirable that this water be readily moved out of the fuel manifold. However, because of the very low conductivity of the water produced inside, there exist challenges to using EHD to move the fluid. Specifically, high levels of energy must be expended to effectively move the water droplet due to the lack of free charge. This can lead to hydrolysis of the water, which is once again, highly wasteful from an overall efficiency perspective. Similarly, in the case of readily analyzing biological fluids such as blood, which are typically highly heterogeneous in composition (containing many different ions and proteins), as well as highly conductive (averaging roughly 650 mS/m) [89], the use of traditional EHD methods becomes impractical, with the heating of solutions and electrophoretic phenomena denaturing the sample.

Therefore, significant interest lies in the development of a droplet manipulation platform that could be readily translated to larger-scale use in practical applications such as fuel cells and medical diagnostics (as previously described). The research presented in this thesis focused on developing the basic foundation for a micropost array-based droplet manipulation approach using a readily accessible power source to generate an electric field to actuate the TiO_2/PDMS microposts.

Although the micropost deflection experiments and droplet manipulation investigations performed in this work focused on the use of DI water as a reference point, further experimentation investigating the behavior of other more heterogeneous fluids is recommended so as to elucidate the potential to apply custom-designed micropost array systems to the manipulation of a particular liquids of interest. The inclusion of an integrated electrode array could provide a promising route, leading to the possibility of localized control of post deflection. The electrode array could be fabricated along with the hairs, and the overview of the fabrication is included Chapter 5. Most importantly, it is anticipated that the methods developed and described in this thesis could provide the foundation for a wide range of electrically actuated droplet manipulation platforms, with the flexibility of the design process potentially allowing for surfaces to be tailored toward fluids that are currently not amenable to standard digital microfluidic techniques.

Chapter 5

Conclusions and Future Work

5.1 Conclusions

In this work, methods were developed to design and fabricate novel TiO_2-loaded PDMS-based micropost arrays, which were evaluated as super-hydrophobic surfaces whose microposts could mechanically deflect (and thereby manipulate droplet movement) when exposed to an electric field.

The initial phase of this work focused largely on the development of bulk polymeric films and relevant controls that could deflect in the presence of an electric field, and therefore act as a base material from which to fabricate and investigate polymeric micropost arrays. Upon assessing various PDMS to heat cure ratios, a ratio of 5 or 10 parts PDMS to 1 part heat cure (5:1 or 10:1 w/w) was selected when preparing the PDMS base material. Investigations surrounding different TiO_2 nanoparticles indicated that hydrophobic particles carrying a net charge could be more readily dispersed throughout the PDMS, as compared to hydrophilic uncharged TiO_2 nanoparticles. TiO_2-loaded PDMS films comprised of 10 or 20 % (w/w) TiO_2 nanoparticles were physically characterized, as compared to unloaded PDMS films. Young's Moduli measurements indicated the inverse relationship between the mean value for the Young's Modulus and the weight percentage of TiO_2 nanoparticles added to the PDMS. Contact angle measurements performed for droplets on the bulk films were largely below 120°, as anticipated. Bulk material deflection experiments pointed to a greater deflection obtainable as a function of the weight percentage of TiO_2 nanoparticles, with the 20 % (w/w) TiO_2 formulation demonstrating significantly enhanced deflection in the presence of a 300 kV/m electric field. Overall, the findings from the first phase of this work supported the use of hydrophobic TiO_2-loaded PDMS as a base material for use in developing novel, deflectable micropost arrays. PANI-loaded films were found to be unsuitable for use in fabricating microposts arrays based on their poor structural integrity.

The second phase of this project was dedicated to designing, fabricating, and characterizing micropost arrays made of TiO_2-loaded PDMS. Mathematical modeling was employed to design micropost arrays that were predicted to yield stable, super-hydrophobic surfaces. These geometric micropost array parameters were in turn used to draw photomasks for use in preparing the micropost arrays. The photomasks were manufactured using standard industry protocols, and then applied to selectively crosslink SU8-coated silicon wafers under UV light. These master templates of SU8-based microposts were made in various thicknesses (100, 200, and 300 µm in thickness) to enable the fabrication and investigation of different micropost lengths. PDMS-based negative molds were cast from these SU8-based master templates to yield arrays of “holes.” Finally, these negative molds were used to make the desired TiO_2-loaded PDMS micropost arrays from PDMS loaded with different weight percentages of TiO_2 nanoparticles (10 and 20 % (w/w)). Using like methods, unloaded PDMS-based micropost arrays were prepared and used as controls during micropost array characterization.

Results obtained during micropost array characterization showed that the micropost arrays did indeed yield super-hydrophobic surfaces, as quantified by the contact angle measurements taken for droplets deposited on the arrays that showed the droplet contact angles remained largely above 120°. Furthermore, micropost characterization results pointed to the ability to successfully deflect microposts spaced 50 µm apart, and with a diameter of 15 µm, in the presence of a ~500 kV/m electric field. As such, these results support the use of TiO_2-loaded PDMS micropost arrays as a novel droplet manipulation platform.

This work represents an important step towards a new technology through which a wide range of fluid types could potentially be precisely manipulated indirectly using an electric field to mechanically actuate the microposts. Given the nature of the platform, it is anticipated that this approach could prove helpful in moving non-ionic, highly-ionic, or heterogeneous fluids (such as blood) that existing micropumping technologies currently handle inefficiently. Overall, the ability to precisely control droplets through dynamically modifying surface wettability using the micropost arrays developed in this work could significantly contribute to the fields of reactor design and medical diagnostic technologies, amongst other platforms.

5.2 Contributions

The most significant contributions of this work to the field of digital microfluidics were:

- The design, manufacture, and characterization of novel polymeric composite micropost arrays made from TiO_2-loaded PDMS, yielding super-hydrophobic surfaces that could be customized via mathematical predictions to accommodate specific liquids/substrates.
- The successful demonstration of TiO_2-loaded PDMS microposts as mechanically actuatable, or deflectable, in the presence of an electric field, pointing to the potential to precisely control surface wettability in droplet manipulation applications.

5.3 Future Work

The results from the work presented in this thesis indicate that TiO_2-loaded PDMS micropost arrays hold promise as electrically controllable, dynamic, super-hydrophobic surfaces. This novel technology could be particularly valuable in those instances where the precise manipulation of heterogeneous fluids is desired. Toward the goal of ultimately translating this overall approach to practical uses, additional protocol optimization and micropost characterization beyond the scope of this thesis is required. Therefore, this section includes the recommended short- and long-term future experimental steps that could be performed during further TiO_2-loaded PDMS micropost array development and optimization.

5.3.1 Micropost Array Design and Fabrication

To further expedite the design process of the micropost arrays, it would be desirable to quickly output micropost geometries (including length, diameter, spacing, shape, etc.). Toward this aim, it is recommended that;

- Computer code be developed using Surface Evolver (via three-dimensional (3-D) droplet profile predictions to minimize surface energy), so as to automatically generate micropost geometry sets that would yield stable, super-hydrophobic surfaces deflectable in the presence of an electric field.
- The methodology introduced by Choi *et al.* (2009) parameters [42] could be employed to effectively model contact angle hysteresis as related to the generation of optimized micropost array designs, especially for a given micropost shape.
- Simulations could be run to approximate and describe the dielectric forces present as a result of the "micropost array/droplet/electric field" systems developed in this work. This would be especially useful in developing a relationship between the applied electric field, micropost design spacing, and final deflection of the composite material.

In the current work, SU8 photoresist spun-coat onto silicon wafers was used to prepare the master templates, which were in turn used to make the negative molds and finally the micropost arrays. However, through further optimizing the fabrication techniques used to generate the master templates, exploration of the impact of micropost shape on surface hydrophobicity could be more rigorously probed given that the resulting microposts could be made with greater geometrical precision. Therefore, to further optimize the quality of the resulting master templates, it is recommended that;

- Master templates made using etchants applied selectively to silicon, thereby yielding entirely silicon-based master templates, be investigated as a possible alternative to using SU8-coated silicon, to improve the quality of microfeatures and the structural robustness of the resulting master templates.

While PDMS was employed successfully in the current work as a dispersion medium for the TiO_2-nanoparticles, the potential to use alternative dispersion mediums should be explored, to ensure the best possible polymer is used as the base material. Therefore, it is recommended that;

- Alternative polymers, such as poly(urethane) [90] should be investigated as dispersion mediums for the TiO_2 nanoparticles. The use of the higher Young's Modulus materials could allow for higher ease of manufacture, and potentially higher overall aspect ratios. The resulting micropost array arrays could be similarly characterized using contact angle measurements and deflection experiments with an electric field.

Overall, TiO_2 was shown as an excellent candidate for use in the overall deflectable micropost array approach developed in this work. For the purposes of further optimizing this technology, it is recommended that;

- More potent TiO_2 nanoparticles be obtained and tested for use in loading PDMS, or some other dispersion medium from which the arrays could be fabricated. Through the use of more dielectric particles, the strength of electric field applied could be reduced, increasing the practicality of the overall approach.
- Alternative particles, such as silica, be investigated.

5.3.2 Micropost Array Characterization

In this work, deionized water droplet behavior in the absence and presence of an indirectly applied electric field was assessed for selected micropost array geometries. Therefore, the results from this work provide a foundation and starting point toward further optimizing micropost array geometries. This work also provides the logical starting point to continue probing the behavior of more heterogeneous fluids on the micropost array surfaces in the presence of an electric field. Steps toward testing the manipulation of droplets of fluids such as blood and other proteinaceous solutions could be taken to better characterize the clinical translatability of this technology. Therefore, the following steps are recommended to advance the findings from the current study;

- Using like contact angle and deflection experiments, evaluate the behavior of droplets of i) blood, and ii) highly ionic solutions, on the same micropost array geometries as those investigated in the current study.

- Perform additional contact angle measurements and deflection experiments for droplets on additional micropost array geometries to further assess the specific impact of parameters such as micropost shape on the ease by which droplets can be manipulated on these arrays. Findings from such experiments would in turn further optimize the overall micropost array design process.

- Design and fabricate micro-scale electrodes in the form of micro-scale gold wires to more precisely apply electric fields to select portions of the arrays, thereby better controlling potential droplet movement. Further, through employing micro-electrodes, high electric strengths could be achieved with low nominal voltage. This could be done via the simultaneous production of channels within the pattern at a given spacing frequency. These channels could then by coated with gold via capillary wetting as described in Xu *et* *al.* (2011) [91]. Ultimately, this could pave the way to a surface in which individual sections could be actuated.

- Droplet direction could be controlled via actuation of microposts by gold electrodes and motion achieved through vibration as seen in work by Daniel *et al.* (2005) [92]. This could provide a robust microfluidic platform that would be free from current digital microfluidic limitations.

References

[1] Li H, Tang Y, Wang Z, Shi Z, Wu S, Song D*, et al.* A review of water flooding issues in the proton exchange membrane fuel cell. Journal of Power Sources 2008;178:103-17.

[2] Rodríguez-Villarreal AI, Arundell M, Carmona M, Samitier J. High flow rate microfluidic device for blood plasma separation using a range of temperatures. Lab Chip 2010 Jan 1;10(2):211.

[3] Chakrabarty K, Su F. Microfluidics and Microfabrication: Springer Science+Business Media, LLC, 2006.

[4] Daniel S, Chaudhury M. Rectified motion of liquid drops on gradient surfaces induced by vibration. Langmuir 2002 Jan 1;18(9):3404-7.

[5] Chen T-H, Chuang Y-J, Chieng C-C, Tseng F-G. A wettability switchable surface by microscale surface morphology change. Journal of micromechanics and microengineering 2007;17(3):489-95.

[6] Fahrni F, Prins MWJ, Van Ijzendoorn LJ. Micro-fluidic actuation using magnetic artificial cilia. Lab Chip 2009 Jan 1;9(23):3413.

[7] Sniadecki NJ, Anguelouch A, Yang MT, Lamb CM, Liu Z, Kirschner SB*, et al.* Magnetic microposts as an approach to apply forces to living cells. Proceedings Of The National Academy Of Sciences Of The United States Of America 2007 Sep 05;104(37):14553-8.

[8] Zaharias G, Shi H, Bent S. Characterization of polyconjugated thin films synthesized by hot-wire chemical vapor deposition of aniline. Thin Solid Films 2006 Jan 1;501(1-2):341-5.

[9] Zrınyi M, Feher J, Filipcsei G. Novel Gel Actuator Containing TiO2 Particles Operated under Static Electric Field. Macromolecules 2000;33(16):5751-3.

[10] Gallone G, Galantini F, Carpi F. Perspectives for new dielectric elastomers with improved electromechanical actuation performance: composites versus blends. Polym Int 2010;59:400-6.

[11] Tabeling P. Introduction to Microfluidics, 2005.

[12] Bhushan B. Springer handbook of nanotechnology, 2004.

[13] Van Lintel H, Van de Pol F, Bouwstra S. A piezoelectric micropump based on micromachining of silicon. Sensors and Actuators 1988 Jan 1;15:153-67.

[14] Iverson B, Garimella S. Recent advances in microscale pumping technologies: a review and evaluation. Microfluidics and Nanofluidics 2008 Jan 1.

[15] Woias P. Micropumps—past, progress and future prospects. Sensors & Actuators: B Chemical 2005 Jan 1.

[16] Whitesides G, Xia Y. Soft Lithography. Angewandte Chemie International Edition 1998 Mar 6;37(5):550-75.

[17] Nguyen N, Huang X, Chuan T. MEMS-Micropumps: A Review. Journal of Fluids Engineering 2002;124(2):384-92.

[18] Holmberg K. Handbook of applied surface and colloid chemistry, Volume 2. 2002 Jan 1:1110.

[19] Wenzel R. Resistance of solid surfaces to wetting by water. Ind Eng Chem 1936 Jan 1;28:988-94.

[20] Cassie A, Baxter S. Wettability of porous surfaces. T Faraday Soc 1944 Jan 1;40:0546-50.

[21] Bhushan B, Nosonovsky M, Jung Y. Lotus effect: roughness-induced superhydrophobic surfaces. Nanotribology and Nanomechanics 2008:995-1072.

[22] Lafuma A, Quere D. Superhydrophobic states. Nat Mater 2003 Jan 1;2(7):457-60.

[23] Oner D, McCarthy T. Ultrahydrophobic surfaces. Effects of topography length scales on wettability. Langmuir 2000 Jan 1;16(20):7777-82.

[24] Yeo J, Choi MJ, Kim DS. Robust hydrophobic surfaces with various micropillar arrays. J Micromech Microeng 2010 Jan 1;20(2):025028.

[25] Callies M, Quere D. On water repellency. Soft Matter 2005 Jan 1;1(1):55-61.

[26] Quere D. Wetting and roughness. Annu Rev Mater Res 2008 Jan 1;38:71-99.

[27] Sun T, Feng L, Gao X, Jiang L. Bioinspired surfaces with special wettability. Accounts Chem Res 2005 Jan 1;38(8):644-52.

[28] Feng L, Zhang Y, Xi J, Zhu Y, Wang N, Xia F*, et al.* Petal effect: A superhydrophobic state with high adhesive force. Langmuir 2008 Jan 1;24(8):4114-9.

[29] Bhushan B, Her EK. Fabrication of Superhydrophobic Surfaces with High and Low Adhesion Inspired from Rose Petal. 2010 Feb 3:1-11.

[30] Bartolo D, Bouamrirene F, Verneuil E, Buguin A, Silberzan P, Moulinet S. Bouncing or sticky droplets: Impalement transitions on superhydrophobic micropatterned surfaces. Europhys Lett 2006 Jan 1;74(2):299-305.

[31] Dupuis A, Yeomans J. Dynamics of sliding drops on superhydrophobic surfaces. Europhys Lett 2006 Jan 1;75(1):105-11.

[32] Ishino C, Okumura K. Nucleation scenarios for wetting transition on textured surfaces: The effect of contact angle hysteresis. Europhys Lett 2006 Jan 1;76(3):464-70.

[33] Ishino C, Reyssat M, Reyssat E, Okumura K, Quere D. Wicking within forests of micropillars. Epl-Europhys Lett 2007 Jan 1;79(5):56005.

[34] Reyssat M, Pepin A, Marty F, Chen Y, Quere D. Bouncing transitions on microtextured materials. Europhys Lett 2006 Jan 1;74(2):306-12.

[35] Bormashenko E. Why does the Cassie-Baxter equation apply? Colloid Surface A 2008 Jan 1;324(1-3):47-50.

[36] Gao N, Yan Y. Modeling Superhydrophobic Contact Angles and Wetting Transition. Journal of Bionic Engineering 2009 Dec 24;6(4):335-40.

[37] Marmur A. Wetting on hydrophobic rough surfaces: To be heterogeneous or not to be? Langmuir 2003 Jan 1;19(20):8343-8.

[38] Patankar N. Transition between superhydrophobic states on rough surfaces. Langmuir 2004 Jan 1;20(17):7097-102.

[39] Peters AM, Pirat C, Sbragaglia M, Borkent BM, Wessling M, Lohse D*, et al.* Cassie-Baxter to Wenzel state wetting transition: Scaling of the front velocity. Eur Phys J E 2009 Aug 9;29(4):391-7.

[40] Bico J, Thiele U, Quere D. Wetting of textured surfaces. Colloid Surface A 2002 Jan 1;206(1-3):41-6.

[41] Extrand C. Model for contact angles and hysteresis on rough and ultraphobic surfaces. Langmuir 2002 Jan 1;18(21):7991-9.

[42] Choi W, Tuteja A, Mabry JM, Cohen RE, Mckinley GH. A modified Cassie–Baxter relationship to explain contact angle hysteresis and anisotropy on non-wetting textured surfaces. J Colloid Interf Sci 2009 Jan 11;339(1):208-16.

[43] Berthier J. Microdrops and digital microfluidics, 2008.

[44] Bahadur V, Garimella S. Electrical actuation-induced droplet transport on smooth and superhydrophobic surfaces. International Journal of Micro-Nano Scale Transport 2010;1(1):1-26.

[45] Hsu S-H, Sigmund WM. Artificial Hairy Surfaces with a Nearly Perfect Hydrophobic Response. Langmuir 2010 Jan 7:100107015319064.

[46] Chandra D, Yang S. Stability of High-Aspect-Ratio Micropillar Arrays against Adhesive and Capillary Forces. Accounts Of Chemical Research 2010;43(8):1080-91.

[47] Roca-Cusachs P, Rico F, Martínez E, Toset J, Farré R, Navajas D. Stability of Microfabricated High Aspect Ratio Structures in Poly(dimethylsiloxane). Langmuir 2005 Jun 1;21(12):5542-8.

[48] Bernardino NR, Blickle V, Dietrich S. Wetting of Surfaces Covered by Elastic Hairs. Langmuir 2010 Jan 29:100129095351070.

[49] Morgan H, Green NG. AC Electrokinetics: Colloids and Nanoparticles: Research Studios Pr, 2003.

[50] Jones T, Wang K, Yao D. Frequency-dependent electromechanics of aqueous liquids: Electrowetting and dielectrophoresis. Langmuir 2004 Jan 1;20(7):2813-8.

[51] Yeo L, Chang H. Electrowetting films on parallel line electrodes. Phys Rev E 2006;73(011605):01-16.

[52] Bao N, Zhang Q, Xu J, Chen H. Fabrication of poly (dimethylsiloxane) microfluidic system based on masters directly printed with an office laser printer. Journal of Chromatography A 2005;1089(1-2):270-5.

[53] Bhushan B. Micro/Nanodroplets in Microfluidic Devices, 2007.

[54] Niu X, Peng S, Liu L, Wen W, Sheng P. Characterizing and Patterning of PDMS-Based Conducting Composites. Advanced Materials 2007;19:2682-6.

[55] Jin M, Feng X, Xi J, Zhai J, Cho K, Feng L*, et al.* Super-Hydrophobic PDMS Surface with Ultra-Low Adhesive Force Macromolecular Rapid Communications 2005;26(22).

[56] Rogers J, Nuzzo R. Recent progress in soft lithography. Materials today 2005;8(2):50-6.

[57] Yun K, Yoon E. Micropumps for MEMS/NEMS and Microfluidic Systems. MEMS/NEMS: handbook techniques and applications 2006 Jan 1.

[58] Laser D, Santiago J. A review of micropumps. Journal of micromechanics and microengineering 2004;14:35-64.

[59] Abdelgawad M, Freire S, Yang H, Wheeler A. All-terrain droplet actuation. Lab Chip 2008;8(5):672-7.

[60] Becker H, Locascio L. Polymer microfluidic devices. Talanta 2002;56(2):267-87.

[61] Soper S, Henry A, Vaidya B, Galloway M, Wabuyele M, McCarley R. Surface modification of polymer-based microfluidic devices. Anal Chim Acta 2002 Jan 1;470(1):87-99.

[62] Lee J, Park C, Whitesides G. Solvent compatibility of poly(dimethylsiloxane)-based microfluidic devices. Anal Chem 2003 Jan 1;75(23):6544-54.

[63] McDonald J, Whitesides G. Poly (dimethylsiloxane) as a material for fabricating microfluidic devices. Acc Chem Res 2002;35(7):491-9.

[64] Ci L, Suhr J, Pushparaj V, Zhang X, Ajayan PM. Continuous carbon nanotube reinforced composites. Nano Lett 2008 Jan 1;8(9):2762-6.

[65] Gardiner MB. The Importance of Being Cilia. HHMI Bulletin 2005 Sep 1(September):1-6.

[66] Toonder JMd. Micro-fluidic manipulation using artificial cilia. 2007 Oct 31:1-.

[67] Satir P, Christensen ST. Structure and function of mammalian cilia. Histochem Cell Biol 2008 Jun 26;129(6):687-93.

[68] Tamm S. Visualization of changes in ciliary tip configuration caused by sliding displacement of microtubules in macrocilia of the ctenophore Beroe. Journal of Cell Science 1985;79(1):161-79.

[69] Barlow D, Sleigh M. Water propulsion speeds and power output by comb plates of the Ctenophore Pleurobrachia pileus under different conditions. Journal of Experimental Biology 1993;183(1):149-64.

[70] Barlow D, Sleigh M, White R. Water flows around the comb plates of the ctenophore Pleurobrachia plotted by computer: a model system for studying propulsion by antiplectic metachronism. Journal of Experimental Biology 1993;177(1):113-28.

[71] Castellanos A, Ramos A, Gonzalez A, Green N, Morgan H. Electrohydrodynamics and dielectrophoresis in microsystems: scaling laws. J Phys D Appl Phys 2003 Jan 1;36(20):2584-97.

[72] Zhou Z-g, Liu Z-w. Biomimetic Cilia Based on MEMS Technology. Journal of Bionic Engineering 2008 Dec 27;5(4):358-65.

[73] Evans BA, Shields AR, Carroll RL, Washburn S, Falvo MR, Superfine R. Magnetically actuated nanorod arrays as biomimetic cilia. Nano Lett 2007 Jan 1;7(5):1428-34.

[74] Krijnen G, Dijkstra M, van Baar J, Shankar S, Kuipers W, de Boer R*, et al.* MEMS based hair flow-sensors as model systems for acoustic perception studies. Nanotechnology 2006 Jan 1;17(4):S84-S9.

[75] Tan J, Tien J, Pirone D, Gray D, Bhadriraju K, Chen C. Cells lying on a bed of microneedles: an approach to isolate mechanical force. P Natl Acad Sci Usa 2003;100(4):1484.

[76] Khatavkar VV, Anderson PD, Den Toonder JMJ, Meijer HEH. Active micromixer based on artificial cilia. Phys Fluids 2007 Jan 1;19(8):083605.

[77] Gauger EM, Downton MT, Stark H. Fluid transport at low Reynolds number with magnetically actuated artificial cilia. Eur Phys J E 2009 Feb 20;28(2):231-42.

[78] Khaderi SN, Baltussen MGHM, Anderson PD, Ioan D, Den Toonder JMJ, Onck PR. Nature-inspired microfluidic propulsion using magnetic actuation. Phys Rev E 2009 Apr 1;79(4):046304.

[79] van Oosten CL, Bastiaansen C, Broer D. Printed artificial cilia from liquid-crystal network actuators modularly driven by light. Nat Mater 2009 Jan 1.

[80] Hiamtup P, Sirivat A, Jamieson A. Electromechanical response of a soft and flexible actuator based on polyaniline particles embedded in a cross-linked poly (dimethyl siloxane) network. Materials Science & Engineering C 2008;28(7):1044-51.

[81] Ram M, Salerno M, Adami M, Faraci P, Nicolini C. Physical properties of polyaniline films: Assembled by the layer-by-layer technique. Langmuir 1999 Jan 1;15(4):1252-9.

[82] Sayre C, Collard D. Deposition of polyaniline on micro-contact printed self-assembled monolayers of omega-functionalized alkanethiols. J Mater Chem 1997 Jan 1;7(6):909-12.

[83] Park S, Cho M, Choi H. Synthesis and electrical characteristics of polyaniline nanoparticles and their polymeric composite. Current Applied Physics 2004;4(6):581-3.

[84] Carpi F, Rossi DD. Improvement of Electromechanical Actuating Performances of a Silicone Dielectric Elastomer by Dispersion of Titanium Dioxide Powder. IEEE Transactions on Dielectrics and Electrical Insulation 2005;12(4):835-43.

[85] Watson GS, Cribb BW, Watson JA. How Micro/Nanoarchitecture Facilitates Anti-Wetting: An Elegant Hierarchical Design on the Termite Wing. Acs Nano 2010 Jan 1;4(1):129-36.

[86] Mata A, Fleischman A, Roy S. Fabrication of multi-layer SU-8 microstructures. Journal of micromechanics and microengineering 2006;16:276.

[87] Senousy YM, Harnett CK. Fast three dimensional ac electro-osmotic pumps with nonphotolithographic electrode patterning. Biomicrofluidics 2010;4(3):-.

[88] O'Halloran A, O'Malley F, McHugh P. A review on dielectric elastomer actuators, technology, applications, and challenges. Journal Of Applied Physics 2008;104(7):071101.

[89] Mohapatra SN, Costeloe KL, Hill DW. Blood resistivity and its implications for the calculation of cardiac output by the thoracic electrical impedance technique. Intensive Care Med 1977;3:63-7.

[90] Zhang Y, Lo C-W, Taylor JA, Yang S. Replica molding of high-aspect-ratio polymeric nanopillar arrays with high fidelity. Langmuir 2006;22(20):8595-601.

[91] Xu Q, Bi L, Zheng H, Fan D, Wang W. PDMS-based gold electrode for sensing ascorbic acid. Colloids and surfaces B, Biointerfaces 2011 Jul 12.

[92] Daniel S, Chaudhury M, de Gennes P. Vibration-actuated drop motion on surfaces for batch microfluidic processes. Langmuir 2005;21(9):4240-8.